博士論文

Functionalization of metal-oxide and sulfide minerals toward efficient multi-electron transfer catalysis with abundant elements
（普遍元素からなる多電子移動触媒に向けた金属酸化・硫化鉱物の機能化）

山口　晃

Table of Contents

Chapter 1.

General Introduction

1.1. Background and objective of this study

Multi-electron transfer catalysts are one of the key components to construct energy conversion systems because multi-electron transfer reactions proceed thermodynamically favorably compared with sequential electron transfer reactions. Although development of efficient multi-electron transfer catalysts is unquestionably important, it is also highly challenging research subject since it requires the management of the multiple numbers of electrons. In general, noble metal-based catalysts exhibit high catalytic activity toward large numbers of multi-electron transfer reactions. The scarcity of the noble metal elements, however, promoted researchers to develop ubiquitous element-based catalysts like 3d metal elements, which are earth-abundant elements. Although noble metal-based catalysts possess high catalytic activity under mild condition such as neutral pH, room temperature and moderate pressure, 3d metal element-based catalysts usually requires more extreme condition, that is, high acidic or alkaline pH, high temperature, and high pressure to show their catalytic activity. Thus, promising design strategy for multi-electron transfer catalysts is highly demanding to achieve ubiquitous elements-based catalysts which can operate under mild conditions.

One approach for utilization of 3d metal elements as multi-electron transfer catalysts is bio-inspired approach, in which researchers focus on natural enzymes. Enzymes are one of the most efficient multi-electron transfer catalysts in nature, which can promote various reactions in moderate conditions, and their reaction centers never rely on noble metals. Inspired by efficient enzymatic reactions, design of metal organic complexes to mimic the structural motif of the

enzymatic reaction centers have been attempted. However, to realize the functional mimetics of the natural enzymes, not only the structure of the enzymatic catalytic center, but the essential physicochemical parameters should be taken into consideration and the application of them to artificial materials is highly demanding.

Based on the backgrounds, the author has attempted to functionalize metal-oxide and metal-sulfide minerals as multi-electron transfer catalysts, which are composed of earth abundant metal elements and are hypothesized to be the origin of the active centers of enzymes. Especially, the author focused on manganese oxide and iron sulfide because they play crucial roles in the two main energy conversion process in nature; that is, photosynthesis converting solar energy to chemical energy and chemoautotrophic process under deep sea environment. In natural photosynthesis, manganese oxide cluster (Mn_4-cluster) catalyzes O_2 evolution reaction from water to extract electrons for carbon fixation. Manganese is the only elements catalyzing O_2 evolution and it is suggested that the origin of naturally occurring Mn_4-cluter is manganese oxide minerals [1-4]. On the other hand, iron sulfides are considered to have contributed to the prebiotic organic synthesis by catalyzing CO_2 reduction at deep sea hydrothermal vents [5]. These facts and hypothesizes have led the author to further consider that these manganese oxide and iron sulfide minerals are potentially active catalysts towards O_2 evolution and CO_2 reduction reaction, respectively.

Not only the active center, but the reaction field in which the active center was embedded was also play crucial roles to maintain the catalytic activity especially in terms of electron and proton transfer regulation and organization of the functional motifs to the adequate positions. Indeed, natural enzymatic system possess sophisticated protein networks to promote catalytic cycle efficiently and stably. Therefore, development of the reaction fields satisfying the parameters mentioned above is also essential to construct sustainable reaction systems.

In this work, based on the concept that the newly functionalization of minerals can be achieved in terms of the management of electron and proton transfer, author attempted to extract the function as multi-electron transfer catalysts from iron sulfide and manganese oxide minerals and to develop a reaction fields where the mineral catalysts work as active centers.

First, the catalytic activity of minerals were examined and found out that the catalytic activity drastically decrease compared with the present enzymatic reactions even though the minerals were hypothesized to be the origin of active centers. Second, from the observations for the catalytic properties of bare mineral samples, the author attempted to understanding the functional difference between the minerals and enzymes and noticed the importance of the taking into consideration of surrounding environment of minerals. As to the CO_2 reduction reaction with iron sulfides, author focused on the co-existence ions and coordinating N-containing polymers similarity to the enzymatic catalytic centers. By combining the knowledge and electrochemical properties of iron sulfide itself, the author proposed to the strategy to improve the catalytic activity. As to the O_2 evolution catalysts, he introduced the lacking function of minerals as O_2 evolution catalysts to the minerals and succeeded to enhance the catalytic activity.

Third, the reaction filed inspired by the surrounding amino acid residues around active centers in natural enzyme was developed. To develop the reaction field, author focused on the electron and proton transfer, and photo-functionalization properties of polyoxomatalate and succeeded to develop the desired systems by blending polyoxometalate and polymer materials. The photochemical results indicate the usability of the constructed membrane system as catalytic reaction fields.

1.2. Overview of this thesis

In chapter 2, the author proposed the design strategy to improve the CO_2 reduction activity of the iron sulfides. In this study, he synthesized one of iron sulfides (greigite) which is hypothesized to have worked as the catalytic centers of CO_2 reduction to organic molecules in the primordial deep sea oceans [5]. However, through the electrochemical investigations of the CO_2 reduction catalysts, he found out that the greigite was catalytically inactive toward CO_2 reduction. To functionalize the iron sulfide, he focused on the co-existing hetero metal ions in deep sea oceans, like Ni^{2+}, Cu^{2+}, and Zn^{2+}. Hetero metal atom-doped iron sulfide was synthesized by the introduction of these metal ions during the synthesis procedure and the electrochemical properties of the samples were investigated. As a result, the faradaic efficiency (FE) for CH_4 formation was enhanced with the sample for Ni-containing iron sulfide (violarite), while Cu and Zn doped samples exhibited smaller improvement. In addition, by modifying the surface of violarite with nitrogen-containing polymer, the FE was further increased. The nitrogen atom can donate the unshared electrons to the LUMO of CO_2 (π^*), resulting the decrease of overpotential to facilitate the cleavage of C=O bond. The obtained results indicated that surrounding environment should be taken into consideration for catalyst design, not only the structure of the minerals.

In chapter 3, the author developed Mn-based O_2 evolution catalysts which can operate under neutral condition by the induction of Concerted Proton-coupled Electron Transfer (CPET). *In situ* spectroelectroscopic measurement show that the protonation state of intermediate Mn^{3+} [6] is different between low active-neutral and high active-alkaline conditions. Furthermore, the author noticed that the proton transfer is not involved in the rate-determining step of O_2 evolution reaction on MnO_2 electrode under neutral condition [6], while the proton transfer is coupled in electron transfer step during the catalytic cycle of natural O_2 evolution center. Based on this consideration, he added to the base reagent such as pyridine and its derivatives, which satisfies

the libido rule of acid-base reaction [7]: namely, bases whose pK_a is between the pK_a of $Mn^{2+}(OH_2)$ and that of $Mn^{3+}(OH_2)$ to induce proton transfer during rate-determining electron transfer step. This base addition largely enhanced the electrochemical O_2 evolution activity on MnO_2 electrode under neutral condition (pH = 7.5). Especially, the addition of base whose pK_a is 7.48 (γ-collidine) achieved the activity that is the half of the activity under alkaline condition. Appearance of pH dependence of onset potential and the increase of kinetic isotopic effect by altering H_2O to D_2O in the addition of base reagents indicated that the proton transfer became involved into the rate-determining step. The contribution of buffering effects of base reagents can be ruled out by the activity enhancement under forced convection condition. These results show that the understanding of the functions of natural enzymes and applying them to minerals are one of the promising approaches toward multi-electron transfer catalysts.

In chapter 4, the author constructed a proton and electron conductive membrane based on polyoxometalates and polymer hybrid materials. Polyoxomatalates are one class of metal-oxygen cluster molecules and exhibits characteristic properties including proton and electron conduction. Not only the POM themselves, but their hybrid materials with organic molecules or polymer are potential reaction field in which embedded catalysts operate efficiently. Recently, our group reported a fabrication of photo-induced charge transferring metal complex by reacting POM with Ce^{3+} [8]. The metal complex is suitable model system to confirm the unidirectional electron transfer and the organization of functional component because the system operates only when the relevant redox components is highly ordered. The author applied the knowledge to the proton and electron conductive membrane in this work. By the treatment with Ce^{3+}, a membrane sample fabricated with $H_3PW_{12}O_{40}$, poly vinylalcohol and poly acrylamide exhibited new absorption band in visible region. The absorption was assigned to a metal-to-metal charge transfer from Ce^{3+} to W^{6+}, indicating the success of the photo-induced charge transfer metal complex on the membrane

sample. Furthermore, the photo-functionalization was also achieved by Co^{2+}, whose redox potential was more positive than Ce^{3+}; namely, more strong driving force for oxidation reaction was expected by Co^{2+} substitution to Ce^{3+}. In photoelectrochemical reaction with MnO_2-depositted membrane sample, only a trimetric material (W, Co, Mn) generated photo current. This result indicated that the adequate configuration of light-absorbing site, electron transfer site, and catalysts site was essential for the catalysts system to operate properly, and the membrane system investigated in this work achieved the configuration and the regulation of electron transfer direction.

1.3 Multi-electron transfer

In multi-electron transfer reaction, multiple numbers of electrons are transferred to/removed from a reaction substrate simultaneously. This multi-electron transfer reaction proceeds thermodynamically more favorably than sequential electron transfer in which only one electron is transferred/removed in one elemental step. For instance, in thermodynamic equations of CO_2 reduction (Eq. (1) – (6)) and water oxidation (Eq. (7) – (9)), which are the focus of this work, the standard redox potential become more positive for CO_2 reduction and more negative for O_2 evolution as the number of electrons involved in the reaction increases. Thus, the required energy to promote these reactions is less for the multi-electron transfer reactions compared with sequential one electron transfer reactions. Not only for CO_2 reduction and water oxidation, but for other electron transfer reactions including O_2 reduction, organic compound oxidation, and nitrogen treatment, the same tendency is applied. Thus, the management of multi-electron transfer is one of the promising but challenging issues to construct efficient energy conversion systems.

$$CO_2 + e^- \rightarrow CO_2^- \qquad E^0 = -1.9\ \text{V (vs SHE, pH = 7)} \qquad (1)$$

$$CO_2 + 2H^+ + 2e^- \rightarrow HCOOH + H_2O \qquad E^0 = -0.61\ \text{V} \qquad (2)$$

$$CO_2 + 2H^+ + 2e^- \rightarrow CO + H_2O \qquad E^0 = -0.53\ \text{V} \qquad (3)$$

$$CO_2 + 4H^+ + 4e^- \rightarrow HCHO + H_2O \qquad E^0 = -0.48\ \text{V} \qquad (4)$$

$$CO_2 + 6H^+ + 6e^- \rightarrow CH_3OH + H_2O \qquad E^0 = -0.38\ \text{V} \qquad (5)$$

$$CO_2 + 8H^+ + 8e^- \rightarrow CH_4 + 2H_2O \qquad E^0 = -0.24\ \text{V} \qquad (6)$$

$$H_2O \rightarrow OH + H^+ + e^- \qquad E^0 = 2.38\ \text{V (pH = 0)} \qquad (7)$$

$$2H_2O \rightarrow H_2O_2 + 2H^+ + 2e^- \qquad E^0 = 1.76\ \text{V} \qquad (8)$$

$$2H_2O \rightarrow O_2 + 4H^+ + 4e^- \qquad E^0 = 1.23\ \text{V} \qquad (9)$$

One of familiar examples of multi-electron transfer catalysts is natural enzymes. Multi-electron transfer reactions in biological systems possess advantages in that not only the reaction proceed favorably, but they avoid a formation of radical species which is harmful to the protein systems.

Tributsch pointed out three features of natural enzymes to achieve multi-electron transfer catalysts based on abundant metals [9]. The first one is an efficient protection of metal centers against chemical oxidation by strongly bonded ligands such as CO, CN ligands like hydrogenase in fig. 1a or tetra-pyrrole-rings like hemoglobin, myoglobin, chlorophylls, cytochromes and Vitamin B12 in fig. 1b because 3d metal elements are easily oxidized. These ligands obviously can stabilize the reaction center to inhibit irreversible oxidation of the metal center without interference of binding reaction substrates.

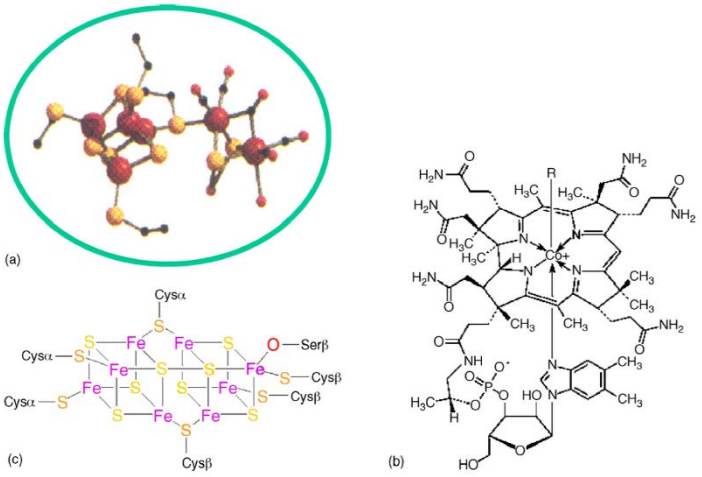

Fig.1 Representative examples of the biological strategies to achieve multi-electron transfer catalysts based on abundant metals pointed by Tributsch (Reprinted with permission from ref. 9. Copyright 2006, Elsevier Ltd.). (a) Active center of iron-only hydrogenase from the bacterium chlostridium pasteurianum [10]. (b) Co center of Vitamin B12. (c) Fe-S center of ferredoxin.

The second property is the storage of the multiple numbers of electrons in the active canter and the availability of them for the chemical reactions. Enzymatic catalytic active centers often adopt cluster-like structure like ferredoxin shown in fig.1c, the cluster serving as the multi-electron reservoir. The final and possibly most important feature of the biological systems pointed by Tributsch is the non-linear electron transfer behavior, that is, positive feedback mechanism. In this mechanism, the transfer of the first electron accelerates the movement of the second and subsequent electrons, making the overall process multi-electron transfer process. Tributsch expected that cysteine ligands play a role in the non-linear mechanism supported by genetic analysis that cysteine in electron transfer components have never been exchanged during evolution while most of other amino acids have been replaced [11]. When an electron is removed from a reaction center, the bonding with cysteine ligand largely changes, resulting in the decrease of the electron density on the amino acid. This facilitates the electron transfer from the neighboring electron donor. As mentioned above, functional mimetics of natural enzymatic centers is one of the promising approaches to develop multi-electron transfer catalysts based on abundant 3d metal elements.

1.4 CO_2 reduction catalysts

1.4.1 Electrochemical CO_2 reduction catalysts

Reduction or fixation of CO_2 is one of the important and at the same time, challenging research topic to construct sustainable society. Many kinds of techniques are adopted to achieve this goal like CO_2 capture into absorbents [12], fixation to other organic compounds [13], electrochemical [14] and photochemical reduction [15]. Among these techniques, electrochemical conversions of CO_2 to reduced compounds are one of the strongest methods to elicit information about the necessity parameters like overpotential, and widely investigated.

Metal electrodes

The history of electrochemical reduction of CO_2 is very long; more than 100 years has passed since Royer reported the production of formic acid during the electrolysis of sodium bicarbonate in 1870 [16]. In 1985, Hori et al. [17] investigated the CO_2 reduction activity of various metal electrodes in aqueous condition and found that Cu electrode possess specific catalytic activity producing CH_4 and even ethylene (table.1). Inspired by this finding, numerous numbers of researches concerning Cu electrodes by both catalyst modifications [18-23] and theoretical/mechanistic approaches have been conducted [24-26].

Generally speaking, the required overpotential to promote CO_2 reduction on Cu electrode is quite large (> 1 V) in aqueous condition and the mechanism and/or the reason for CH_4 production on Cu electrodes is still under discussion. Nørskov et al. [25,26] tackled to these problems by Density Functional Theory (DFT) calculation and a computational hydrogen electrode (CHE) model. Base on the calculation results, they suggested that the key step for CH_4 production is the protonation step of adsorbed CO intermediate to form adsorbed CHO species (fig.2)[25]. They also suggested that the materials which can stabilize adsorbed CHO relative to adsorbed CO are

promising catalyst to decrease overpotential. The materials hopefully should satisfy the properties that they can bind CHO more strongly and CO with similar tendency compared with Cu to produce CH_4 because weaker CO binding results in CO production. Further calculations by Nørskov et al. [26] demonstrate that Cu is the most suitable metal electrodes among examined metals (Pt, Rh, Pd, Ni, Au, Ag) based on the volcano-type relationship between binding energy of CO and limiting potentials. With the aid of these theoretical approaches, researches in this field have shown large progress. Recently, Kanan et al. [23] achieved the electrochemical reduction of CO_2 with an overpotential less than 0.4 V at the current density of 1 mA/cm^2 for CO_2 reduction utilizing Cu electrodes prepared by annealing of Cu foil in air and electrochemical reduction of resulting Cu_2O. The CO_2 reduction activity largely depends on the initial thickness of Cu_2O and the modified electrode exhibited high stability over several hours, while a polycrystalline Cu electrode deactivated within 1 hour. Furthermore, the same group achieved [27] the CO_2 reduction to CO with an overpotential of 140 mV in aqueous solution by Au nanoparticles derived from electrochemically prepared Au oxide (Au_2O_3).

Metal Electrode	Electrode Potential (V vs. SHE)	Faradaic Efficiency/ %			Lower Limit/Upper Limit	
		$HCOO^-$	CO	CH_4	H_2	Total
Cd	-1.66 ± 0.02	65.3/ 67.2	6.2/ 11.1	0.2	14.9/ 22.2	93/ 100
Sn	-1.40 ± 0.04	65.5/ 79.5	2.4/ 4.1	0.1/ 0.2	13.4/ 40.8	94/ 110
Pb	-1.62 ± 0.03	72.5/ 88.8	0.3/ 0.6	0.1/ 0.2	3.8/30.9	94/ 100
In	-1.51 ± 0.05	92.7/ 97.6	0.9/ 2.2	0.0	1.6/ 4.5	93/ 102
Zn	-1.56 ± 0.08	17.6/ 85.0	3.3/ 63.3	0.0	2.2/ 17.6	90/ 98
Cu	-1.39 ± 0.02	15.4/ 16.5	1.5/ 3.1	37.1/ 40.0	32.8/ 33.0	87/ 92
Ag	-1.45 ± 0.02	1.6/ 4.6	61.4/ 89.9	0.0	10.4/35.3	99/ 106
Au	-1.14 ± 0.01	0.4/ 1.0	81.2/ 93.0	0.0	6.7/ 23.2	100/ 105
Ni	-1.39	0.3	0.0	1.2	96.3	98
Fe	-1.42	2.1	1.4	0.0	97.5	101

Table.1 CO_2 reduction products on metal electrodes in aqueous solution reported by Hori et al. [17].

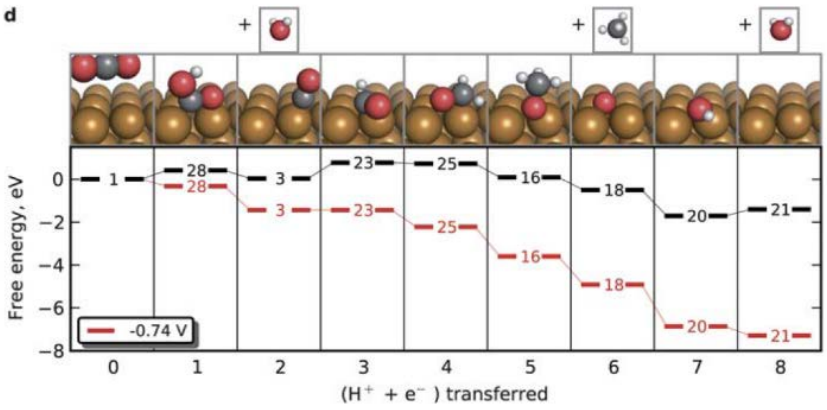

Fig.2 Free energy diagram for CH_4 production from CO_2 on Cu electrode (Reprinted with permission from ref. 25. Copyright 2010, Royal Society of Chemistry).

Metal complex catalysts

To achieve both high selectivity and low overpotential, metal complex catalysts have been developed since 1980s [14, 28,29]. In 1980, Eisenberg et al. [28] reported the first demonstration of indirect CO_2 reduction mediated by metal complexes utilizing tetraazamacrocyclic complexes of Co and Ni. They achieved the production of CO and H_2 with ratio of 1 : 1 or 2 : 1 as the CO_2 reduction under the mixed solvent of water and acetonitrile (v/v = 2 : 1). Efficient CO production under pure aqueous condition was achieved by Ni cyclams (1,4,8,11- tetraaazacyclotetradecane) systems and the series of this compound categorized to one of the most efficient CO_2 reduction metal organics catalysts in terms of CO_2 to CO selectivity [30-32]. The electrocatalytic properties for CO_2 reduction of Ni $cyclam^{2+}$ were first examined by Sauvage et al. [30] and they achieved high coulombic efficiency for CO production of over 90 % at – 1.0 V vs SHE under aqueous condition (pH = 4.1) with Hg electrode. The CO_2 reduction efficiency was further improved by di-nuclear Ni_2(biscyclam)$^{4+}$ complex [31]. This compound catalyzed CO_2 to CO with no other product under aqueous condition, while 75 % of $HCOO^-$ production was observed in addition to

CO production when the electrochemical reduction was conducted in dimethylformamide (DMF) with small concentration of water (< 0.2 %). While the major product of electrochemical CO_2 reduction with Ni cyclam complexes is CO described above, Jäger et al. [32] reported the selective reduction to oxalate with Ni cyclam complexes substituted by COOEt or COMe.

In parallel with catalyst design, mechanistic studies have also conducted for CO production with Ni cyclam systems [33-35]. Sakaki [33] conducted *ab initio* Molecular Orbital study for the model complex of CO_2-binding Ni cyclam, $NiF(NH_3)_4(\eta^1\text{-}CO_2)$. In this study, electron donation from d orbital of Ni to $p\pi^*$ orbital of CO_2 occurred in the intermediate $Ni^I(NH_3)_4(\eta^1\text{-}CO_2)$ species, resulting in the increase of nucleophilicity of O atom of binding CO_2. This model is consistent with the proposed reaction mechanism by Sauvage et al. [30] that binding CO_2 extracted H^+ and the following electron insertion produced CO as shown in fig.3. Rodgers et al. [34] demonstrated that pulse radiolysis and laser flash photolysis to obtain the thermodynamic and kinetic insights of CO_2 and H^+ binding to Ni cyclam in aqueous solution. They explained that the origin of high selectivity for CO_2 reduction with Ni cyclam against H^+ reduction is the more favorable binding of CO_2 to the complex than H^+ at pHs more than 2. Calculations by Fujita et al. [35] showed that N-H proton in the macrocycle contributed to the stabilization of CO_2 by H-bonding, and the singly and doubly occupied molecular orbitals form σ-bonding between C of CO_2 and Ni.

Furuya et al adopted a gas diffusion electrode system and demonstrated the urea formation by the simultaneous reduction of CO_2 and NO_2^- or NO_3^- [36-38]. When they applied negative potential to electrodes modified by various metal or metal-phthalocyanine complex (metal = Al, Ti, V, Cr, Mn, Fe, Co, Ni, Cu, Zn, Ga, Ge, Mo, Ru, Rh, Pd, Ag, Cd, In, Sn, Pt, Au, Tl, Pb) with NO_2^- or NO_3^- in an electrolyte and CO_2 in a gas compartment, urea formation was observed for electrodes modified with Cu, Zn, Pd, Ag, Cd, In, Sn, Au, Tl, Pb metals and Fe-, Co-, Ni-, Cu-, Zn-, Ga-, Pd-, Cd-, In-, Sn-, Pb-phthalocyanine electrodes. The experiments in the presence of CO instead of

CO_2 or NH_3 instead NO_2^-/NO_3^- resulted in the no formation of urea, indicating the intermediate species for CO_2 reduction and NO_2^-/NO_3^- reduction was essential for urea formation.

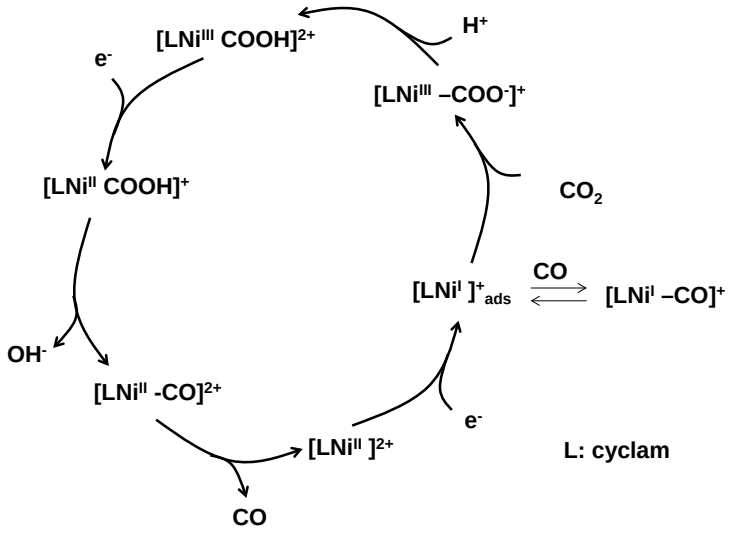

Fig.3 Proposed reaction mechanism for electrochemical CO_2 reduction on Ni cyclam under aqueous condition [30].

Organic molecules

Not only metal organic molecules, but pure organic molecules work as the electron mediator for CO_2 reduction [29, 39]. In 1994, Seshadri et al. [40] reported the electrochemical reduction of CO_2 to methanol with the coulombic efficiencies of 30 % and overpotential of less than 200 mV in the presence of pyridine with hydrogenated Pd electrodes. Morris et al. [41] further studied in detail the pyridine-catalyzed CO_2 reduction system as a function of catalyst concentration, temperature, and pressure with Pt electrode and the reaction kinetics with first order in both CO_2 and pyridine was observed. Combined the experimental results with DFT calculations, they proposed the intermediated is carbamate species and the Lewis basicity of the pyridyl N and the

stabilization of carbon-based free radical at the electrode surface were the key factors to determine the catalytic activity. Further calculation by Keith et al. [42] revealed that the active species was a surface-bound dihydropyridine (DHP), not pyridinyl radical in solution (fig.4).

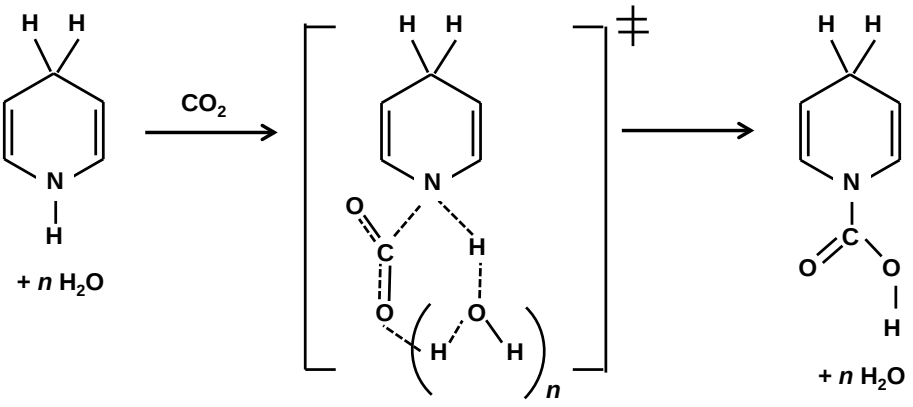

Fig.4 H^+/CO_2 exchange reaction on DHP species [42].

Recently, efficient electrochemical CO_2 reduction in the presence of ionic acid was reported by Rosen et al [43]. They conducted electrochemical CO_2 reduction with an Ag cathode in an ionic liquid electrolyte and achieved the overpotential of less than 0.2 V and columbic efficiencies of more than 96 % for CO production. They utilized 1-ethyl-3-methylimidazolium fluoroborate (EMIM-BF_4) with the expectation of the complex formation with CO_2 to stabilize intermediate CO_2^- radical species. This report boosted up the development of ionic liquid-related CO_2 reduction systems [44-49].

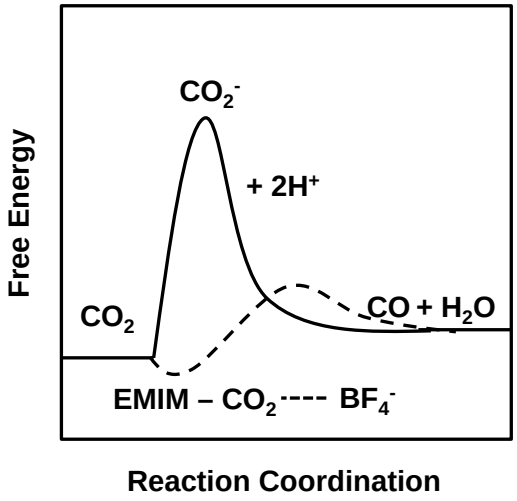

Fig.5 Schematic energy diagram of CO_2 reduction to CO in the absence (solid line) and presence of (dashed line) EMIM-BF_4 [43].

These results of both catalyst design and analytical, theoretical approach described here in previous studies clearly indicate that the rational design to regulate CO_2 reduction intermediate is one of the promising approaches for efficient CO_2 reduction. For Cu electrode case, the protonation of reaction intermediate determines the overpotential of the total reaction, the regulation of the process could achieve the control of the reaction selectivity. The key feature of the ionic liquid in electrochemical CO_2 reduction is the lowering the activation energy to produce CO_2^- radical intermediate by coordination. Therefore, the approach to regulate the intermediate species can be applicable to both organometalic molecular and bulk electrode systems.

1.4.2 Carbon Monoxide dehydrogenaze (CODH)

During the process of CO respirations in acetate producing bacteria, Carbon monoxide dehydrogenaze (CO) catalyzes the oxidation of CO to CO_2 coupled with the reduction of proton to H_2 and the required energy for microbial activity is produced ($CO + H_2O \rightarrow CO_2 + H_2$, $\Delta G^{0'}$ = - 20 kJ/mol)[50]. The CODH can be classified mainly to two types, namely, Mo-containing CODH for aerobic bacteria [51], and Ni-containing CODH for anaerobic bacteria [52]. The crystal structure of CODH was first reported by Dobbek et al. in 1999 [53] for aerobic bacterium, *Oligotropha carboxidovorans*, with the resolution of 2.2 Å (fig.6 left). The active site revealed to be composed of molybdopterin-cytosine dinucleotide, S-selanylcysteine connecting to [2Fe-2S] cluster and flavin-adenine dinucleotide. The crystal structure of CODH for anaerobic bacteria was also reported by H. Dobbek et al. in 2001 [54] for *Carboxydothermus hydrogenoformans* with the resolution of 1.63 Å (fig.6 right). This enzyme consists of cubane-type [4Fe-4S] clusters called B-cluster and D-cluster and the active site is asymmetric [Ni-4Fe-5S] cluster called C-cluster.

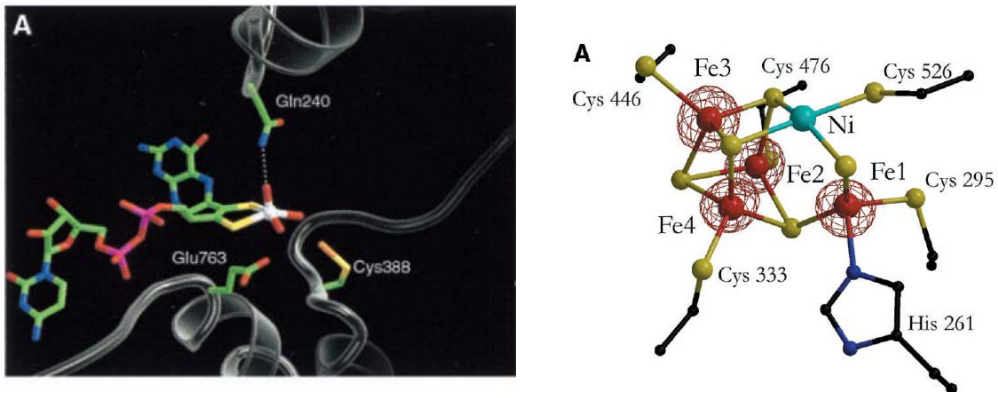

Fig.6 Crystal structure of the active centers of (left) Mo-containing CODH for aerobic bacteria (H. Dobbek et al., *Proc. Natl. Acad. Sci. USA,* **1999,** *96,* 8884-8889, copyright by the National Academy of Sciences) and (right) Ni-containing CODH for anaerobic bacteria (Reprinted with permission from ref. 54. Copyright 2001, American Association for the Advancement of Science) revealed by Dobbek et al.

Ni L-edge X-ray spectroscopy revealed [55] that the Ni site in CODH isolated from *Clostridium thermoaceticum* is low-spin Ni(II), and that upon CO treatment, the Ni site is converted to high spin Ni(II) and/or Ni(I). This is distinct from Ni-Fe cluster of hydrogenase, whose reduced form contains high spin Ni(II) [56]. CO and H_2O are reacted on the C-cluster, and generated electrons are transferred to the D-cluster via B-cluster. In addition to these Fe-S clusters, some kinds of Ni-CODH possess another Fe-S cluster called A-cluster, which synthesizes acetyl-CoA utilizing the CO. This complex composed of Ni-CODH and acetyl-CoA synthase (ACS) reduce CO_2 and generated CO is utilized for acetyl-CoA synthesis (CH_3-CFeSP + CO + CoA $\rightarrow$ acetyl-CoA + CFeSP, CFeSP: corrinoid iron-sulfur protein) [57]. The turnover frequencies (TOF) of Ni-containing CODH for CO oxidation is reported to be approx. 40000 /s in pH = 8, 70 °C [58], while TOF of Mo-containing CODH is 100 s^{-1} [59]. The reaction mechanism of the CO oxidation of CODH is still under discussion, and the representative one is hydride-forming pathway [60]. First, CO is bind to the Ni site, and a proton is extracted form an OH group binding to Fe site neighboring the Ni site, forming Fe-O-C bonding. By binding the extracted proton to the Ni site, hydride species is formed, and the reductive dissociation of CO_2 occurs. The catalytic cycle is terminated by the binding of OH^- extracted from water to Fe site after H_2 released by the reaction between the hydride and a proton (fig.7).

Shin et al. applied the CODH to electrochemical CO_2 reduction system by combining CODH and methyl viologen as an electron mediator [61]. They achieved the efficient CO_2 reduction to CO with the overpotential of less than 100 mV and the coulombic efficiencies of almost 100 % at pH = 6.3. In 2007, Armstrong et al. [62] confirmed the reversible conversion (CO $\Leftrightarrow$ CO_2) properties of the CODH under aqueous environment by grafting the enzyme on to the surface of glassy carbon electrode and also achieved the reduction of CO_2 to CO with the overpotential of less than 100 mV and the coulombic efficiencies of almost 100 % in electrochemical systems.

They also expand the CODH-CO_2 reduction system to a photochemical system by utilizing $[Ru^{II}(bipy)_2(4,4'\text{-}(PO_3H_2)_2\text{-}bipy)]Br_2$ (RuP; bipy = 2,2'-bipyridine) as a photo-sensitizer and TiO_2 nano particles as electron conduit [63]. Here, a irradiation of visible light linger than 420 nm sensitizes the RuP and the excited electron was transferred to the CODH site via a conduction band of TiO_2 nanoparticle to reduce CO_2 to CO, while the generated hole were scavenged by 2-(*N*-morpholino) ethanesulfonic acid (MES) (fig.8).

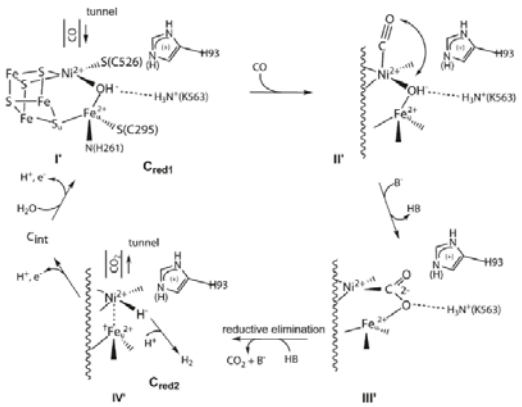

Fig.7 Possible mechanism of CO oxidation by CODH proposed by Amara et al.(Reprinted with permission from ref. 60. Copyright 2011, American Chemical Society).

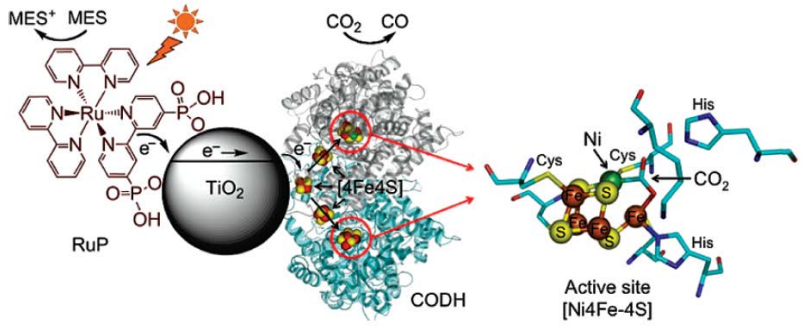

Fig.8 CODH-CO_2 photochemical reduction system composed of $[Ru^{II}(bipy)_2(4,4'\text{-}(PO_3H_2)_2\text{-}bipy)]Br_2$ (RuP; bipy = 2,2'-bipyridine) as a photo-sensitizer and TiO_2 nano particles as electron conduit constructed by Armstrong et al. (Reprinted with permission from ref. 63. Copyright 2010, American Chemical Society)

1.4.3 Biomimetic approaches to CO_2 reduction catalysts

Inspired by enzymatic CO_2 fixation center, structure-mimetic approaches especially for Fe-S cubane cluster have been taken to synthesize CO_2 reduction catalysts. Hidai et al. synthesized Fe-S cubane cluster, $[Fe_4S_4(SR)_4]^{2-}$ (R = $CH_2C_6H_5$ or C_6H_5), and conducted electrochemical CO_2 reduction in *N*, *N*-dimethylformamide (DMF) [64] (fig.9a). They observed the decrease of overpotential of approx. 700 mV by the addition of the cluster on a mercury pool electrode. The reaction product was mainly oxalate, but the addition of small amount of water increased the production rate of formate and CO. Tanaka et al. synthesized a metal-sulfur cluster [65] composed of Mo, Fe and S ($[Mo_2Fe_6S_8(SEt)_9]^{3-}$) inspired by a reductive carboxylic cycle in photosynthetic bacteria (fig.9b). The model reaction of α-keto acid synthesis proceeded in the presence of the cluster under acetonitrile with the applying electrode potential of -1.55 V vs SCE: $RC(O)SEt + CO_2 + 2e^- \rightarrow RC(O)COO^- + EtS^-$ (R = CH_3, C_2H_5, C_6H_5). In addition to the α-keto acid synthesis, the model reaction of β-keto acid synthesis was also promoted by $[Fe_4S_4(SPh)_4]^{2-}$ or $[Mo_2Fe_6S_8(SPh)_9]^{3-}$; $8PhC(O)CH_3 + 8CO_2 + 2NO_2^- + 6e^- \rightarrow 8PhC(O)CH_2COO^- + N_2 + 4H_2O$ [66]. In 2011, Kanatzidis et al. reported [67] the chalcogel-type material in which Fe-S cubane cluster and transition metals (Pt, Co, Ni, Sn, Zn) were connected by Sn-S cluster (fig.9c). The electrochemical CO_2 reduction measurement in DMF tended to be higher when Ni and Co were utilized as transition metal sites.

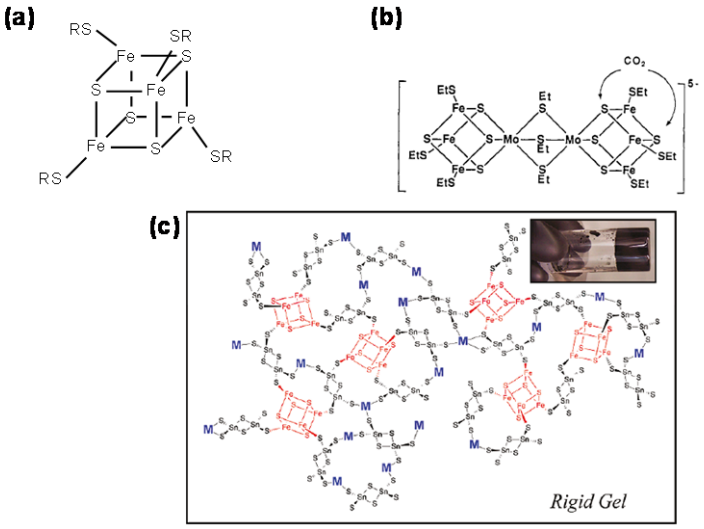

Fig.9 Biomimetic CO_2 reduction Fe-S clusters synthesized by (a) Hidai et al. [64], (b)Tanaka et al. (Reprinted with permission from ref. 65. Copyright 1992, American Chemical Society), and (c) Kanatzidis et al. (Reprinted with permission from ref. 67. Copyright 2011, American Chemical Society)

Not only synthesizing approaches, but computational approaches have been done to clarify the important factor of catalytic activity of CODH. Nørskov et al. [68] performed a mechanistic study of electrocatalytic CO_2 reduction with $[Fe_4S_4]$ cubane cluster especially for the effect of Ni substitution and/or structural change using Density Functional Theory (DFT) calculation. They observed that the activation energy for the CO_2 reduction to CO via COOH* intermediate is largely decreased by substitution of one Fe atom to Ni while the activation energy to HCOOH via OCHO* intermediate is not affected (fig.10). They explained that the Ni substitution alters the chemical environment in the COOH* binding because the COOH* binds to only S site in $[NiFe_3S_4]$ cluster while it binds to both S and Fe in $[Fe_4S_4]$ cluster. Further decrease of activation energy was observed by further Ni substitution, but only one or zero Ni-substituted cluster were predicted to be stable during the catalytic cycle.

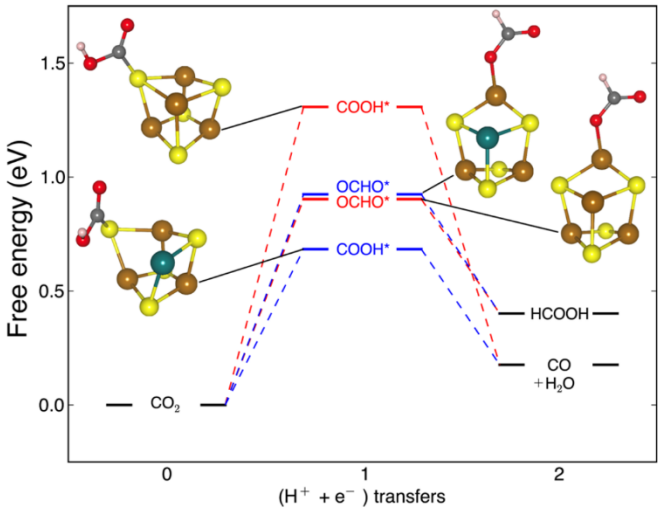

Fig.10 Free energy diagram for CO_2 reduction on $[Fe_4S_4]^{2-}$ (red) and $[NiFe_3S_4]^{2-}$ (blue) cubane complexes based on DFT calculation reported by Nørskov et al. (Reprinted with permission from ref. 68. Copyright 2013, American Chemical Society)

While the Fe-S cubane clusters are widely investigated as partly described in this chapter, the physicochemical origins of the efficient CO_2 reduction activity of the CODH, natural CO_2 reduction catalysts, are remained unexplored. Therefore, the further investigation in term of both catalyst design and theoretical approach is further demanding.

1.4.4 Prebiotic organic synthesis on metal sulfides

Near a hydrothermal vent in deep sea floors, diverse ecosystems are sustained by the chemical energy supplied by hydrothermal fluid [69] and the deep sea environment operates as the reaction field for one of the two essential energy conversion systems in nature. Not only for the present ecosystem, but for the primordial earth, it is considered that the hydrothermal environment played a crucial role to promote the emergence of life. Although whether the primordial life was autotrophic or heterotrophic is under discussion, hypothesize concerning the autotrophic origin has been proposed widely since the discovery of a hydrothermal vent in 1970s [70]. One of the main problems of the autotrophic origin theory is the first process of carbon fixation. Wächtershäuser reported his model concerning the autotrophic origin [71, 72], in which CO_2 is reduced on the surface of a pyrite (FeS_2). H_2S or HS^- released from the hydrothermal vent reacts with dissolved Fe^{2+} to produce iron sulfides including pyrite and the reaction proceeds on the glowing pyrite. He argued that the produced organic molecules are self-organized and form the first metabolizing cell. The driving force of the CO_2 reduction is the oxidative formation of pyrite ($4CO_2 + 7H_2S + 7FeS \rightarrow (CH_2\text{-}COOH)_2 + 7FeS_2 + 4H_2O$, ΔG^O = - 420 kJ/mol). The hypothesis is supported by a series of experimental observations like thiol (CH_3S^-) formation from CO_2 in the presence of FeS [73], acetic acid formation from CH_3SH and CO on iron-nickel sulfide (fig.11)[74], and peptide formation from amino acids with CO and iron-nickel sulfide [75].

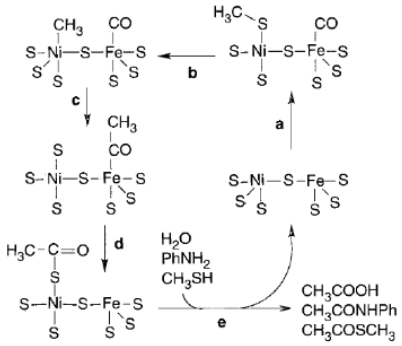

Fig.11 A hypothetical reaction mechanism of acetic acid formation from CH_3SH and CO on iron-nickel sulfide (Reprinted with permission from ref. 74. Copyright 1997, American Association for the Advancement of Science)

In contrast to the Wächtershäuser's hypothesis, Russell proposed his model that CO_2 in ocean water reacts with H_2 from alkaline hydrothermal fluid in three-dimensional compartments whose walls are composed of iron sulfide [76]. Main difference between Wächtershäuser's and Russell's hypothesis is that Wächtershäuser considers the FeS as an energy source to reduce CO_2, while Russell does the FeS as the components for the compartment and H_2 as an electron donor. Not only as cavity, but iron sulfides such as Nickelian mackinawite ($FeNiS_2$), Ni-containing greigite ($NiFe_5S_8$), and violarite ($FeNi_2S_4$) acted as the catalysts for CO_2 reduction with the structural similarity to [Ni-Fe] hydrogenase for Nickelian mackinawite, C-cluster in CODH for greigite and ACS active site A-cluster for violarite (fig.12) [77]. It is hypothesized that H_2 adsorbed onto and/or absorbed into the cubane sites of the minerals and dissociated into a proton, an electron, and a reactive hydrogen atom ($H^{\cdot}$). The generated hydrogen atom reduced CO_2 to CO. Then, the CO reacted with methane thiol (CH_3SH) produced in the crust [71] to produce thioester acetyl methylsulphide, hydrolyzed to acetate [74] (eq. 10-12).

$$2H^{\cdot} + CO_2 \rightarrow CO + H_2O \quad (10)$$

$$CO + 2CH_3SH \rightarrow CH_3CO(SCH_3) + H_2S \quad (11)$$

$$CH_3CO(SCH_3) + H_2O \rightarrow CH_3COOH + CH_3SH \quad (12)$$

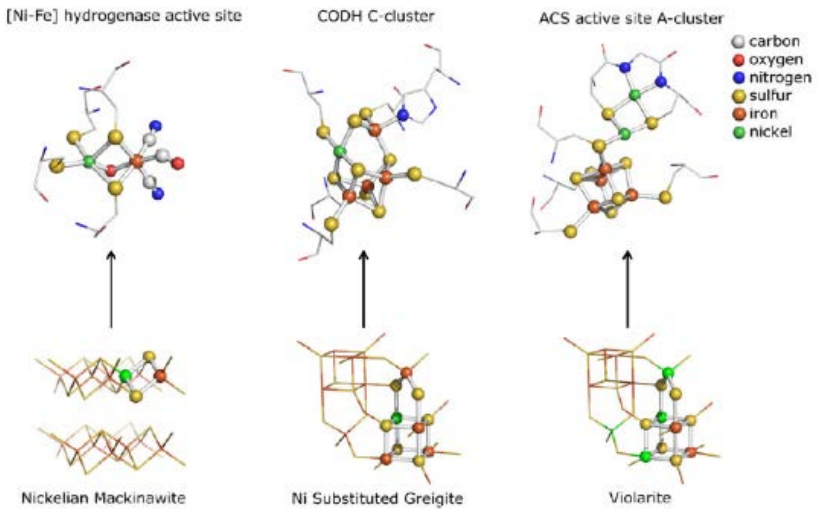

Fig.12 Structural similarity between the natural sulfide nickelian mackinawite on the bottom left, greigite on the center, and violarite on the right with the active centers of early metalloenzymes: [Ni-Fe] hydrogenase on the top left, C-cluster in (CODH) on the center and ACS active site A-cluster on the right, respectively (Reprinted with permission from ref. 77. Copyright 2013, Elsevier B. V.)

As introduced in this section, iron sulfides, especially greigite, are proposed to be essential for the primordial organic synthesis. However, the electrochemical CO_2 reduction property of greigite has never been examined. The discussion in this field is based on the thermodynamic relations, and the kinetic consideration is hardly conducted. Thus, the investigations of the electrochemical property of greigite bring further insight concerning both the efficient catalyst design and the primordial organic synthesis.

1.5 O_2 evolution catalysts

1.5.1 Electrochemical O_2 evolution catalysts

O_2 evolution reaction from water is at the heart of not only natural photosynthetic process but also artificial water splitting systems. The examination methods for water oxidation properties of catalysts can be classified into mainly three categories; electrochemical, photochemical, and photoelectrochemical techniques. Compared with other two techniques, electrochemical technique possesses the advantages to evaluate intrinsic catalytic properties without the interference of the effect of the diffusion of catalysts and/or the diluteness of photon flux.

Noble metal catalysts

In general, noble metal-based catalysts like IrO_2 and RuO_2 exhibit high catalytic activity. Trasatti et al. [78] first reported a RuO_2-based catalyst prepared on titanium in 1971. The film electrode exhibited high OER activity with an overpotential at 10 mA cm^{-2} of 200 mV in 1 M $HClO_4$. This report has inspired the development of large numbers of colloidal and heterogeneous RuO_2-based O_2 evolution catalysts [79,80]. IrO_x also demonstrate both high catalytic activity and stability [79,81,82]. Yagi et al. [83] prepared a monolayer of citrate-stabilized IrO_2 nanoparticles (50-100 nm) deposited on an ITO electrode in 2005 and the electrode exhibited high water oxidation activity with an onset potential of 1.2 V vs SHE at pH 5.3. Further enhancement of activity (an overpotential of 150-250 mV at 0.5 mA cm^{-2} and a current efficiency of 100% at an overpotential of 250 mV) was achieved with over a pH range of 1.5 to 13 by decreasing the particle size (1.6 ± 0.6 nm [84,85].

3d block metal element-based catalysts

Among 3d block metal elements, CoO_x complexes have been found to demonstrate high catalytic

activity for O_2 evolution at neutral pH under both heterogeneous and homogeneous conditions since the early 1980s [86-88]. Nocera et al. [87] reported the *in-situ* formation of a catalytic film composed of cobalt phosphates, hydroxide, and oxides upon application of a positive potential to an ITO electrode under neutral condition in the presence of Co^{2+} and phosphate ions in 2008. The Co-based catalyst catalyzes water oxidation with an overpotential of 410 mV at 1 mA cm^{-2} at pH 7. Furthermore, it is reported that cubic Co_3O_4 nanoparticles (5.9 ± 1.0 nm) showed an electrochemical water oxidation activity with an overpotential of 330 mV at 10 mA cm^{-2} under alkaline conditions [88].

Theoretical approaches

Not only fabrications of catalysts, but theoretical approaches have been taken to develop efficient water oxidation catalysts based on 3d block metal elements [89-91]. One possible parameter to determine the water oxidation activity is metal ion (M)-OH bond strength as reported by Rüetschi et al. in the early 1950's [89]. They found that the overpotential for O_2 evolution linearly decreases with increasing M-OH bond energy through the theoretical investigation for the water oxidation activity under alkaline conditions of several types of noble-metal (Ag, Au, Cd, Pb, Pd, Pt) and 3d block metal (Co, Cu, Fe, Ni,) electrodes.

Another candidate for determinant is the electron occupancy of the e_g orbital in active metal sites. Iwakura et al. [90] reported that the water oxidation activity of spinel transition metal oxides ($Co_xFe_{3-x}O_4$, $Mn_xFe_{3-x}O_4$, and $Ni_xFe_{3-x}O_4$) increases with the number of unpaired d-electrons when the generation of OH radical via oxidation of OH^- ($HO^- \rightarrow HO^\bullet + e^-$) is the rate-determining step, while it decreases with the unpaired d-electron number in case the reaction between OH radical and OH^- is the rate-determining step. Bockris et al. [91] explored the relationship between the water oxidation activity of 18 perovskite-type oxides and various parameters, like the effective

magnetic moment, formation enthalpy of the corresponding hydroxides, M-OH bond strength, and d-electron numbers. They concluded that the water oxidation activity has relevance to the occupancy of the antibonding orbitals of M-OH. Furthermore, they predicted a volcano-like relationship between the catalytic activity and M-OH bond strength based on their theoretical results. In 2011, Shao-Horn et al. [92] investigated the water oxidation activity of more than 10 metal oxides with perovskite structure and found that the activity depends on the occupancy of an e_g orbital of metal cations in a volcano-like manner. Based on the result, they predicted that metal oxides which possess 1 to 1.5 electron in their 3d e_g orbital is the most suitable catalysts (fig.13). Indeed, they synthesized $Ba_{0.5}Sr_{0.5}Co_{0.8}Fe_{0.2}O_{3-\delta}$, as such a material, and the perovskite metal oxide exhibits water oxidation activity with an overpotential of 250 mV at current density of 50 μA cm^{-2} under alkaline conditions.

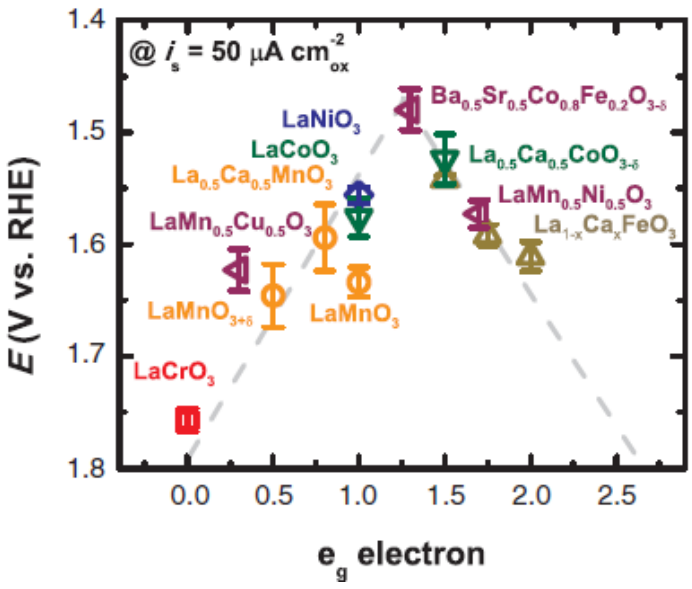

Fig.13 The volcano-like relationship between the water oxidation activity and the occupancy of the e_g orbitals of the transition metal (B in ABO_3) under alkaline condition. (Reprinted with permission from ref. 92. Copyright 2011, American Association for the Advancement of Science)

These studies indicate that the d-band model is effective for the catalytic design of water oxidation reaction with 3d metal elements under alkaline conditions [89-92].

The situation is, however, completely different for the neutral pH conditions. For instance, Raabe et al. [93] revealed that an amorphous $Pr_{1-x}Ca_xMnO_3$ (PCMO) layer formed at the surface of PCMO with a concomitant decrease of O_2 evolution activity during the catalytic cycle at pH 7 by using *in-situ* transmission electron microscopy (TEM). Furthermore, the valence of the Mn site was altered from 3.2 to 2.0 during the water oxidation reaction revealed by *in-situ* electron energy-loss spectroscopy (EELS) analysis. This deactivation tendency at neutral pH cannot be directly explained by the d-band model; thus, new design strategy is required to develop O_2 evolution catalysts with abundant elements which can operate under neutral condition.

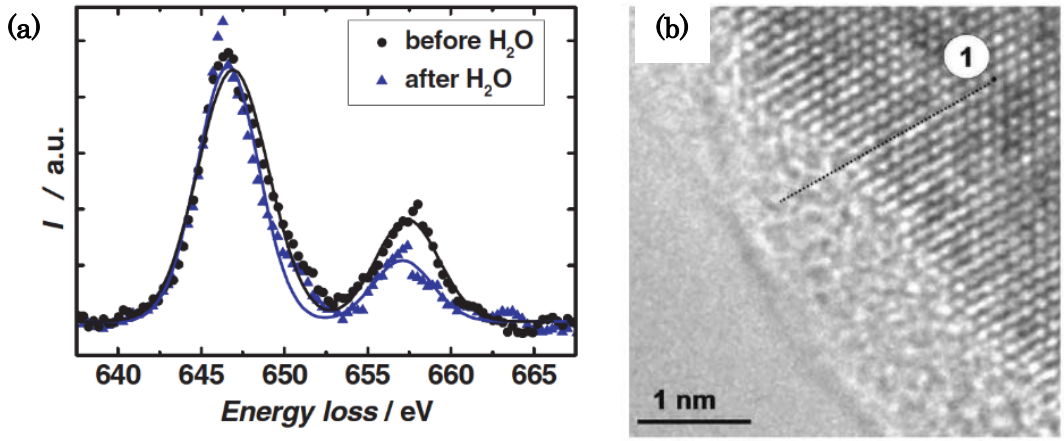

Fig.14 The surface changes of $Pr_{1-x}Ca_xMnO_3$ (x = 0.32) after the water oxidation reaction confirmed by (a) *in situ* EELS and (b) TEM observation (Reprinted with permission from ref. 93. Copyright 2012, WILEY-VCH Verlag GmbH & Co. KGaA, Weinheim).

1.5.2 Mn_4-cluster in Photosystem II (PSII)

Photosynthesis is the two of major energy conversion system in natural ecosystem and O_2 evolution is at the heart of the overall photosynthetic system. O_2 evolution reaction from water in photosynthesis is catalyzed by a $CaMn_4O_5$ cluster (Mn_4-cluster) in a transmembrane protein called D1 subunit of photosystem II (PSII). PSII forms a dimer structure with dimensions of 105 Å depth, 205 Å length, and 110 Å width [94] as shown in fig.15 for PSII isolated from *Thermosynechococcus elongatus*. The Mn_4-cluster is located on the lumen side of the thylakoid membrane and surrounded by three extrinsic proteins, PsbO (33 kDa), PsbP (23 kDa) and PsbQ (17 kDa). PsbP and PsbQ are substituted by PsbV (17 kDa) and PsbU (12 kDa) in cyanobacteria [95, 96].

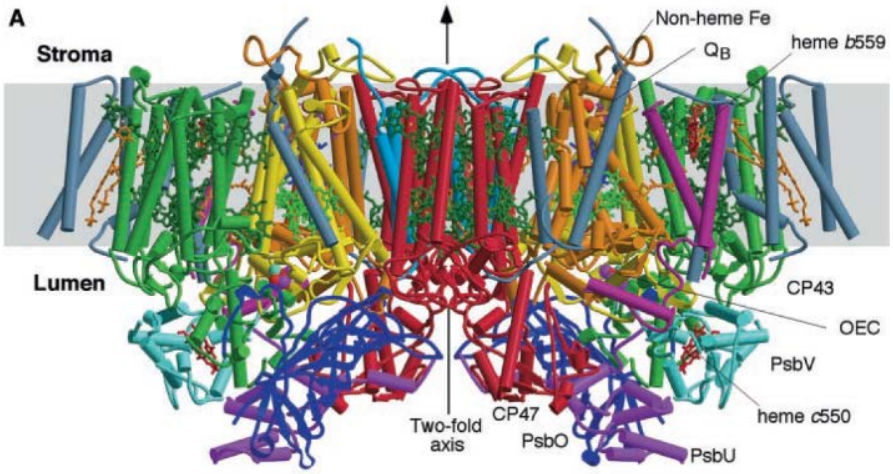

Fig.15 Overall structure of PS II (Reprinted with permission from ref. 94. Copyright 2004, American Association for the Advancement of Science)

In 1970, Kok et al. examined [97] an O_2 evolution reaction of isolated chloroplast by light flash techniques and observed that light flash always produce the same number of oxidizing equivalent and when the four oxidizing equivalents were accumulated, O_2 evolution occur. Based on the observation, they suggested catalytic cycle, referred to as Kok cycle. In the cycle, the O_2 evolution center (OEC) is sequentially oxidized by four photogenerated oxidizing equivalents. The determination of oxidation states of the intermediates, denoted as S_n states (n = 0−4), have been tackled by various spectroscopic methods like X-ray absorption near edge spectroscopy (XANES), Mn K-edge spectroscopy, and electron paramagnetic resonance (EPR) spectroscopy [98-100]. Although they are still under discussion, the oxidation states of the intermediates are common assigned from S_0, $3Mn^{III}$ Mn^{IV}, to S_4, which is a putative $3Mn^{IV}$, Mn^{V}, or $4Mn^{IV}$ -ligand radical that promotes O−O bond formation and O_2 release (fig.16)[101].

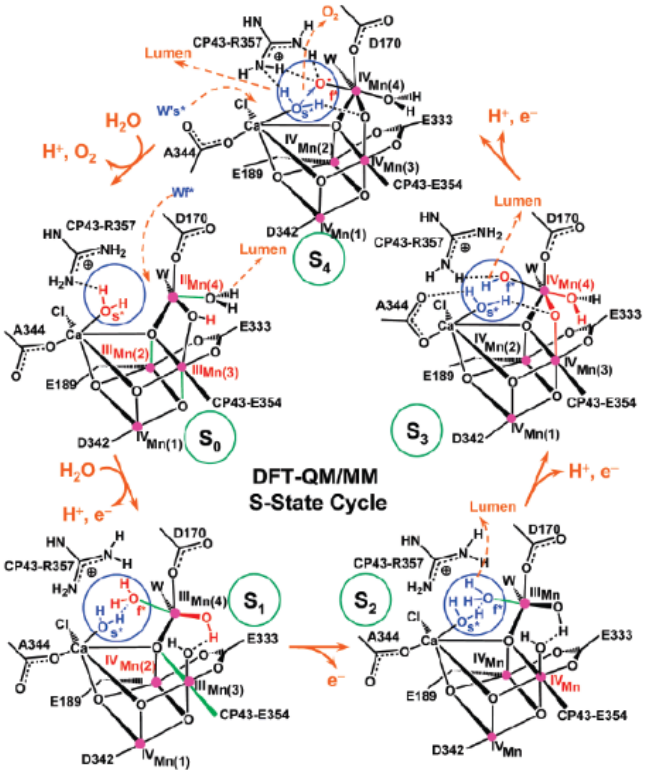

Fig.16 Proposed catalytic cycles of Mn_4-cluster. (Reprinted with permission from ref. 101. Copyright 2008, American Chemical Society)

Oxidation power of OEC has been discussed. Schiller et al examined a pH dependence of oxygen evolution of spinach and *Scenedesmus* PSII particles prepared by their own protocols [102]. Both of samples showed a same pH dependence of activity: the maximum activity was observed at pH = 6.5, while the activity was diminished at less than pH = 4.5 and more than pH = 7.5. Although no information concerning the surrounding pH of OEC at this stage, the redox potential for water oxidation to oxygen is 0.96-0.79 V vs SHE taking the pH range above as the surrounding pH. The redox potential of $P680^+/P680$ and Y_Z^+/Y_Z couples were investigated by the recombination-fluorescence decay and determined to be + 1.25 V and + 1.21 eV, respectively (fig.17) [103-105].

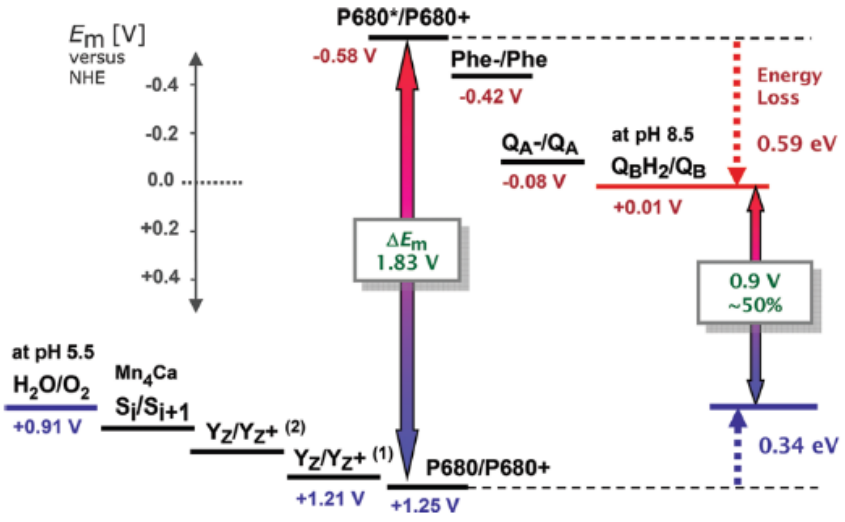

Fig.17 Estimated redox potentials of PS II compositions. (Reprinted with permission from ref. 105. Copyright 2009, American Chemical Society)

Elucidation of the crystal structure of PSII including Mn_4-cluster was one of the hottest research topic in the field about natural photosynthesis. In 2001, Zouni et al. described the X-ray structure of PSII isolated from *Synechococcus elongatus* at 3.8 Å resolution [106] and the resolution was improved to 2.9 Å by the same group [107]. In 2011, Umena et al., reported [108] the crystal

structure of Mn_4-cluster at 1.9 Å including coordinating ligands and surrounding water molecules as shown fig.18. The determination of high-resolution structure allows them to identify the position and configurations of identical atoms. In the structure of $CaMn_4O_5$ cluster, three manganese atoms, one calcium atom and four oxygen atoms construct a cubane-like structure in which the metal atoms occupy the four corners of the cubane while the oxygen atoms occupy the other four corners. The cubane –like cluster is directly coordinated by two aspartic acids (D1-Asp 170, D1-Asp 342), three glutamic acids (D1-Glu 189, D1-Glu 333, CP43-Glu 354), one histidine (D1-His 332), one alanine (D1-Ala 344) and four water molecules. In the second coordination sphere, D1-Asp 61, D1-His 337 and one arginine (CP43-Arg 357) exist. Recently, Suga et al. reported a "radiation-damage-free" structure of PSII in S_1 state isolated from *Thermosynechococcus vulcanus* at a 1.95 Å resolution [109] utilizing femtosecond X-ray pulses of the SPring-8 Å compact free-electron laser (SACLA). The "radiation-damage-free" PSII possesses the 0.1-0.2 Å shorter Mn-Mn bond than previously reported XRD results [108].

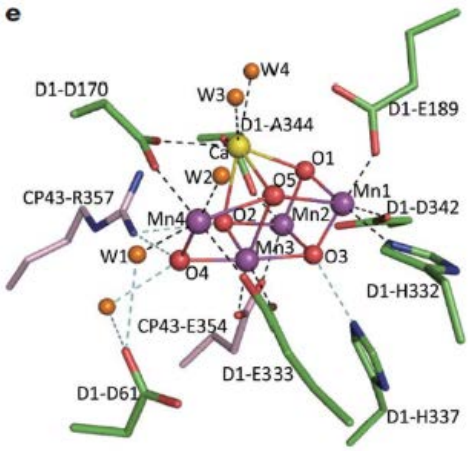

Fig.18 Crystal structure of $CaMn_4O_5$ water oxidation center in PS II revealed by Umena et al. (Reprinted with permission from ref. 108. Copyright 2011, Rights Managed by Nature Publishing Group)

1.5.3 Biomimetic approaches to O_2 evolution catalysts

In spired by OEC in PSII, various kinds of manganese oxide cluster which possess bi-nuclear, tri-nuclear, and tetra-nuclear manganese centers have been synthesized [110-115]. Especially, tetra nuclear manganese clusters with the cubane structure have been focused on due to their structural similarity with OEC [113-115] since the first all oxo-bridged tetra-nuclear Mn_4O_4 cluster ($Mn_4O_4(O_2P(Ph)_2)_6$) was synthesized by Dismukes et al. shown in fig.19 [111]; however, no O_2 evolution was confirmed with these synthesized manganese clusters. Spiccia et al. observed [114] the photo-anodic current from $[Mn_4O_4L_6]^+$ (L = (p-MeO-Ph)$_2$PO$_2$) embedded in a proton conducting membrane (Nafion) coated onto glassy carbon electrode under UV-visible light (275-750 nm) with applied potential of + 1.00 V vs Ag/AgCl. The proposed mechanism is shown fig.20. In this system, however, the Mn cuban clusters don't retain their original structure as revealed by in situ X-ray absorption spectroscopy and transmission electron microscopy studies [116].

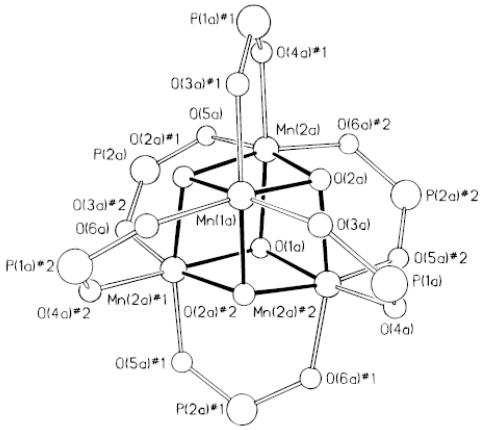

Fig.19 $Mn_4O_4(O_2P(Ph)_2)_6$) synthesized by Dismukes et al. (Reprinted with permission from ref. 111. Copyright 1997, American Chemical Society)

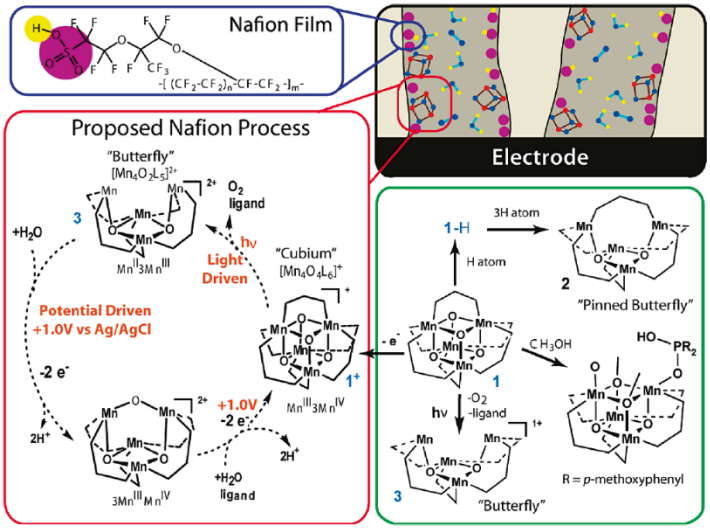

Fig.20 Proposed photoelectrochemical reaction mechanism of $[Mn_4O_4L_6]^+$ (L = (*p*-MeO-Ph)$_2PO_2$) cluster embedded in nafion membrane prepared by Spiccia et al. (Reprinted with permission from ref. 114. Copyright 2009, American Chemical Society)

Not only for organic complex but for bulk MnO_2 systems, the relevance of the structure with OEC to achieve the catalytic O_2 evolution have been discussed [117-120]. δ-MnO_2 (birnessite), which possesses a layered structure, exhibit O_2 evolution from water [116] and comprise puckered, half-cube Mn-O recesses and protrusion [117]. This structural motif is quite similar to OEC (fig.21 left and center), and considered to contribute to water oxidation activity. In 2010, Najafpour et al. reported the synthesis and the catalytic activity for water oxidation of Ca-containing manganese oxides ($CaMn_2O_4$) as biomimetic oxygen evolution catalysts [118]. They demonstrated photooxidation of water using Ce(IV) as an oxidant and $[Ru^{III}(bipy)_3]^{3+}$ as a photo-sensitizer and as the result, Ca-containing manganese oxides exhibited higher activity compared with bare Mn_2O_3 samples. XAS examination revealed that the $CaMn_2O_4$ contains a $CaMn_3O_4$ cubane motif in its structure [119] and identify common features to achieve water oxidation

catalysts based on manganese oxides as (i) a mixed valence of Mn between +3 and +4, (ii) di-μ-oxide bridging involving coordinatively unsaturated μ_2-O(H) bridges between Mn ions in a layered-oxide structure of low order, and (iii) redox-inert cations connected to Mn ions by μ-oxido bridges. Dismukes et al. reported that a conversion of an inactive spinel catalyst ($LiMn_2O_4$) to a photochemically-active water oxidation catalyst (λ-MnO_2) by acidic removal of Li ion [120], the latter oxide possesses a cubane core in the unit cell. They explained that the delithiation process activate the cubane unit by introduction of flexibility of degree of freedom.

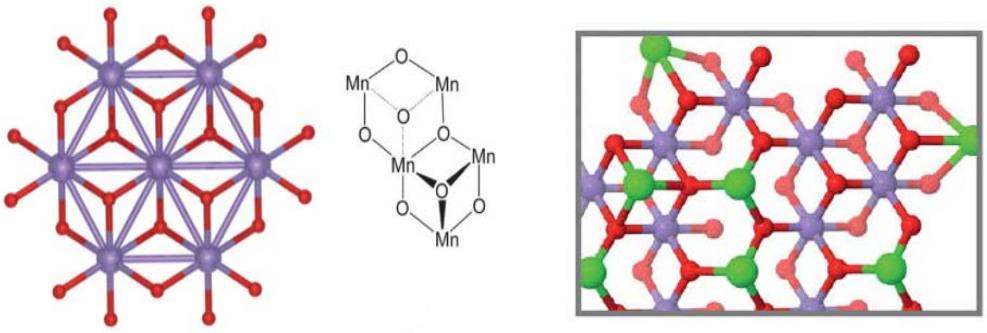

Fig.21 (Left) Crystal structure of birnessite and (center) the structural arrangement of Mn-O sheet layers in birnesite. (Reprinted with permission from ref. 117. Copyright 2011, Royal Society of Chemistry) (right) Hypothetical structure of Ca-containing manganese oxide synthesized by Najafpour et al. (Reprinted with permission from ref. 119. Copyright 2011, Royal Society of Chemistry).

1.5.4 Possible evolutionary origin of OEC

The origin of natural OEC has been discussed [1-4]. Russell et al. suggested that the origin of the Mn_4-cluster is the colloidal cluster of $CaMn_4O_9 \cdot 3H_2O$ generated by the reaction between Mn^{2+} and Ca^{2+} promoted by the super-ultraviolet irradiation [1]. Yachandra et al. have focused on the reported bond length of Mn-Mn in natural OEC (2.7~2.8 Å and 3.3 Å), and investigate the bond length in several Mn-based minerals (fig.22) [2]. Based on these observations, they proposed that the hollandite (mainly composed of α-MnO_2) is the origin of naturally occurring OEC. Their discussions are based on the structural similarity of the Mn-containing minerals to OEC.

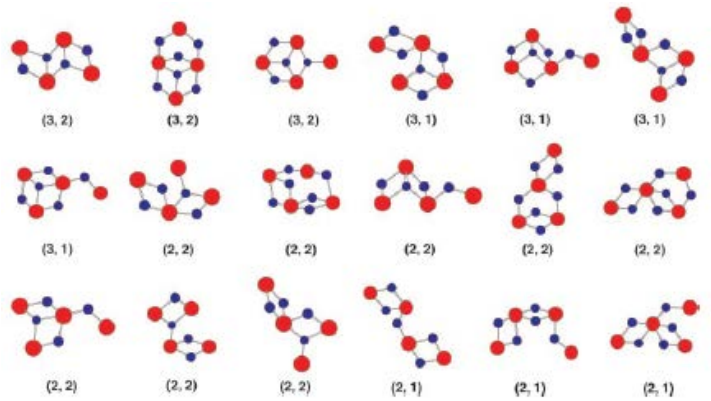

Fig.22 Mn_4-clusters in hollandite which are compatible with that present in OEC. (K. Sauer et al., *Proc. Natl. Acad. Sci. USA*, **2002,** *99*, 8631-8636, copyright by the National Academy of Sciences)

In nature, Mn is the only element which is in charge of O_2 evolution at present. Armstrong considered that the reason why nature chose Mn is its accessibility to various oxidation states [3]. In his review, the concept concerning the evolution of OEC proposed by Dismukes et al. [4] is also introduced. They hypothesized that the precursor for OEC was the Mn(II)-bicarbonate cluster

in the Archean sea considering the composition of the sea. In their hypothesis, $Mn^{II}_2(HCO_3)_4$ served as an electron donor in anoxygenic photosynthesis and the environmental tetramanganese-bicarbonate cluster was bind to the reaction center. Finally, the incorporation of Ca boosted the electrochemical oxidation power to achieve water oxidation as the present OEC. Despite of these hypotheses that the origin of natural OEC is MnO_2-based minerals, the electrochemical water oxidation activity of artificially synthesized MnO_2 catalysts are far away from natural one. This has been the long-standing mystery in this field. To elucidate the origin of the catalytic deactivation of artificial MnO_2 catalysts and educe the function of the natural OEC, the investigation and understanding of the essential physicochemical parameters which provide the natural system with the efficient catalytic activity is promising approach.

1.6 The reaction field surrounding the enzymatic active center

In enzymatic systems, protein environment and the amino acid residue-combinations assist the appropriate electron, proton, and substrate transportations to active centers for stable and efficient catalysis. Concrete examples: carbon monoxide dehydrogenase (CODH) and photosystem II (PSII) in photosynthesis are described in this section. As described in 1.4.2., the reaction center of CODH from *Carboxydothermus hydrogenoformans* reported by Dobbek et al. is [Ni-4Fe-4S] cluster [54], and the cluster is embedded in unquestionably functional protein environments. Hereafter, the term "CODH" means the one isolated from *Carboxydothermus hydrogenoformans.* The overall structure of CODH is composed of the dimer, and each monomer possesses substrate transporting channel with two hydrophobic exit and one hydrophilic end toward the active center (fig.23). The Ni site of active center, which is the possible CO-binding site, is oriented to the exit of the hydrophobic channel, which is the possible CO-path route, as shown in inset of fig.23. Lys^{563} and His^{93} amino acid residues are responsible to this orientation and manage the efficient binding of CO to the active site.

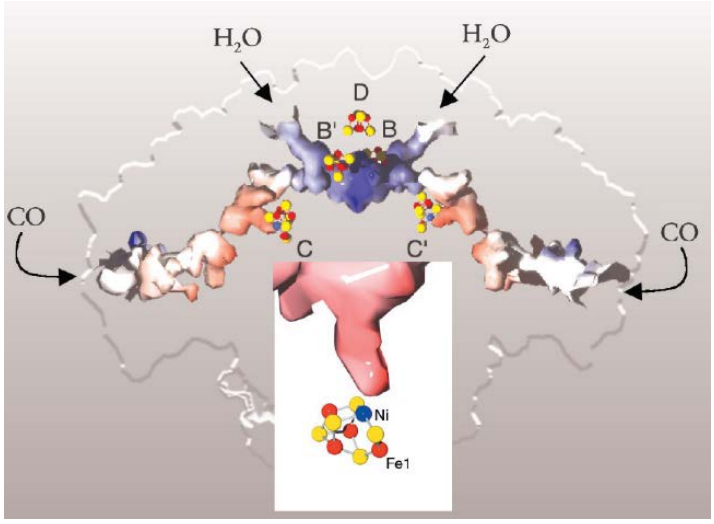

Fig.23 CO and H_2O channel in the CODH dimer. The inset is the active C cluster oriented to the exit of the hydrophobic channel. (Reprinted with permission from ref. 54. Copyright 2001, American Association for the Advancement of Science)

In addition to the active site, C cluster, there are other Fe-S clusters in CODH dimer which constitute electron transfer chain, called B cluster and D cluster. In fig. 23, these clusters are shown; B, C clusters and B',C' cluster are embedded in each monomers, and D cluster locates at the junction of the each monomers. Electron is transferred from C (C') cluster to D cluster via B' (B) cluster; thus, electron transfer from each active cluster involves both of the monomer. Distance between each Fe-S clusters are only 10 to 11 Å (fig.24), facilitating the electron transfer through these clusters. This appropriate location of the electron transporting components is another essential feature of enzymatic systems.

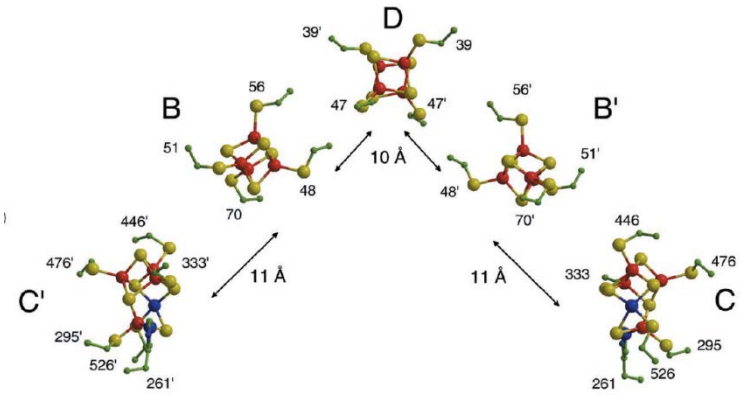

Fig.24 Distance between each electron transfer components in CODH. (Reprinted with permission from ref. 54. Copyright 2001, American Association for the Advancement of Science)

PSII in natural photosynthesis is one of the most sophisticated enzymatic systems in which several key components like light harvesting center, O_2 evolution center, proton transfer pathway, and electron transfer chains are highly organized. The components involved in electron transfer in PSII isolated from *Thermosynechococcus* are shown in fig.25. The initial event of the electron transfer in PSII is the light absorption by a light harvesting site composed of several chlorophyll *a* (Chl *a*) denoted as P680 located towards the lumenal surface. The excited electron is transferred

to Chl_{D1}, pheophytin ($Pheo_{d1}$), plastquinone Q_A, and finally to plastquinone Q_B [94]. The Q_B accepts two electrons and after protonation, it is released from PSII. On the other hand, generated $P680^+$ radical oxidizes the tyrosine (Tyr_z). Resulting Tyr^+ work as oxidant for OEC to promote water oxidation reaction.

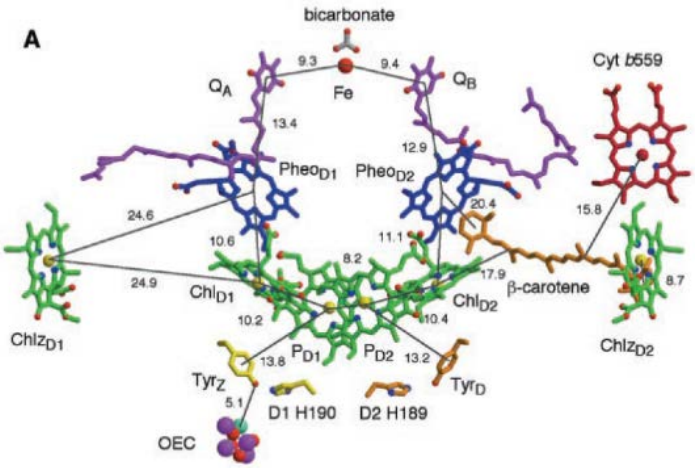

Fig.25 Components for electron transfer in PSII. (Reprinted with permission from ref. 94. Copyright 2004, American Association for the Advancement of Science)

Management of proton transfer ability is also crucial property of enzymatic systems to maintain the catalytic cycle. As expected from Nernst equation, the equilibrium potential for water oxidation reaction positively shifted with proton accumulation, resulting in the decrease of driving force for the reaction. Kocks et al. simulated the oscillations of ATP production of photosynthesis depending on the pH gradient across the thylakoid membrane (ΔpH)[121]. When ΔpH increases, the driving force for ATP production increases, resulting in the acceleration of ATP synthesis. The ATP synthesis decreasing ΔpH by consumption of proton, and thereby ΔpH is retained to a certain value. To achieve this ΔpH homeostasis, quick transportation of proton is necessary. As described in section 1.5.2, highly sophisticated hydrogen bonding network constructed by amino acid

residues and water molecules play a crucial role for the proton transportation and rather management of proton-coupled electron transfer in PSII [105, 108, 122-128]. Proton extracted from water is transferred to lumen side from D1-Asp 61 through polar channel (~30 Å) in D1 and PsbO unit. The relevant amino acid residues for proton channel possess the adequate pK_a values, namely, monotonical increase from OEC to lumen side, facilitating the proton transfer [123]. Promoted by the crystal structure reported by Umena et al., Nakamura et al. conducted Molecular dynamics (MD) simulation to clarify the dynamics of OEC [128]. The simulation detected three pathways for H_2O, proton, and O_2 transfer denoted as Path 1, Path 2, and Path 3. Path 1 and Path 2 are hydrogen-bonding networks from D1-Y161 to PsbV-K129 and from D1-D61 to CP47-A361, respectively (fig.26). Path 2 further branches to two pathways, marked Path 2-1 and Path 2-2. Path 3 mainly contains water molecules connecting from O_4 atom in OEC to PSbU-D96. Among these pathways, Path 2-1 is most efficient for proton transfer, while the other pathways (Path 1, Path 2-2 and Path 3) are suitable for the molecule transfer like H_2O, H_3O^+ and O_2.

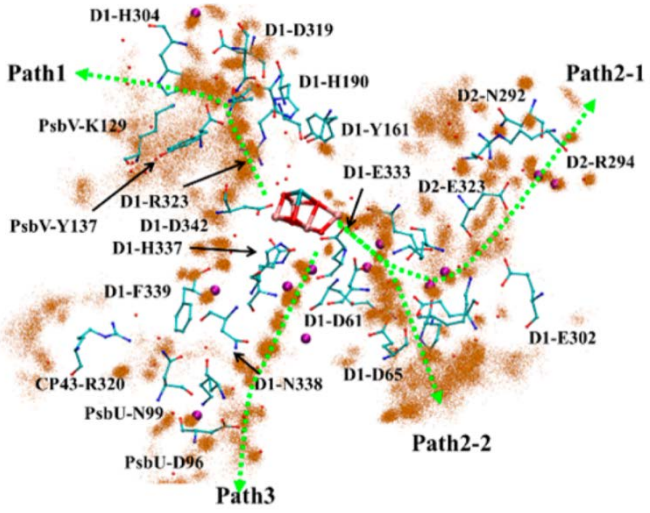

Fig.26 H_2O, proton, and O_2 transfer pathway for OEC based on MD simulation. (Reprinted with permission from ref. 128. Copyright 2013, American Chemical Society)

Not only for bioenzymatic systems, but for artificial catalytic systems, the efficient removal of protons without accumulation is one of the essential parameters to maintain the catalytic cycle. As described in section 1.5.3, Spiccia et al. achieved [114] the stable photo-anodic current from $[Mn_4O_4L_6]^+$ (L = (*p*-MeO-Ph)$_2$PO$_2$) embedded in a proton conducting membrane (Nafion) aiming at the efficient transportation of generated protons though the structure of the metal complex wasn't maintained the original one [116].

Based on the observations for the report by Spiccia et al. [114] and the taking the efficient and stable catalytic activity of enzymes into consideration, the development of reaction field achieving the optimum ordering of the reaction component, efficient transportation of reaction substrate, electrons and protons is also highly demanding to construct more sophisticated artificial multi-electron transfer catalysts, not only the design of reaction center.

References

[1] M. J. Russell, A. J. Hall, FROM GEOCHEMISTRY TO BIOCHEMISTRY Chemiosmotic coupling and transition element clusters in the onset of life and photosynthesis. *The Geochemical News*, **2002,** *113,* 6-12

[2] K. Sauer, V. K. Yachandra, A Possible evolutionary origin for the Mn_4 cluster of the photosynthetic water oxidation complex from natural MnO_2 precipitates in the early ocean. *Proc. Natl. Acad. Sci. USA*, **2002,** *99,* 8631-8636

[3] F. A. Armstrong, Why did Nature choose manganese to make oxygen? *Phil. Trans. R. Soc. B*, **2008,** *363,* 1263-1270

[4] G. C. Dismukes, V. V. Klimov, S. V. Baranov, Y. N. Kozlov, J. DasGupta, A. Tyryshkin, The origin of atmospheric oxygen on Earth: The innovation of oxygenic photosynthesis. *Proc. Natl. Acad. Sci. USA*, **2001,** *98,* 2170-2175

[5] M. J. Russell, The Alkaline Solution to the Emergence of Life: Energy, Entropy and Early Evolution. *Acta Biotheor.*, **2007,** *55,* 133-179

[6] T. Takashima, K. Hashimoto, R. Nakamura, Mechanisms of pH-Dependent Activity for Water Oxidation to Molecular Oxygen by MnO_2 Electrocatalysts. *J. Am. Chem. Soc.*, **2012,** *134,* 1519-1527

[7] W. P. Jencks, Requirements for General Acid-Base Catalysis of Complex Reactions. *J. Am. Chem. Soc.*, **1972,** *94,* 4731-4732

[8] T. Takashima, R. Nakamura, K. Hashimoto, Visible Light Sensitive Metal Oxide Nanocluster Photocatalysts: Photo-Induced Charge Transfer from Ce(III) to Keggin-Type Polyoxotungstates. *J. Phys. Chem. C*, **2009**, *113*, 17247-17253

[9] H. Tributsch, Multi-electron transfer catalysis for energy conversion based on abundant transition metals. *Electrochim. Acta*, **2007,** *52,* 2302-2316

[10] J. W. Peters, W. N. Lanzilotta, B. J. Lemon, L. C. Seefeldt, X-ray Crystal Structure of the Fe-Only Hydrogenase (Cpl) from *Clostridium pasteurianum* to 1.8 Angstrom Resolution. *Science,* **1998,** *282*, 1853-1858

[11] I. Daizadeh, D. M. Medvedev, A. A. Stuchebrukhov, Electron Transfer in Ferredoxin: Are Tunneling Pathways Evolutionarily Conserved? *Mol. Biol. Evol.,* **2002,** *19*, 406-415

[12] D. M. D'Alessandro, B. Smit, J. R. Long, Carbon Dioxide Capture: Prospects for New Materials. *Angew. Chem. Int. Ed.,* **2010,** *49*, 6058-6082

[13] M. Cokoja, C. Bruckmeier, B. Rieger, W. A. Herrmann, F. E. Kühn, Transformation of Carbon Dioxide with Homogeneous Transition-Metal Catalysts: A Molecular Solution to a Global Challenge? *Angew. Chem. Int. Ed.,* **2011,** *50*, 8510-8537

[14] R. J. Lim, M. Xie, M. A. Sk, J. –M. Lee, A. Fisher, X. Wang, K. H. Lim, A review on the electrochemical reduction of CO_2 in fuel cells, metal electrodes and molecular catalysts. *Catalysis Today,* **2014,** *233*, 169-180

[15] S. Das, W. M. A. W. Daud, Photocatalytic CO_2 transformation into fuel: A review on advances in photocatalyst and photoreactor. *Renewable and Sustainable Energy Reviews,* **2014,** *39*, 765-805

[16] M. E. Royer, (not available on the Internet) *Acad. Sci. Paris,* **1870,** *70*, 731-732

[17] Y. Hori, K. Kikuchi, S. Suzuki, PRODUCTION OF CO AND CH_4 IN ELECTROCHEMICAL REDUCTION OF CO_2 AT METAL ELECTRODES IN AQUEOUS HYDROGENCARBONATE SOLUTION. *Chem. Lett.,* **1985,** 1695-1698

[18] R. L. Cook, R. C. MacDuff, A. F. Sammells, On the Electrochemical Reduction of Carbon Dioxide at *In Situ* Electrodeposited Copper. *J. Electrochem. Soc.,* **1988,** *135*, 1320-1326

[19] M. Azuma, K. Hashimoto, M. Hiramoto, M. Watanabe, T. Sakata, Electrochemical Reduction of Carbon Dioxide on Various Metal Electrodes in Low-Temperature Aqueous

$KHCO_3$ Media. *J. Electrochem. Soc.,* **1990,** *137,* 1772-1778

[20] M. Watanabe, M. Shibata, A. Kato, M. Azuma, T. Sakata, Design of Alloy Electrocatalysts for CO_2 Reduction III. The Selective and Reversible Reduction of CO_2 on Cu Alloy Electrodes. *J. Electrochem. Soc.,* **1991,** *138,* 3382-3389

[21] A. Katoh, H. Uchida, M. Shibata, M. Watanabe, Design of Electrocatalyst for CO_2 Reduction V. Effect of the Microcrystalline Structure of Cu-Sn and Cu-Zn Alloys on the Electrocatalysis of CO_2 Reduction. *J. Electrochem. Soc.,* **1994,** *141,* 2054-2058

[22] Y. Hori, I. Takahashi, O. Koga, N. Hoshi, Selective Formation of C2 Compounds from Electrochemical Reduction of CO_2 at a Series of Copper Single Crystal Electrodes. *J. Phys. Chem. B,* **2002,** *106,* 15-17

[23] C. W. Li, M. W. Kanan, CO_2 Reduction at Low Overpotential on Cu Electrodes Resulting from the Reduction of Thick Cu_2O Films. *J. Am. Chem. Soc.,* **2012,** *134,* 7231-7234

[24] M. Gattrell, N. Gupta, A. Co, A review of the aqueous electrochemical reduction of CO_2 to hydrocarbons at copper. *J. Electroanal. Chem.,* **2006,** *594,* 1-19

[25] A. A. Peterson, F. Abild-Pedersen, F. Studt, J. Rossmeisl, J. K. Nørskov, How copper catalyzes the electroreduction of carbon dioxide into hydrocarbon fuels. *Energy Environ. Sci.,* **2010,** *3,* 1311-1315

[26] A. A. Peterson, J. K. Nørskov, Activity Descriptors for CO_2 Electroreduction to Methane on Transition-Metal Catalysts. *J. Phys. Chem. Lett.,* **2012,** *3,* 251-258

[27] Y. Chen, C. W. Li, M. W. Kanan, Aqueous CO_2 Reduction at Very Low Overpotential on Oxide-Derived Au Nanoparticles. *J. Am. Chem. Soc.,* **2012,** *134,* 19969-19972

[28] B. J. Fisher, R. Eisenberg, Electrocatalytic Reduction of Carbon Dioxide by Using Macrocycles of Nickel and Cobalt. *J. Am. Chem. Soc.,* **1980,** *102,* 7361-7363

[29] C. D. Windle, R. N. Perutz, Advances in molecular photocatalytic and electrocatalytic CO_2

reduction. *Coord. Chem. Rev.,* **2012,** *256*, 2562-2570

[30] M. Beley, J. –P. Collin, R. Ruppert, J. –P. Sauvage, Electrocatalytic Reduction of CO_2 by Ni Cyclam^{2+} in Water: Study of the Factors Affecting the Efficiency and the Selectivity of the Process. *J. Am. Chem. Soc.*, **1986,** *108*, 7461-7467

[31] J. –P. Collin, A. Jouaiti, J. –P. Sauvage, Electrocatalytic Properties of Ni(cyclam)$^{2+}$ and Ni_2(biscyclam)$^{4+}$ with Respect to CO_2 and H_2O Reduction. *Inorg. Chem.,* **1988,** *27*, 1986-1990

[32] M. Rudolph, S. Dautz, E. –G. Jäger, Macrocyclic [N_4^{2-}] Coordinated Nickel Complexes as Catalysts for the Formation of Oxalate by Electrochemical Reduction of Carbon Dioxide. *J. Am. Chem. Soc.*, **2000,** *122*, 10821-10830

[33] S. Sakaki, An ab Initio MO/SD-CI Study of Model Complexes of Intermediates in Electrochemical Reduction of CO_2 Catalyzed by $NiCl_2$(cyclam). *J. Am. Chem. Soc.*, **1992,** *114*, 2055-2062

[34] C. A. Kelly, Q. G. Mulazzani, M. Venturi, E. L. Blinn, M. A. J. Rodgers, The Thermodynamics and Kinetics of CO_2 and H^+ Binding to Ni(cyclam)$^+$ in Aqueous Solution. *J. Am. Chem. Soc.*, **1995,** *117*, 4911-4919

[35] J. Schneider, H. Jia, J. T. Muckerman, E. Fujita, Thermodynamics and kinetics of CO_2, CO, and H^+ binding to the metal centre of CO_2 reduction catalysts. *Chem. Soc. Rev.*, **2012,** *41*, 2036-2051

[36] M. Shibata, K. Yoshida, N. Furuya, Electrochemical synthesis of urea on reduction of carbon dioxide with nitrate and nitrite ions using Cu-loaded gas-diffusion electrode. *J. Electroanal. Chem.*, **1995,** *387*, 143-145

[37] M. Shibata, N. Furuya, Electrochemical synthesis of urea at gas-diffusion electrodes Part VI. Simultaneous reduction of carbon dioxide and nitrite ions with various

metallophthalocyanine catalysts. *J. Electroanal. Chem.,* **2001,** *507*, 177-184

[38] M. Shibata, N. Furuya, Simultaneous reduction of carbon dioxide and nitrate ions at gas-diffusion electrodes with various metallophthalocyanine catalysts. *Electrochim. Acta,* **2003,** *48*, 3953-3958

[39] Y. Oh, X. Hu, Organic molecules as mediators and catalysts for photocatalytic and electrocatalytic CO_2 reduction. *Chem. Soc. Rev.,* **2013,** *42*, 2253-2261

[40] G. Seshadri, C. Lin, A. B. Bocarsly, A new homogeneous electrocatalyst for the reduction of carbon dioxide to methanol at low overpotential. *J. Electroanal. Chem.,* **1994,** *372*, 145-150

[41] A. J. Morris, R. T. McGibbon, A. B. Bocarsly, Electrocatalytic Carbon Dioxide Activation: The Rate-Determining Step of Pyridinium-Catalyzed CO_2 Reduction. *ChemSusChem,* **2011,** *4*, 191-196

[42] J. A. Keith, E. A. Carter, Electrochemical reactivities of pyridinium in solution: consequences for CO_2 reduction mechanisms. *Chem. Sci.,* **2013,** *4*, 1490-1496

[43] B. A. Rosen, A. Salehi-Khojin, M. R. Thorson, W. Zhu, D. T. Whipple, P. J. A. Kenis, R. I. Masel, Ionic Liquid-Mediated Selective Conversion of CO_2 to CO at Low Overpotentials. *Science,* **2011,** *334*, 643-644

[44] B. A. Rosen, W. Zhu, G. Kaul, A. Salehi-Khojin, R. I. Masel, Water Enhancement of CO_2 Conversion on Silver in 1-Ethyl-3-Methylimidazolium Tetrafluoroborate. *J. Electrochem. Soc.,* **2013,** *160*, H138-H141

[45] J. D. Watkins, A. B. Bocarsly, Direct Reduction of Carbon Dioxide to Formate in High-Gas-Capacity Ionic Liquids at Post-Transition-Metal Electrodes. *ChemSusChem,* **2014,** *7*, 284-290

[46] L. Sun, G. K. Ramesha, P. V. Kamat, J. F. Brennecke, Switching the Reaction Course of Electrochemical CO_2 Reduction with Ionic Liquids. *Langmuir,* **2014,** *30*, 6302-6308

[47] D. C. Grills, Y. Matsubara, Y. Kuwahara, S. R. Golisz, D. A. Kurtz, B. A. Mello, Electrocatalytic CO_2 Reduction with a Homogeneous Catalyst in Ionic Liquid: High Catalytic Activity at Low Overpotential. *J. Phys. Chem. Lett.,* **2014,** *5,* 2033-2038

[48] D. Quezada, J. Honores, M. García, F. Armijo, M. Isaacs, Electrocatalytic reduction of carbon dioxide on a cobalt tetrakis(4-aminophenyl)porphyrin modified electrode in $BMImBF_4$. *New J. Chem.,* **2014,** *38,* 3606-3612

[49] F. Zhou, S. Liu, B. Yang, P. Wang, A. S. Alshammari, Y. Deng, Highly selective electrocatalytic reduction of carbon dioxide to carbon monoxide on silver electrode with aqueous ionic liquids. *Electrochem. Commun.,* **2014,** *46,* 103-106

[50] T. I. Doukov, T. M. Iverson, J. Seravalli, S. W. Ragsdale, C. L. Drennan, A Ni-Fe-Cu Center in a Bifunctional Carbon Monoxide Dehydrogenase/ Acetyl-CoA Synthase. *Science,* **2002,** *298,* 567-572

[51] O. Meyer, L. Gremer, R. Ferner, M. Ferner, H. Dobbek, M. Gnida, W. Meyer-Klaucke, R. Huber, The Role of Se, Mo and Fe in the Structure and Function of Carbon Monoxide Dehydrogenase. *Biol. Chem.,* **2000,** *381,* 865-876

[52] J. G. Ferry, CO DEHYDROGENASE. *Annu. Rev. Microbiol.,* **1995,** *49,* 305-333

[53] H. Dobbek, L. Gremer, O. Meyer, R. Huber, Crystal structure and mechanism of CO dehydrogenase, a molybdo iron-sulfur flavoprotein containing *S*-selanylcysteine. *Proc. Natl. Acad. Sci. USA,* **1999,** *96,* 8884-8889

[54] H. Dobbek, V. Svetlitchnyi, L. Gremer, R. Huber, O. Meyer, Crystal Structure of a Carbon Monoxide Dehydrogenase Reveals a [Ni-4Fe-5S] Cluster. *Science,* **2001,** *293,* 1281-1285

[55] C. Y. Ralston, H. Wang, S. W. Ragsdale, M. Kumar, N. J. Spangler, P. W. Ludden, W. Gu, R. M. Jones, D. S. Patil, S. P. Cramer, Characterization of Heterogeneous Nickel Sites in CO Dehydrogenases from *Clostridium thermoaceticum* and *Rhodospirillum rubrum* by Nickel

L-Edge X-ray Spectroscopy. *J. Am. Chem. Soc.,* **2000,** *122,* 10553-10560

[56] H. Wang, C. Y. Ralston, D. S. Patil, R. M. Jones, W. Gu, M. Verhagen, M. Adams, P. Ge, C. Riordan, C. A. Marganian, P. Mascharak, J. Kovacs, C. G. Miller, T. J. Collins, S. Brooker, P. D. Croucher, K. Wang, E. I. Stiefel, S. P. Cramer, Nickel L-Edge Soft X-ray Spectroscopy of Nickel-Iron Hydrogenases and Model Compounds-Evidence for High-Spin Nickel(II) in the Active Enzyme. *J. Am. Chem. Soc.,* **2000,** *122,* 10544-10552

[57] S. W. Ragsdale, M. Kumar, Nickel-Containing Carbon Monoxide Dehydrogenase/Acetyl-CoA Synthase. *Chem. Rev.,* **1996,** *96,* 2515-2539

[58] V. Svetlitchnyi, C. Peschel, G. Acker, O. Meyer, Two Membrane-Associated NiFeS-Carbon Monoxide Dehydrogenases from the Anaerobic Carbon-Monoxide-Utilizing Eubacterium *Carboxydothermus hydrogenoformans. J. Bacteriol.,* **2001,** *183,* 5134-5144

[59] B. Zhang, C. F. Hemann, R. Hille, Kinetics and Spectroscopic Studies of the Molybdenum-Copper CO Dehydrogenase from *Oligotropha carboxidovorans. J. Biol. Chem.,* **2010,** *285,* 12571-12578

[60] P. Amara, J. -M. Mouesca, A. Volbeda, J. C. Fontecilla-Camps, Carbon Monoxide Dehydrogenase Reaction Mechanism: A Likely Case of Abnormal CO_2 Insertion to a Ni-H^- Bond. *Inorg. Chem.,* **2011,** *50,* 1868-1878

[61] W. Shin, S. H. Lee, J. W. Shin, S. P. Lee, Y. Kim, Highly Selective Electrocatalytic Conversion of CO_2 to CO at -0.57 V (NHE) by Carbon Monoxide Dehydrogenase from *Moorella thermoacetica*. *J. Am. Chem. Soc.,* **2003,** *125,* 14688-14689

[62] A. Parkin, J. Seravalli, K. A. Vincent, S.W. Ragsdale, F. A. Armstrong, Rapid and Efficient Electrocatalytic CO_2/CO Interconversions by *CArboxydothermus hydrogenoformans* CO Dehydrogenase I on an Electrode. *J. Am. Chem. Soc.,* **2007,** *129,* 10328-10329

[63] T. W. Woolerton, S. Sheard, E. Reisner, E. Pierce, S. W. Ragsdale, F. A. Armstrong, Efficient

and Clean Photoreduction of CO_2 to CO by Enzyme-Modified TiO_2 Nanoparticles Using Visible Light. *J. Am. Chem. Soc.*, **2010,** *132*, 2132-2133

[64] M. Tezuka, T. Yajima, A. Tsuchiya, Y. Matsumoto, Y. Uchida, M. Hidai, Electroreduction of Carbon Dioxide Catalyzed by Iron-Sulfur Clusters $[Fe_4S_4(SR)_4]^{2-}$. *J. Am. Chem. Soc.*, **1982,** *104*, 6834-6836

[65] N. Komeda, H. Nagao, T. Matsui, G. Adachi, K. Tanaka, Electrochemical Carbon Dioxide Fixation to Thioesters Catalyzed by $[Mo_2Fe_6S_8(SEt)_9]^{3-}$. *J. Am. Chem. Soc.*, **1992,** *114*, 3625-3630

[66] K. Tanaka, R. Wakita, T. Tanaka, Electrochemical Carboxylation Coupled with Nitrite Reduction Catalyzed by $[Fe_4S_4(SPh)_4]^{2-}$ and $[Mo_2Fe_6S_8(SPh)_9]^{3-}$. *J. Am. Chem. Soc.*, **1989,** *111*, 2428-2433

[67] B. D. Yuhas, C. Prasittichai, J. T. Hupp, M. G. Kanatzidis, Enhanced Electrocatalytic Reduction of CO_2 with Ternary Ni-Fe_4S_4 and Co-Fe_4S_4-Based Biomimetic Chalcogels. *J. Am. Chem. Soc.*, **2011,** *133*, 15854-15857

[68] J. B. Varley, H. A. Hansen, N. L. Ammitzbøll, L. C. Grabow, A. A. Peterson, J. Rossmeisl, J. K. Nørskov, Ni-Fe-S Cubanes in CO_2 Reduction Electrocatalysis: A DFT Study. *ACS Catal.*, **2013,** *3*, 2640-2643

[69] A. –L. Reysenbach, E. Shock, Merging Genomes with Geochemistry in Hydrothermal Ecosystems. *Science*, **2002,** *296*, 1077-1082

[70] R. F. Weiss, P. Lonsdale, J. E. Lupton, A. E. Bainbridge, H. Craig, Hydrothermal plumes in the Galapagos Rift. *Nature*, **1977,** *267*, 600-603

[71] G. Wächtershäuser, Pyrite Formation, the First Energy Source for Life: a Hypothesis. *Syst. Appl. Microb.*, **1988,** *10*, 207-210

[72] G. Wächtershäuser, Evolution of the first metabolic cycles. *Proc. Natl. Acad. Sci. USA*, **1990,**

87, 200-204

[73] W. Heinen, A. M. Lauwers, Organic sulfur compounds resulting from the interaction of iron sulfide, hydrogen sulfide and carbon dioxide in an anaerobic aqueous environment. *Orig. Life Evol. Biosph.*, **1996,** *26*, 131-150

[74] C. Huber, G. Wächtershäuser, Activated Acetic Acid by Carbon Fixation on (Fe, Ni)S Under Primordial Conditions. *Science*, **1997,** *276*, 245-247

[75] C. Huber, G. Wächtershäuser, Peptides by Activation of Amino Acids with CO on (Ni,Fe)S Surfaces: Implications for the Origin of Life. *Science*, **1998,** *281*, 670-672

[76] M. J. Russell, R. M. Daniel, A. J. Hall, J. A. Sherringham, A Hydrothermally Precipitated Catalytic Iron Sulphide Membrane as a First Step Toward Life. *J. Mol. Evol.*, **1994,** *39*, 231-243

[77] W. Nitschke, S. E. McGlynn, E. J. Milner-White, M. J. Russell, On the antiquity of metalloenzymes and their substrates in bioenergetics. *Biochim. Biophys. Acta*, **2013,** *1827*, 871-881

[78] S. Trasatti, G. Buzzanca, Ruthenium dioxide: a new interesting electrode material. Solid state structure and electrochemical behavior. *J. Electroanal. Chem.*, **1971,** *29*, A1-A5

[79] A. Harriman, M. –C. Richoux, P. A. Christensen, S. Mosseri, P. Neta, Redox Reactions with Colloidal Metal Oxides Comparison of Radiation-generated and Chemically generated $RuO_2 \cdot 2H_2O$ and MnO_2 Colloids. *J. Chem. Soc., Faraday Trans.1*, **1987,** *83*, 3001-3014

[80] J. Kiwi, M. Grätzel, Colloidal Redox Catalysts for Evolution of Oxygen and for Light-Induced Evolution of Hydrogen from Water. *Angew. Chem. Int. Ed. Engl.*, **1979,** *18*, 624-626

[81] A. Harriman, I. J. Pickering, J. M. Thomas, P. A. Christensen, Metal Oxides as Heterogeneous Catalysts for Oxygen Evolution under Photochemical Conditions. *J. Chem.*

Soc., Faraday Trans. 1, **1988,** *84*, 2795-2806

[82] A. Mills, T. Russell, Comparative Study of New and Established Heterogeneous Oxygen Catalysts. *J. Chem. Soc. Faraday Trans.*, **1991,** *87*, 1245-1250

[83] M. Yagi, E. Tomita, S. Sakita, T. Kuwabara, K. Nagai, Self-Assembly of Active IrO_2 Colloid Catalyst on an ITO Electrode for Efficient Electrochemical Water Oxidation. *J. Phys. Chem. B*, **2005,** *109*, 21489-21491

[84] T. Nakagawa, N. S. Bjorge, R. W. Murray, Electrogenerated IrO_x Nanoparticles as Dissolved Redox Catalysts for Water Oxidation. *J. Am. Chem. Soc.*, **2009,** *131*, 15578-15579

[85] T. Nakagawa, C. A. Beasley, R. W. Murray, Efficient Electro-Oxidation of Water near Its Reversible Potential by a Mesoporous IrO_x Nanoparticle Film. *J. Phys. Chem. C*, **2009,** *113*, 12958-12961

[86] B. S. Brunschwig, M. H. Chou, C. Creutz, P. Ghosh, N. Sutin, Mechanism of Water Oxidation to Oxygen: Cobalt(IV) as an Intermediate in the Aquocobalt(II)-Catalyzed Reaction. *J. Am. Chem. Soc.*, **1983,** *105*, 4832-4833

[87] M. W. Kanan, D. G. Nocera, In Situ Formation of an Oxygen-Evolving Catalyst in Neutral Water Containing Phosphate and Co^{2+}. *Science*, **2008,** *321*, 1072-1075

[88] A. J. Esswein, M. J. McMurdo, P. N. Ross, A. T. Bell, T. D. Tilley, Size-Dependent Activity of Co_3O_4 Nanoparticle Anodes for Alkaline Water Electrolysis. *J. Phys. Chem. C*, **2009,** *113*, 15068-15072

[89] P. Rüetschi, P. Delahay, Influence of Electrode Material on Oxygen Overvoltage: A Theoretical Analysis. *J. Chem. Phys.*, **1955,** *23*, 556-560

[90] C. Iwakura, M. Nashioka, H. Tamura, Anodic Evolution of Oxygen on Solid Solutions with Spinel-type Structure. *NIHONKAGAKUKAISHI*, **1982,** *8*, 1294-1298

[91] J. O. Bockris, T. Otagawa, The Electrocatalysis of Oxygen Evolution on Perovskites. *J.*

Electrochem. Soc., **1984,** *131,* 290-302

[92] J. Suntivich, K. J. May, H. A. Gasteiger, J. B. Goodenough, Y. Shao-Horn, A Perovskite Oxide Optimized for Oxygen Evolution Catalysis from Molecular Orbital Principles. *Science,* **2011,** *334,* 1383-1385

[93] S. Raabe, D. Mierwaldt, J. Ciston, M. Uijttewaal, H. Stein, J. Hoffmann, Y. Zhu, P. Blöchl, C. Jooss, In Situ Electrochemical Electron Microscopy Study of Oxygen Evolution Activity of Doped Manganite Perovskites. *Adv. Funct. Mater.,* **2012,** *22,* 3378-3388

[94] K. N. Ferreira, T. M. Iverson, K. Maghlaoui, J. Barber, S. Iwata, Architecture of the Photosynthetic Oxygen-Evolving Center. *Science,* **2004,** *303,* 1831-1838

[95] T. M. Bricker, J. L. Roose, R. D. Fagerlund, L. K. Frankel, J. J. Eaton-Rye, The extrinsic proteins of Photosystem II. *Biochim. Biophys. Acta,* **2012,** *1817,* 121-142

[96] R. D. Fagerlund, J. J. Eaton-Rye, The lipoproteins of cyanobacterial photosystem II. *J. Photochem. Photobiol. B Biol.,* **2011,** *104,* 191-203

[97] B. Kok, B. Forbush, M. Mcgloin, COOPERATION OF CHARGES IN PHOTOSYNTHETIC O_2 EVOLUTION-I. A LINEAR FOUR STEP MECHANISM. *Photochem. Photobiol.,* **1970,** *11*, 457-475

[98] K. Sauer, J. Yano, V. K. Yachandra, X-ray spectroscopy of the photosynthetic oxygen-evolving complex. *Coord. Chem. Rev.,* **2008,** *252,* 318-335

[99] J. Yano, V. K. Yachandra, Oxidation state changes of the Mn_4Ca cluster in Photosystem II. *Photosynth. Res.,* **2007,** *92,* 289-303

[100] J. Yano, V. Yachandra, Mn_4Ca Cluster in Photosynthesis: Where and How Water is Oxidized to Dioxygen. *Chem. Rev.,* **2014,** *114,* 4175-4205

[101] E. M. Sproviero, J. A. Gascon, J. P. McEvoy, G. W. brudvig, V. S. Batista, Quantum Mechanics/Molecular Mechanics Study of the Catalytic Cycle of Water Splitting in

Photosystem II. *J. Am. Chem. Soc.,* **2008,** *130,* 3428-3442

[102] H. Schiller, H. Dau, Preparation protocols for high-activity Photosystem II membrane particles of green algae and higher plants, pH dependence of oxygen evolution and comparison of the S_2-state multiline signal by X-band EPR spectroscopy. *J. Photochem. Photobiol. B: Biol.,* **2000,** *55,* 138-144

[103] F. Rappaport, M. Guergova-Kuras, P. J. Nixon, B. A. Diner, J. Lavergne, Kinetics and Pathways of Charge Recombination in Photosystem II. *Biochemistry,* **2002,** *41,* 8518-8527

[104] M. Grabolle, H. Dau, Energetics of primary and secondary electron transfer in Photosystem II membrane particles of spinach revisited on basis of recombination-fluorescence measurements. *Biochim. Biophys. Acta,* **2005,** *1708,* 209-218

[105] H. Dau, I. Zaharieva, Principles, Efficiency, and Blueprint Character of Solar-Energy Conversion in Photosynthetic Water Oxidation. *Acc. Chem. Res.,* **2009,** *42,* 1861-1870

[106] A. Zouni, H. –T. Witt, J. Kern, P. Fromme, N. Krauβ, W. Saenger, P. Orth, Crystal structure of photosystem II from *Synechococcus elongates* at 3.8 Å resolution. *Nature,* **2001,** *409,* 739-743

[107] A. Guskov, J. Kern, A. Gabdulkhakov, M. Broser, A. Zouni, W. Saenger, Cyanobacterial photosystem II at 2.9-Å resolution and the role of quinones, lipids, channels and chloride. *Nature Struct. Mol. Biol.,* **2009,** *16,* 334-342

[108] Y. Umena, K. Kawakami, J. –R. Shen, N. Kamiya, Crystal structure of oxygen-evolving photosystem II at a resolution of 1.9 Å. *Nature,* **2011,** *473,* 55-61

[109] M. Suga, F. Akita, K. Hirata, G. Ueno, H. Murakami, Y. Nakajima, T. Shimizu, K. Yamashita, M. Yamamoto, H. Ago, J. –R. Shen, Native structure of photosystem II at 1.95 Å resolution viewed by femtosecond X-ray pulses. *Nature,* **2015,** *517,* 99-103

[110] S. Mukhopadhyay, S. K. Mandal, S. Bhaduri, W. H. Armstrong, Manganese Clusters

with Relevance to Photosystem II. *Chem. Rev.,* **2004,** *104,* 3981-4026

[111] W. F. Ruettinger, C. Campana, G. C. Dismukes, Synthesis and Characterization of $Mn_4O_4L_6$ Complexes with Cubane-like Core Structure: A New Class of Models of the Active Site of the Photosynthetic Water Oxidase. *J. Am. Chem. Soc.,* **1997,** *119,* 6670-6671

[112] A. Mishra, J. Yano, Y. Pushkar, V. K. Yachandra, K. A. Abboud, G. Christou, Heteronuclear Mn-Ca/Sr complexes, and Ca/Sr EXAFS spectral comparisons with the Oxygen-Evolving Complex of Photosystem II. *Chem. Commun.,* **2007,** 1538-1540

[113] G. C. Dismukes, R. Brimblecombe, G. A. N. Felton, R. S. Pryadun, J. E. Sheats, L. Spiccia, G. F. Swiegers, Development of Bioinspired Mn_4O_4-Cubane Water Oxidation Catalysts: Lessons from Photosynthesis. *Acc. Chem. Res.,* **2009,** *42,* 1935-1943

[114] R. Brimblecombe, D. R. J. Kolling, A. M. Bond, G. C. Dismukes, G. F. Swiegers, L. Spiccia, Sustained Water Oxidation by $[Mn_4O_4]^{7+}$ Core Complexes Inspired by Oxygenic Photosynthesis. *Inorg. Chem.,* **2009,** *48,* 7269-7279

[115] J. S. Kanady, E. Y. Tsui, M. W. Day, T. Agapie, A Synthetic Model of the Mn_3Ca Subsite of the Oxygen-Evolving Complex in Photosystem II. *Science,* **2011,** *333,* 733-736

[116] R. K. Hocking, R. Brimblecombe, L. –Y. Chang, A. Singh, M. H. Cheah, C. Glover, W. H. Casey, L. Spiccia, Water-oxidation catalysis by manganese in a geochemical-like cycle. *Nat. Chem.,* **2011,** *3,* 461-466

[117] G. F. Swiegers, J. K. Clegg, R. Stranger, Structural Similarities in enzymatic, homogeneous and heterogeneous catalysts of water oxidation. *Chem. Sci.,* **2011,** *2,* 2254-2262

[118] M. M. Najafpour, T. Ehrenberg, M. Wiechen, P. Kurz, Calcium Manganese (III) Oxides ($CaMn_2O_4 \cdot xH_2O$) as Biomimetic Oxygen-Evolving Catalysts. *Angew. Chem. Int. Ed.,* **2010,** *49,* 2233-2237

[119] I. Zaharieva, M. M. Najafpour, M. Wiechen, M. Haumann, P. Kurz, H. Dau, Synthetic manganese-calcium oxides mimic the water-oxidizing complex of photosynthesis functionally and structurally. *Energy Environ. Sci.,* **2011,** *4,* 2400-2408

[120] D. M. Robinson, Y. B. Go, M. Greenblatt, G. C. Dismukes, Water Oxidation by λ-MnO_2: Catalysis by the Cubical Mn_4O_4 Subcluster Obtained by Delithiation of Spinel $LiMn_2O_4$. *J. Am. Chem. Soc.,* **2010,** *132,* 11467-11469

[121] P. Kocks, J. Ross, Kinetic Model for (Damped) Oscillations of Transthylakoid pH in Plants. *J. Phys. Chem.,* **1995,** *99,* 16490-16497

[122] G. Renger, Coupling of electron and proton transfer in oxidative water cleavage in photosynthesis. *Biochim. Biophys. Acta,* **2004,** *1655*, 195-204

[123] H. Ishikita, W. Saenger, B. Loll, J. Biesiadka, E. –W. Knapp, Energetics of a Possible Proton Exit Pathway for Water Oxidation in Photosystem II. *Biochemistry,* **2006,** *45,* 2063-2071

[124] G. Renger, Oxidative photosynthetic water splitting: energetics, kinetics and mechanism. *Photosynth. Res.,* **2007,** *92,* 407-425

[125] T. J. Meyer, M. H. V. Huynh, H. H. Thorp, The Possible Role of Proton-Coupled Electron Transfer (PCET) in Water Oxidation by Photosystem II. *Angew. Chem. Int. Ed.,* **2007,** *46,* 5284-5304

[126] D. R. Weinberg, C. J. Gagliardi, J. F. Hull, C. F. Murphy, C. A. Kent, B. C. Westlake, A. Paul, D. H. Ess, D. G. McCafferty, T. J. Meyer, Proton-Coupled Electron Transfer. *Chem. Rev.,* **2012,** *112,* 4016-4093

[127] K. Saito, A. W. Rutherford, H. Ishikita, Mechanism of tyrosine D oxidation in Photosystem II. *Proc. Natl. Acad. Sci. USA,* **2013,** *110,* 7690-7695

[128] K. Ogata, T. Yuki, M. Hatakeyama, W. Uchida, S. Nakamura, All-Atom Molecular

Dynamics Simulation of Photosystem II Embedded in Thylakoid Membrane. *J. Am. Chem. Soc.*, **2013,** *135,* 15670-15673

Chapter 2.

The activation of metal sulfides as CO_2 reduction catalysts under the similar environment to primordial ocean

2.1. Introduction

In the last two decades, there has been considerable interest in understanding biogeochemical processes associated with deep-sea hydrothermal environments [1-8]. Such studies are motivated by the unique microbial and chemical processes occurring in the present and ancient deep oceans without energy input from sun light and using reductive chemicals such as H_2S and H_2 emitted from hydrothermal vents as energy sources [1,3,6,8]. In such environments, iron sulfides (FeSs), which are able to catalyze CO_2 reduction and carbon assimilation, are continuously precipitated [9]. Based on these phenomena, it has been proposed that the surface of FeS minerals, which often contains trace metals such as Ni, Cu, W and Mo [10], has played a critical role in prebiotic organic synthesis and early evolution of energy metabolisms in ancient Earth [10-27].

As a model of prebiotic organic synthesis, Russell et al. [28-31] have proposed that Ni-containing greigite (Fe_5NiS_8) embedded in a colloidal membrane of FeS acts as a catalyst for CO_2 reduction. This proposed model is based on the structural similarity of Fe_5NiS_8 to the $NiFe_3S_4$ cluster that functions as the reaction center of carbon monoxide dehydrogenase (CODH), a Ni-containing enzyme found in certain chemolithoautotrophic microorganisms including acetogens and methanogens that reversibly catalyzes the reduction of CO_2 to CO [32-34]. Russell et al. [18,35,36] have pointed that H_2 supplied from alkaline hydrothermal fluids serves as an electron and proton source for the conversion of CO_2 to formate by Fe_5NiS_8. In contrast, Wächtershäuser

et al. [37] suggested that FeS, rather than H_2, act as a reductant and demonstrated that Ni-containing FeS particles catalyzed the synthesis of organic compounds using the reducing power of the FeS/FeS_2 couple. As a potential prebiotic pathway of such H_2-independent acetyl-CoA synthesis, the hydrothermal synthesis (100 °C) of acetate from CO and CH_3SH in a mixed solution of FeS and NiS has also been demonstrated [12].

In biological systems, CO_2 reduction by CODH is coupled with the oxidation of H_2 to protons [38-40]. Recently, it has been also shown that CODH directly exchanges electrons with conductive substrates and functions as an efficient electrocatalyst for CO_2 reduction to CO at potentials near the thermodynamic potential of the CO_2/CO couple (−0.54 V vs SHE at pH 7.3) [41]. This finding, together with the hypothesis by Russell et al. [28-31] that Ni/greigite could be the evolutionary origin for the $NiFe_3S_4$ cluster in CODH, led us further to consider Ni/FeS system, especially greigite, is the promising candidate to construct multi-electron CO_2 reduction catalyst, as is observed for the immobilized catalytic center of CODH. The catalysis of greigite for CO_2 reduction, however, has never been examined.

To obtain new insight into the electrocatalysis of FeS precipitates, here, the electroreduction of CO_2 by hydrothermally synthesized Fe_3S_4 greigite was evaluated in an aqueous solution at pH 5.5 in order to mimic the pH of the CO_2-saturated early ocean [42]. Specifically, the author investigated the role of Ni in the electroactivation of CO_2 by replacing an Fe atom in greigite with a hetero-metal atom, such as Ni, Cu, or Zn.

In addition to the catalytic functionalization of iron sulfides, this work also attempted to provide insight into the homeostatic prebiotic organic fixation which is essential for the emergence of life. The two proposed pathways for prebiotic organic synthesis are based on the heterogeneous reactions of CO_2 with reductive chemicals such as H_2, H_2S, and FeS at the surface of Ni-containing FeS deposits. In any of the operative CO_2 reduction processes, however, the

formation of organic molecules is ceased when the reducing chemicals are consumed. Therefore, a continuous influx of reductants to the catalytic centers via diffusion and/or convection is essential to drive the prebiotic organic synthesis system. Alternatively, it is also possible to promote a continuous energy influx by the transfer of electrons from the densely interconnected structure of micron- and submicron-crystalline particles of FeS deposits (Fig. 1). Recently, Nakamura et al. examined the electrochemical functionalities of biogeochemical processes associated with FeS and found that a portion of mineral assemblage obtained from a black smoker chimney in the Mariner hydrothermal field of the Lau Basin displayed excellent metallic electrical conduction over a 10-cm distance [43,44]. In addition, the chimney minerals functioned as efficient electrocatalysts for the oxidation of H_2S and H_2, and the reduction of O_2 and ferric ions. Based on these findings, Nakamura et al. hypothesized that in addition to the reductive chemicals emitted from the hydrothermal fluids, high-energy electrons are also transported from the high-temperature hydrothermal fluid to the outer mineral interface with seawater via the hydrothermal sulfide deposits in the form of electrical current (Fig. 1). The FeS precipitates can also store, transport and discharge elemental hydrogen in the form of protons, as demonstrated from the use of FeS as an anode material in nickel-metal hydride batteries [45,46]. Therefore, it is possible that the natural setting of electrochemical reactors in the hydrothermal vents could sustain the energy flow for organic synthesis at the mineral interfaces between seawater and hydrothermal fluid.

One missing consideration concerning the prebiotic organic synthesis is the kinetic issues. The proposed reactions to promote organic synthesis is based on the thermodynamic considerations, namely, the reactions are assumed to proceed when only the thermodynamically favorable. To gain insight concerning the prebiotic organic synthetic event, the kinetics, i.e., overpotential for each reaction steps should be taken into consideration.

Based on the observed electroreduction potential of CO_2 and hydrogen storage ability of FeS

in this work, the author discuss how the natural electrochemical reactors in the hydrothermal vents would be able to trigger and maintain the electroreduction of CO_2 as the prebiotic organic carbon syntheses.

2.2. Experiments

2.2.1. Synthesis

Fe_3S_4 powder was prepared in aqueous solutions using standard hydrothermal techniques reported in the literature [46]. 6 mmol iron (II) sulfate heptahydrate (Sigma-Aldrich) and 6 mmol L-cysteine ($C_3H_7NO_2S$, Wako) were separately dissolved in 120 mL deionized water. The L-cysteine solution was dropped into iron (II) sulfate solution under stirring. Following further stirring for 20 min, the mixed solution was then combined in a Teflon-lined, 300-mL autoclave reaction vessel. After heating at 200 °C for 24 h, the reaction vessel was cooled to room temperature in air. Black precipitates were collected by filtration, and the obtained samples were washed with distilled water and ethanol, followed by evacuation for 2 h at 60 °C. The introduction of Ni^{2+}, Cu^{2+}, Zn^{2+} into iron sulfides was performed by the partial substitution of an appropriate ratio of iron (II) sulfate as a starting material with either nickel (II) sulfate hexahydrate (Wako), copper (II) sulfate pentahydrate (Wako) or zinc sulfate heptahydrate (Wako), respectively. Triethylamine (TEA) modification was conducted as follows. 20 mg of iron sulfide sample was dispersed into TEA (Wako) -containing distilled water with stirring. After 10 min, the dispersion was filtered, and washed with 50 ml of distilled water. Polyarylamine (PAH) modification was conducted by the mixing of iron sulfide sample and Poly(allylamine hydrochloride) (Sigma-Aldrich). 25 mg of iron sulfide sample was dispersed into the 600 μl of distilled water containing 4.8 mg of PAH. After the stirring for 10 min, the dispersion was subjected to the electrode preparation procedure. All chemicals were of the highest grade possible and were used without further purification.

2.2.2. Electrochemical Reactions

A gas diffusion electrode system was adapted to the electrochemical CO_2 reduction experiments. The electrochemical cell of this system consists of two compartments, one for the liquid phase

and one for the gas phase, and a gas diffusion electrode was positioned at the interface between these compartments. The gas diffusion electrode consisted of a hydrophobic gas diffusion layer facing the gas phase and a hydrophilic catalyst layer facing the liquid phase. To function as a working electrode, carbon paper (5.4 cm^2) was coated with the 25 mg of the prepared Fe_3S_4 powder and utilized for the catalytic layer. No binder materials were utilized in the coating of the electrode to avoid potential adverse effects on the catalytic ability of the metal sulfides. A Teflon membrane with 5-μm pore size (Millipore) was used as a gas diffusion layer. A Pt plate and Ag/AgCl (sat. KCl) electrode were used as counter and reference electrodes, respectively, and phosphate buffer (Na_2HPO_4/KH_2PO_4: pH = 5.5) was used as an electrolyte. Electrochemical measurements were conducted using a HSV-100 potentiostat (Hokuto-Denko). After potentiostatic condition for 30 min with 760 Torr CO_2 in a gas chamber, the analysis of reduction products was performed by gas chromatography (Shimadzu) equipped with FID or TCD detectors. All measurements were conducted at room temperature.

2.2.3. Characterization

Characterization of obtained samples was performed by X-ray diffraction (XRD) on a Rigaku-Smart Lab X-ray diffractometer using Cu Kα radiation (λ = 1.5418 Å) and an operation voltage and current maintained at 40 kV and 40 mA, respectively. FTIR spectra of samples and adsorbed species were recorded with a Vertex 70 FT-IR spectrometer (Bruker) in transmission mode at room temperature. The self-sustaining wafer of a sulfide sample (~10 mg) was mounted into an in-house constructed transmission infrared vacuum cell equipped with CaF_2 windows.

2.3. Results

2.3.1. Characterization

XRD patterns for Fe_3S_4 powder obtained from a mixed solution of L-cysteine and Fe(II) sulfate heptahydrate, and those for Ni-doped iron sulfide (Ni-FeS) with a Fe to Ni ratio of 5 to 1 are shown in Fig. 2a-i and Fig. 2a-ii, respectively. The prepared Fe_3S_4 powder exhibited an XRD pattern assigned to that of greigite (indexed to JCPDS 16-0713), characterized by a reverse spinel structure composed of edge-sharing FeS_6 octahedra and corner-sharing FeS_4 tetrahedra (Fig. 2b left). Although Ni-FeS with an Fe/Ni ratio of 5 retained the greigite structure, the sample with an Fe/Ni ratio of 1 exhibited a new phase assigned to $FeNi_2S_4$ (violarite, indexed to JCPDS 42-1449) and NiS (indexed to JCPDS 02-1280) (Fig. 2a-iii). $FeNi_2S_4$ has a reverse spinel structure composed of edge-sharing FeS_6 octahedra, NiS_6 octahedra, and corner-sharing NiS_4 tetrahedra [47] (Fig. 2b center). The sample obtained from mixed solutions of Ni(II) sulfate hexahydrate and L-cysteine (Fe/Ni = 0) had an XRD pattern characteristic of pure NiS (Fig. 2a-iv). SEM images of the Fe_3S_4 powder showed that the particles were composed of abundant nanosheets that formed an aggregated structure with a diameter of approx. 5 μm (Fig. 3a). In the sample prepared with a Fe/Ni ratio of 5, numerous spherical particles of ~500 nm in diameter were observed (Fig. 3b), which became more abundant as the amount of Ni increased (Fig. 3c and d).

2.3.2. Electrochemical reduction of protons

To investigate the electrocatalytic functions of the FeS deposits, carbon paper coated with greigite or Ni-FeS powder was used as a gas diffusion electrode. In order to avoid potential adverse effects on the catalytic ability of metal sulfides, no binder materials was utilized for coating of metal sulfides particles on a carbon paper. Although the lack of binder materials impedes the analysis of long-term electrocatalytic property due to a partial detachment of metal sulfides particles from

a carbon paper, it is of importance to evaluate the intrinsic catalytic properties of metal sulfides. A control experiment for electrochemical CO_2 reduction was first performed by examining the electrocatalysis of greigite at pH 5.5 in the presence of 760 Torr N_2. The potential-dependent Faradaic efficiencies (FE) for H_2 production by greigite are shown in Fig. 4. H_2 was generated at an onset potential of –0.5 V (vs SHE), which is 0.2 V below the theoretical equilibrium potential. The FE increased when more negative potential was applied and approached saturation at –1.1 V. The total FE fell below 100 % at a potential of –1.1 V and was reduced to almost 0 % at –0.5 V. The reduced FE was attributed to hydrogen storage within the greigite particles. A recent report showed that hydrothermally synthesized greigite powder stores hydrogen at a density of 3.26×10^{-2} mol/cm^3, which is comparable to that reported for Pd (6.83×10^{-2} mol/cm^3) [46]. The author estimated the amount of stored hydrogen in the greigite particles by monitoring the time course of potential under galvanostatic conditions at 60 mA g^{-1} after electrolysis at –0.5, –0.7 and –0.9 V for 30 min (Fig. 5). Under these three conditions, the amount of stored hydrogen was approximately $(3.86 \pm 2.02)\times10^{-3}$, $(3.95 \pm 0.51)\times10^{-3}$, and $(5.83 \pm 1.32)\times10^{-3}$ mol/cm^3, respectively, which corresponded to FEs of 80 ± 30 %, 61 ± 23 % and 19 ± 8 % (mean ± standard deviation), respectively. These values were consistent with the observed reductions in FE observed in the range –0.5 to –1.1 V.

2.3.3. Electrochemical reduction of CO_2

The electrocatalytic potential of FeS for CO_2 reduction was next evaluated by performing electrolysis with the greigite and Ni-FeS samples as catalysts in the presence of 760 Torr CO_2. After electrolysis at –1.3 V for 1 h, CO, CH_4, and H_2 were detected as gas phase products, and no products were detected by HPLC analysis in the liquid phase. As shown in Fig. 6a, the FEs of CO and CH_4 increased with increasing Ni content, with the sample prepared using a Fe/Ni ratio of 1

showing the highest activity. However, in the absence of FeS, CO and CH_4 were not produced. Thus, these results demonstrate that Ni-containing FeS has the ability to electrochemically reduce CO_2. As described in Fig. 2, the Ni-FeS (Fe/Ni = 1) sample is comprised of a mixture of $FeNi_2S_4$ and NiS. As pure NiS was less active than Ni-FeS (Fe/Ni = 1), $FeNi_2S_4$ appears to play a key role in CO_2 reduction processes.

The potential dependence of FEs for CO and CH_4 production for the greigite and Ni-FeS (Fe/Ni = 1) samples is presented in Fig. 7. Over the potential range examined, Ni doping led to an increase in FEs compared to those for greigite. For the Ni-FeS sample, CO and CH_4 were generated at onset potentials of –0.5 and –0.7 V, respectively, which are 0.07 and 0.54 V below the theoretical equilibrium potentials, respectively. Note that such improvement in FE was not observed for FeS that contained either Cu^{2+} or Zn^{2+} in place of Ni (Fig. 6b and c). From these results, it can be concluded that the tetrahedrally coordinated Ni ion center in $FeNi_2S_4$ plays an important role in the electrochemical reduction of CO_2 on the surface of FeS deposits.

2.3.4. Effects of FeS surface modification with amine compounds

The $NiFe_3S_4$ catalytic center in CODH is held in place by cysteine and histidine side chains of the protein [32]. It has been postulated in the iron sulfur world concept that the surface modification of metal sulfide minerals by peptides was an important evolutionary step from abiotic chemical reactions towards biotic metabolisms [48-50]. Specifically, the formation of Fe-N bonds through the interaction of peptide amine groups and FeS may have formed the primitive core of CODH. Alternatively, the peptide amine groups can also serve as co-catalysts for CO_2 reduction by donating electrons to the anti-bonding π^* orbital of CO_2, which is essential for the efficient electrochemical activation of CO_2, as it induces an anti-bonding character that facilitates disruption of the C=O bond, thereby decreasing the overpotential for CO_2 reduction. Recently,

density functional theory (DFT) calculations indicated that the overpotential for the electroreduction of CO_2 by the $NiFe_3S_4$ center in CODH is largely due to the requirement for energetic stabilization of the adsorbed COOH formed by the one-electron reduction of CO_2 [51,52]. N-containing ionic liquids have been demonstrated to efficiently stabilize adsorbed COO^- and thus lower the overpotential and increase the FE for CO production [49]. Therefore, the author speculate that the surface modification of FeS with amine compounds was critical for the evolutionary transition of inactive FeS minerals to active inorganic analogs of the $NiFe_3S_4$ center.

To examine the role of amine groups in the electrocatalytic reduction of CO_2, Ni-FeS powder (Fe/Ni = 1) was reacted with triethylamine (TEA) and poly-allylamine hydrochloride (PAH). Ni-FeS powder dispersed in an aqueous solution was reacted with different TEA concentrations and then examined by FT-IR following filtration, revealing that the reacted powder showed a symmetric vibration mode of ν(C-H) at 2853 and 2923 cm^{-1} (Fig. 8). These two infrared peaks remained at a similar intensity after vigorous washing of the powder sample with water, indicating that chemical bonds had formed between TEA and the Ni-doped FeS particles.

Using the TEA-treated Ni-FeS (Fe/Ni = 1) as an electrocatalyst, the effect of amine bases on electrochemical CO_2 reduction was examined at pH 5.5. Analysis of gas phase products after electrolysis for 30 min at –1.3 V revealed a large increase in the FEs of both CO and CH_4 production relative to those for untreated Ni-FeS (Fig. 9). The FEs for CO and CH_4 production increased with increasing TEA content. As neither CO nor CH_4 was detected when electrolysis was conducted in the absence of CO_2, CO_2, as opposed to TEA, was the carbon source for the production of CO and CH_4.

The enhancement of the FE was also observed during the reaction of PAH with the Ni-FeS catalysts. A PAH-modified Ni-containing FeS sample was prepared by the dispersion of Ni-FeS powder in an aqueous solution containing different concentrations of PAH. Surface modification

of Ni-FeS by PAH increased the FEs for CO and CH_4 by approx. 85 fold compared with unmodified greigite (Fig. 10). Taken together, these findings indicate that the co-existence of amine compounds with Ni-containing FeS minerals was critical for the formation of naturally occurring electrocatalysts capable of CO_2 reduction.

2.4. Discussion

The primary aim of the present research was to examine the electrocatalytic potential of FeS deposits for CO_2 reduction and obtain new insights into the metabolic evolution related to the utilization of reducing chemicals such as H_2 emitted from deep-sea hydrothermal vents for CO_2 reduction and carbon assimilation. The results demonstrate that hydrothermally synthesized iron-sulfide greigite is inefficient for the electrochemical reduction of CO_2 while the efficiency of this reaction is substantially improved (~85 fold) by Ni substitution of an Fe atom in greigite to form $FeNi_2S_4$, followed by the surface modification of $FeNi_2S_4$ with amine compounds such TEA and PAH. These findings highlight the possibility that abundant high-energy electrons delivered from hydrothermal fluids directly activate Ni/FeS deposits for CO_2 reduction.

Based on results of the electrocatalysis experiments performed in aqueous solution at pH 5.5, FeS precipitates containing $FeNi_2S_4$ as a catalytic site may function as an electrocatalyst for CO_2 reduction in hydrothermal environments (Fig. 11). Nakamura et al. proposed that the electrical current across a sulfide-rich chimney wall represented a new form of energy transport that sustains CO_2 reduction and carbon assimilation (Fig. 1) [43,44]. The essence of this model is that an interconnected percolation network of micron and submicron crystalline FeS particles facilitates the highly efficient conversion of a spatially discrete redox potential to electrical current. Accordingly, high-energy electrons present in the hot hydrothermal fluid are directly transported to the mineral outer interface with the cold ambient seawater. Notably, this model differs from those previously proposed that assume CO_2 and reductive chemicals directly react at a narrow mixing interface between the hydrothermal fluids and seawater. At temperatures above approximately 250 °C, organic carbons in contact with water become CO_2. As the electrosynthesis of organic compounds in the mineral outer interface may occur at much lower temperatures, the system can escape from rapid thermal degradation of synthesized organic compounds.

As shown in Figs. 7 and 11a, the electrochemical reduction of CO_2 to CO by FeS deposits containing $FeNi_2S_4$ was initiated at approximately −500 mV at pH 5.5. This potential is 180 mV more negative than the redox couple of H^+/H_2, which provides the most reducing power in a hydrothermal fluid, resulting in a strong endergonic electron transfer reaction (Fig. 11a). This energy imbalance suggests that a naturally occurring proton-motive force (PMF) as high as 200 mV, which is equivalent to a proton gradient of 3-4 pH units, must be established across the hydrothermal mineral structure such as chimney walls. The early ocean was saturated with CO_2 and had an estimated pH of 5.5 [41]. Thus, hydrothermal fluids with a pH above 8.5-9.5, such as alkaline bisulfide-bearing submarine vents described by Russell et al. [54], may utilize the spatially separated reductive energy of H_2 for electrosynthesis (Fig. 11b). Highly alkaline hydrothermal vents in the Hadean ocean are the most plausible system for prebiotic organic synthesis [55], as the hydrothermal vent chimney interior has a pH of 9-10 and the outer walls are bathed in ocean water with a pH of 5-6, generating a PMF of 180-300 mV.

It should be noted, however, that the PMF in alkaline vents would be rapidly dissipated by the H_2 generation reaction. As shown in Fig. 7, CO_2 reduction mediated by Ni/FeS competes for electrons with the proton reduction reaction that forms H_2. Thus, the low FE for CO_2 reduction limits electrosynthesis, as the H_2 generation inside the cavity of the densely-connected percolation structure of FeS rapidly decreases the proton concentration, dissipating the PMF (Fig. 11c, left). Therefore, the presence of amine bases, which substantially improve the FE for CO_2 reduction (Fig. 10), is critical for maintaining the proton gradient. Inorganic bases, such as Mg^{2+} and Ca^{2+}, are able to serve the same function as amine bases in the cavity of FeS.

The dissipation of the electrochemical gradient across the vent wall by H_2 generation may be minimized by chemical energy stored in the hydrothermal mineral precipitates. In the hydrothermal vents, in addition to electrons generated by H_2 oxidation, elemental hydrogen is

constantly generated at the interface between the hydrothermal fluid and the inner mineral precipitates via the dissociative insertion of H_2 and is subsequently stored within the mineral precipitates [45]. The storage of surplus energy is critical to maintain energy flow within the system, as described by Hengeveld et al [56]. FeS minerals can store, transport and discharge elemental hydrogen in the form of protons, as has been demonstrated from the use of FeS as anode materials in nickel-metal hydride batteries [45,46]. Therefore, the author hypothesize that elemental hydrogen stored in the hydrothermal mineral precipitates is used to lower the pH in the inner cavity by the reductive dissolution of HS^- from FeS_2 ($2H + FeS_2 \rightarrow FeS + HS^- + H^+$), when the electrochemical gradient within the reactors is dissipated as a result of H_2 (Fig. 11c, right). Such a homeostatic pH regulation mechanism is expected to balance the consumption of the electrochemical gradient by H_2 generation, and thus maintain the electrosynthesis of organic compounds at sulfide-rich hydrothermal deposits for long.

2.5. Conclusions

The present electrochemical experiments for CO_2 reduction by FeS attempted to functionalize the minerals as CO_2 reduction catalysts and at the same time, to elucidate the energetic basis for the electrosynthesis of organic compounds at bisulfide-bearing deep-sea hydrothermal vent deposits. The analyses demonstrated that FeS precipitates function as efficient electrocatalysts for CO_2 reduction upon the substitution of Fe with Ni to form $FeNi_2S_4$, and that the FE is further increased by modification of the catalytic surface with amine compounds. These findings are consistent with the concept that Ni/greigite serves as a prebiotic catalyst for CO_2 reduction due to its structural similarity with the catalytic centers of CODH enzyme [28-31]. However, the results indicate that surface modification of the active $FeNi_2S_4$ (violarite) center embedded in FeS precipitates with amine compounds was more important for the formation of naturally occurring electrocatalysts capable of the electroreduction of CO_2.

Based on the potential dependence of the CO_2 reduction products on iron sulfide samples, the author proposed the required pH gradient of 3-4 between hydrothermal fluid and sea water to promote the prebiotic carbon fixation. The requirement is satisfied in ancient alkaline hydrothermal vent whose interior pH was 9-10, as the pH of the ancient CO_2-saturated sea water was 5.5. The proposed requirement is an important model in terms of taking into consideration of the kinetic parameters. The author also demonstrated that H_2 generation competes with CO_2 reduction for electrical current, resulting in the consumption of the PMF. As amine compounds substantially improve the FE for CO_2 reduction, the author conclude that the presence of amine compounds or inorganic bases such as Mg^+ and Ca^{2+} is indispensable to limit dissipation of the electrochemical gradient by H_2 generation. Alternatively, homeostatic pH regulation mechanisms of FeS, as demonstrated from the use of sulfide-based anode materials in nickel-metal hydride batteries [45,46], may also limit the consumption of PMF by H_2 generation. Thus, the findings

are expected to provide great insights into not only the electron conduction and electrocatalytic functions of bisulfide-bearing hydrothermal vent deposits, but also the energy storage ability of the hydrothermal vent deposits, for triggering and maintaining the electrosynthesis of organic compounds prior to the emergence of the primordial living forms. The model can provide one of the answer for the reaction sustainability in prebiotic organic synthesis, which is not fully explained by the exisitng models.

References

[1] A. –L. Reysenbach, E. Shock, Merging Genomes with Geochemistry in Hydrothermal Ecosystems. *Science*, **2002,** *296*, 1077-1082

[2] K. Takai, K. Horikoshi, Genetic Diversity of Archaea in Deep-Sea Hydrothermal Vent Environments. *Genetics*, **1999,** *152*, 1285-1297

[3] W. Martin, J. Baross, D. Kelley, M. J. Russell, Hydrothermal vents and the origin of life. *Nat. Rev. Microbiol.*, **2008,** *6*, 805-814

[4] S. M. Sievert, C. Vetriani, Chemoautotrophy at Deep-Sea Vents: Past, Present, and Future. *Oceanography*, **2012,** *25*, 218-233

[5] T. Mogi, T. Ishii, K. Hashimoto, R. Nakamura, Low-voltage electrochemical CO_2 reduction by bacterial voltage-multiplier circuits. *Chem. Commun.*, **2013,** *49*, 3967-3969

[6] H. W. Jannasch, M. J. Mottl, Geomicrobiology of Deep-Sea Hydrothermal Vents. *Science*, **1985,** *229*, 717-725

[7] S. Nakagawa, K. Takai, Deep-sea vent chemoautotrophs: diversity, biochemistry and ecological significance. *FEMS Microbiol. Ecol.*, **2008,** *65*, 1-14

[8] J. A. Baross, S. E. Hoffman, SUBMARINE HYDROTHERMAL VENTS AND ASSOCIATED GRADIENT ENVIRONMENTS AS SITES FOR THE ORIGIN AND EVOLUTION OF LIFE. *Orig. Life Evol. Biosph.*, **1985,** *15*, 327-345

[9] G. Wächtershäuser, Pyrite Formation, the First Energy Source for Life: a Hypothesis. *Syst. Appl. Microb.*, **1988,** *10*, 207-210

[10] W. Nitschke, M. J. Russell, Hydrothermal Focusing of Chemical and Chemiosmotic Energy, Supported by Delivery of Catalytic Fe, Ni, Mo/W, Co, S and Se, Forced Life to Emerge. *J. Mol. Evol.*, **2009,** *69*, 481-496

[11] E. V. Koonin, W. Martin, On the origin of genomes and cells within inorganic compartments.

Trends Genet., **2005,** *21*, 647-654

[12] C. Huber, G. Wächtershäuser, Activated Acetic Acid by Carbon Fixation on (Fe, Ni)S Under Primordial Conditions. *Science*, **1997,** *276*, 245-247

[13] D. Rickard, G. W. Luther III, Chemistry of Iron Sulfides. *Chem. Rev.*, **2007,** *107*, 514-562

[14] M. Pósfai, R. E. Dunin-Borkowski, Sulfides in Biosystems. *Rev. Mineral. Geochem.*, **2006,** *61*, 679-714

[15] P. Baaske, F. M. Weinert, S. Duhr, K. H. Lemke, M. J. Russell, D. Braun, Extreme accumulation of nucleotides in simulated hydrothermal pore systems. *Proc. Natl. Acad. Sci. USA*, **2007,** *104*, 9346-9351

[16] M. A. A. Schoonen, Y. Xu, J. Bebie, ENERGETICS AND KINETICS OF THE PREBIOTIC SYNTHESIS OF SIMPLE ORGANIC ACIDS AND AMINO ACIDS WITH THE FES-H_2S/FES_2 REDOX COUPLE AS REDUCTANT. *Orig. Life Evol. Biosph.*, **1999,** *29*, 5-32

[17] T. M. McCollom, J. S. Seewald, Abiotic Synthesis of Organic Compounds in Deep-Sea Hydrothermal Environments. *Chem. Rev.*, **2007,** *107*, 382-401

[18] M. J. Russell, The Alkaline Solution to the Emergence of Life: Energy, Entropy and Early Evolution. *Acta Biotheor.*, **2007,** *55*, 133-179

[19] G. D. Cody, N. Z. Boctor, R. M. Hazen, J. A. Brandes, H. J. Morowitz, H. S. Yoder Jr, Geochemical roots of autotrophic carbon fixation: Hydrothermal experiments in the system citric acid, H_2O-(±FeS)-(±NiS). *Geochim. Cosmochim. Acta*, **2001,** *65*, 3557-3576

[20] N. Lane, W. F. Martin, The Origin of Membrane Bioenergetics. *Cell*, **2012,** *151*, 1406-1416

[21] O. Dannenmuller, K. Arakawa, T. Eguchi, K. Kakinuma, S. Blanc, A. M. Albrecht, M. Schmutz, Y. Nakatani, G. Ourisson, Membrane Properties of Archæal Macrocyclic Diether Phospholipids. *Chem. Eur. J.*, **2000,** *6*, 645-654

[22] M. G. Vladimirov, Y. F. Ryzhkov, V. A. Alekseev, V. A. Bogdanovskaya, V. A.

Otroshchenko, M. S. Kritsky, ELECTROCHEMICAL REDUCTION OF CARBON DIOXIDE ON PYRITE AS A PATHWAY FOR ABIOGENIC FORMATION OF ORGANIC MOLECULES. *Orig. Life Evol. Biosph.,* **2004,** *34*, 347-360

[23] U. J. Meierhenrich, J. -J. Filippi, C. Meinert, P. Vierling, J. P. Dworkin, On the Origin of Primitive Cells: From Nutrient Intake to Elongation of Encapsulated Nucleotides. *Angew. Chem. Int. Ed.,* **2010,** *49*, 3738-3750

[24] A. G. Cairns-Smith, A. J. Hall, M. J. Russell, MINERAL THEORIES OF THE ORIGIN OF LIFE AND AN IRON SULFIDE EXAMPLE. *Orig. Life Evol. Biosph.,* **1992,** *22*, 161-180

[25] G. D. Cody, TRANSITION METAL SULFIDES AND THE ORIGINS OF METABOLISM. *Annu. Rev. Earth Planet. Sci.,* **2004,** *32*, 569-599

[26] G. Wächtershäuser, From volcanic origins of chemoautotrophic life to Bacteria, Archaea and Eukarya. *Phil. Trans. R. Soc. B,* **2006,** *361*, 1787-1808

[27] F. L. Sousa, T. Thiergart, G. Landan, S. Nelson-Sathi, I. A. C. Pereira, J. F. Allen, N, Lane, W. F. Martin, Early bioenergetic evolution. *Phil. Trans. R. Soc. B,* **2013,** *368*, 20130088

[28] M. J. Russell, R. M. Daniel, A. J. Hall, J. A. Sherringham, A Hydrothermally Precipitated Catalytic Iron Sulphide Membrane as a First Step Toward Life. *J. Mol. Evol.,* **1994,** *39*, 231-243

[29] M. J. Russell, W. Martin, The rocky roots of the acetyl-CoA pathway. *Trends Biochem. Sci.,* **2004,** *29*, 358-363

[30] M. J. Russell, A. J. Hall, The emergence of life from iron monosulphide bubbles at a submarine hydrothermal redox and pH front. *J. Geol. Soc. Lond.,* **1997,** *154*, 377-402

[31] W. Nitschke, S. E. McGlynn, E. J. Milner-White, M. J. Russell, On the antiquity of metalloenzymes and their substrates in bioenergetics. *Biochim. Biophys. Acta,* **2013,** *1827*, 871-881

[32] H. Dobbek, V. Svetlitchnyi, L. Gremer, R. Huber, O. Meyer, Crystal Structure of a Carbon Monoxide Dehydrogenase Reveals a [Ni-4Fe-5S] Cluster. *Science*, **2001,** *293*, 1281-1285

[33] C. L. Drennan, J. Heo, M. D. Sintchak, E. Schreiter, P. W. Ludden, Life on carbon monoxide: X-ray structure of *Rhodospirillum rubrum* Ni-Fe-S carbon monoxide dehydrogenase. *Proc. Natl. Acad. Sci. USA*, **2001,** *98*, 11973-11978

[34] P. Amara, J. -M. Mouesca, A. Volbeda, J. C. Fontecilla-Camps, Carbon Monoxide Dehydrogenase Reaction Mechanism: A Likely Case of Abnormal CO_2 Insertion to a Ni−H^- Bond. *Inorg. Chem.*, **2011,** *50*, 1868-1878

[35] M. J. Russell, I. Kanik, Why Does Life Start, What Does It Do, Where Will It Be, And How Might We Find It? *Journal of Cosmology*, **2010,** *5*, 1008-1039

[36] M. J. Russell, A. J. Hall, W. Martin, Serpentinization as a source of energy at the origin of life. *Geobiology*, **2010,** *8*, 355-371

[37] G. Wächtershäuser, Evolution of the first metabolic cycles. *Proc. Natl. Acad. Sci. USA*, **1990,** *87*, 200-204

[38] J. G. Ferry, CO DEHYDROGENASE. *Annu. Rev. Microbiol.*, **1995,** *49*, 305-333

[39] S. W. Ragsdale, M. Kumar, Nickel-Containing Carbon Monoxide Dehydrogenase/Acetyl-CoA Synthase. *Chem. Rev.*, **1996,** *96*, 2515-2540

[40] W. B. Jeon, S. W. Singer, P. W. Ludden, L. M. Rubio, New insights into the mechanism of nickel insertion into carbon monoxide dehydrogenase: analysis of *Rhodospirillum rubrum* carbon monoxide dehydrogenase variants with substituted ligands to the [Fe_3S_4] portion of the active-site C-cluster. *J. Biol. Inorg. Chem.*, **2005,** *10*, 903-912

[41] W. Shin, S. H. Lee, J. W. Shin, S. P. Lee, Y. Kim, Highly Selective Electrocatalytic Conversion of CO_2 to CO at −0.57 V (NHE) by Carbon Monoxide Dehydrogenase from *Moorella thermoacetica. J. Am. Chem. Soc.*, **2003,** *125*, 14688-14689

[42] G. Macleod, C. Mckeown, A. J. Hall, M. J. Russell, HYDROTHERMAL AND OCEANIC pH CONDITIONS OF POSSIBLE RELEVANCE TO THE ORIGIN OF LIFE. *Orig. Life Evol. Biosph.,* **1994,** *24*, 19-41

[43] R. Nakamura, T. Takashima, S. Kato, K. Takai, M. Yamamoto, K. Hashimoto, Electrical Current Generation across a Black Smoker Chimney. *Angew. Chem. Int. Ed.,* **2010,** *49*, 7692-7694

[44] M. Yamamoto, R. Nakamura, K. Oguri, S. Kawagucci, K. Suzuki, K. Hashimoto, K. Takai, Generation of Electricity and Illumination by an Environmental Fuel Cell in Deep-Sea Hydrothermal Vents. *Angew. Chem. Int. Ed.,* **2013,** *52*, 10758-10761

[45] M. Bungs, H. Tributsch, Electrochemical and Photoelectrochemical Insertion and Transport of Hydrogen in Pyrite. *Ber. Bunsenges. Phys. Chem.,* **1997,** *101*, 1844-1850

[46] F. Cao, W. Hu, L. Zhou, W. Shi, S. Song, Y. Lei, S. Wang, H. Zhang, 3D Fe_3S_4 flower-like microspheres: high-yield synthesis *via* a biomolecule-assisted solution approach, their electrical, magnetic and electrochemical hydrogen storage properties. *Dalton Trans.,* **2009,** 9246-9252

[47] S. Haider, A. Roldan, N. H. de Leeuw, Catalytic Dissociation of Water on the (001), (011), and (111) Surfaces of Violarite, $FeNi_2S_4$: A DFT-D2 Study. *J. Phys. Chem. C,* **2014,** *118*, 1958-1967

[48] E. J. Milner-White, M. J. Russsell, SITES FOR PHOSPHATES AND IRON-SULFUR THIOLATES IN THE FIRST MEMBRANES: 3 TO 6 RESIDUE ANION-BINDING MOTIFS (NESTS). *Orig. Life Evol. Biosph.,* **2005,** *35*, 19-27

[49] R. P. H. Enriquez, T. N. Do, Interactions of iron-sulfur clusters with small peptides: Insights into early evolution. *Comput. Biol. Chem.,* **2012,** *41*, 58-61

[50] J. Meyer, Iron–sulfur protein folds, iron–sulfur chemistry, and evolution. *J. Biol. Inorg.*

Chem., **2008,** *13*, 157-170

[51] H. A. Hansen, J. B. Varley, A. A. Peterson, J. K. Nørskov, Understanding Trends in the Electrocatalytic Activity of Metals and Enzymes for CO_2 Reduction to CO. *J. Phys. Chem. Lett.*, **2013,** *4*, 388-392

[52] J. B. Varley, H. A. Hansen, N. L. Ammitzbøll, L. C. Grabow, A. A. Peterson, J. Rossimeisl, J. K. Nørskov, Ni-Fe-S Cubanes in CO_2 Reduction Electrocatalysis: A DFT Study. *ACS Catal.*, **2013,** *3*, 2640-2643

[53] B. A.Rosen, A. Salenhi-Khojin, M. R. Thorson, W. Zhu, D. T. Whipple, P. J. A. Kenis, R. I. Masel, Ionic Liquid–Mediated Selective Conversion of CO_2 to CO at Low Overpotentials. *Science*, **2011,** *334*, 643-644

[54] R. E. Mielke, K. J. Robinson, L. M. White, S. E. McGlynn, K. McEachern, R. Bhartia, I. Kanik, M. J. Russell, Iron-Sulfide-Bearing Chimneys as Potential Catalytic Energy Traps at Life's Emergence. *Astrobiology*, **2011,** *11*, 933-950

[55] T. Shibuya, T. Komiya, K. Nakamura, K. Takai, S. Maruyama, Highly alkaline, high-temperature hydrothermal fluids in the early Archean ocean. *Precambrian Res.*, **2010,** *182*, 230-238

[56] R. Hengeveld, M. A. Fedonkin, Bootstrapping the Energy Flow in the Beginning of Life. *Acta Biotheor.*, **2007,** *55*, 181-226

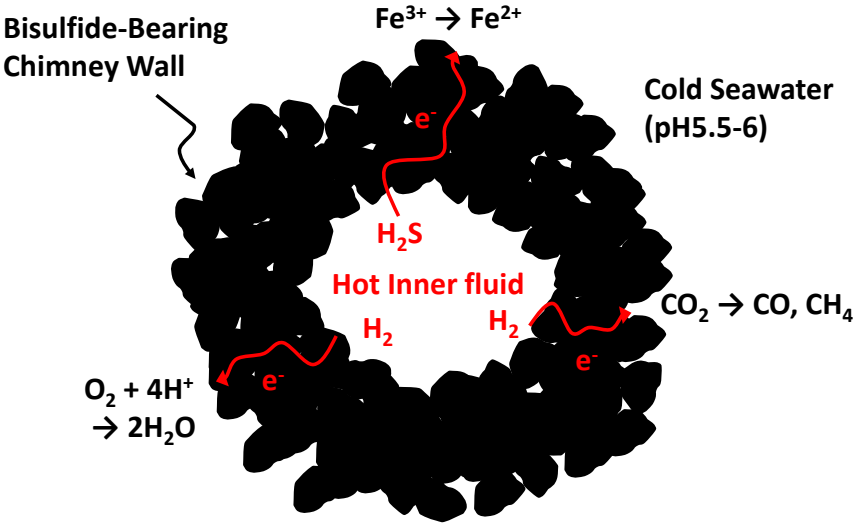

Fig. 1. Proposed model for electrical current generation in the deep-sea hydrothermal vent chimney [43,44]. In this model, electrons generated via the oxidation of H_2S and/or H_2 in the hydrothermal fluid are transported through the bisulfide-bearing chimney wall to seawater where they reduce Fe^{3+}, O_2, CO_2, and H^+. The charge balance between an inner and outer surface of a hydrothermal vent is maintained by the diffusion and/or convection of ionic substances in sea water and/or a hydrothermal fluid. Copyright 2014, Elsevier Ltd.

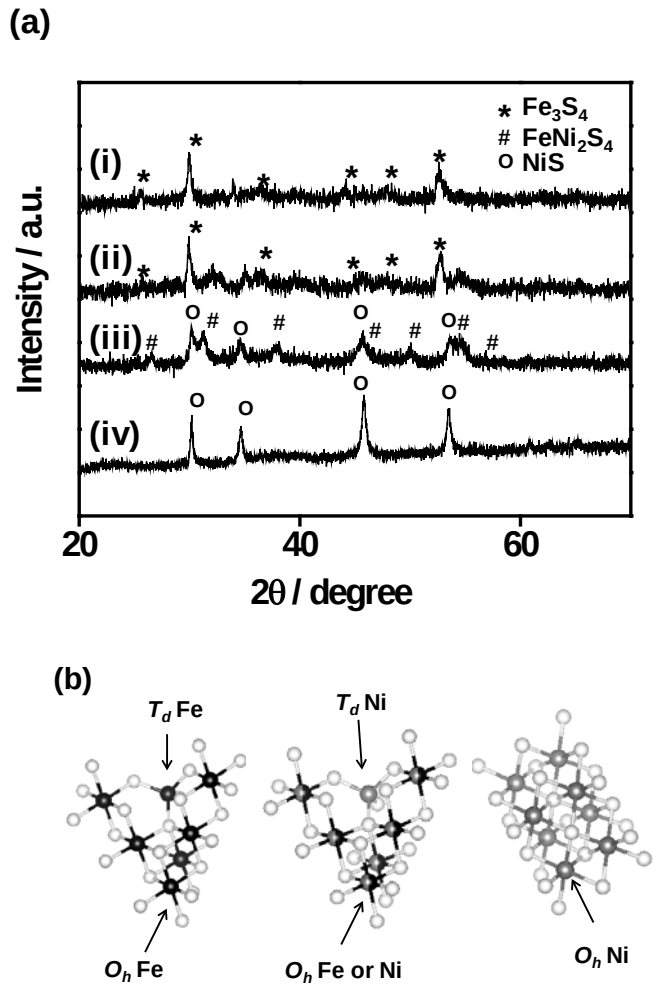

Fig. 2. (a) XRD patterns of (i) pristine greigite (Fe_3S_4), Ni-doped iron sulfides (Ni-FeSs) with ratios of Fe to Ni of (ii) 5 to 1 and (iii) 1 to 1, and (iv) NiS. The patterns assigned to greigite (Fe_3S_4), $FeNi_2S_4$ and NiS are indicated with asterisks, pound signs and open circles, respectively. (b) Ball and stick models for the crystal structures of (left) Fe_3S_4 (greigite), (center) $FeNi_2S_4$ and (right) NiS. White: S, black: Fe, and gray: Ni. Copyright 2014, Elsevier Ltd.

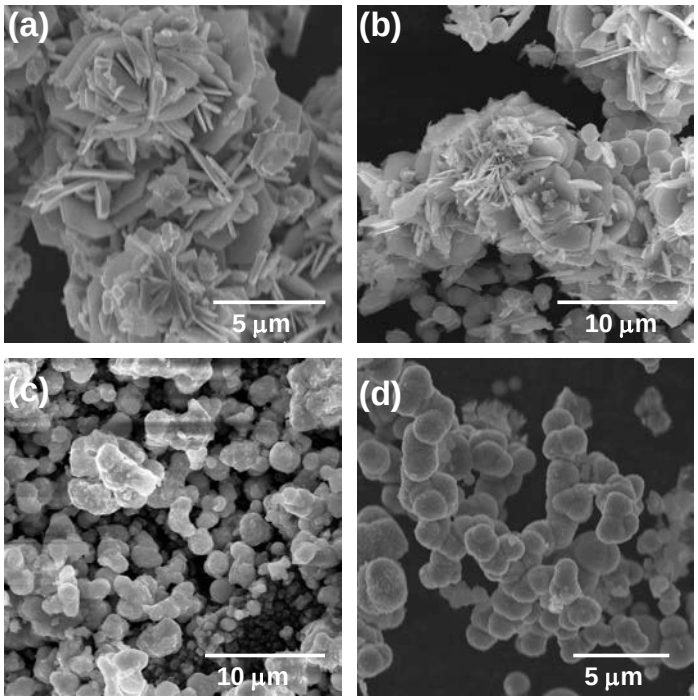

Fig. 3. SEM images for (a) pristine greigite, (b) Ni-doped iron sulfides (Ni-FeSs) with Fe to Ni ratios of 5 to 1 (c) and 1 to 1, and (d) NiS. Copyright 2014, Elsevier Ltd.

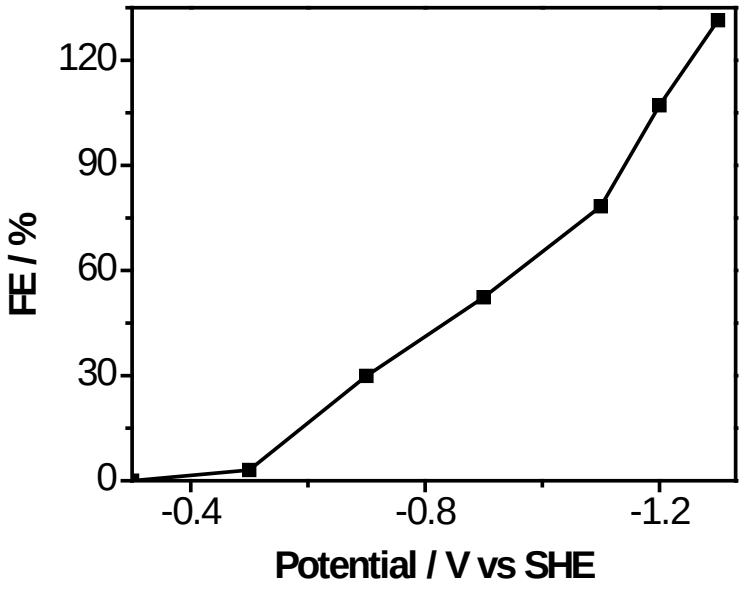

Fig. 4. Potential dependence of the FE (Faradaic efficiency) for hydrogen production from greigite after potentiostatic conditions in N_2 atmosphere. Copyright 2014, Elsevier Ltd.

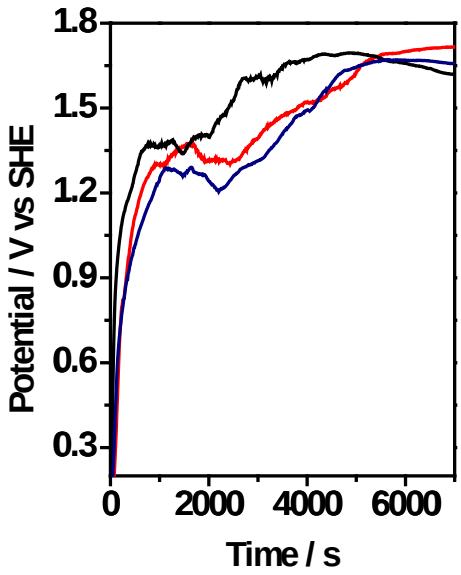

Fig. 5. The time course of potential under galvanostatic conditions at 500 μA for greigite sample after electrolysis at –0.5 (black), –0.7 (red) and –0.9 V (blue) for 30 min. The amount of stored hydrogen was estimated based on the methods reported by Cao et al [46]. The electrodes were discharged at a constant current of 60 mA g^{-1} after the electrolysis for 30 min with N_2 bubbling. The electrolyte was identical to that of the electrochemical CO_2 reduction experiments. The resting time between electrolysis and the discharge process was 5 min. At the galvanostatic condition, the potential-time curves showed plateau region at 1.3 V vs SHE and then increased to 1.6 V. The appearance of plateau region and the following gradual increase of potential is the characteristic behavior of oxidation of stored hydrogen. We adopted the time when the electrode potential reached to 1.4 V as the termination of the oxidation of hydrogen, and calculated the coulombic number to estimate accumulated hydrogen amount.

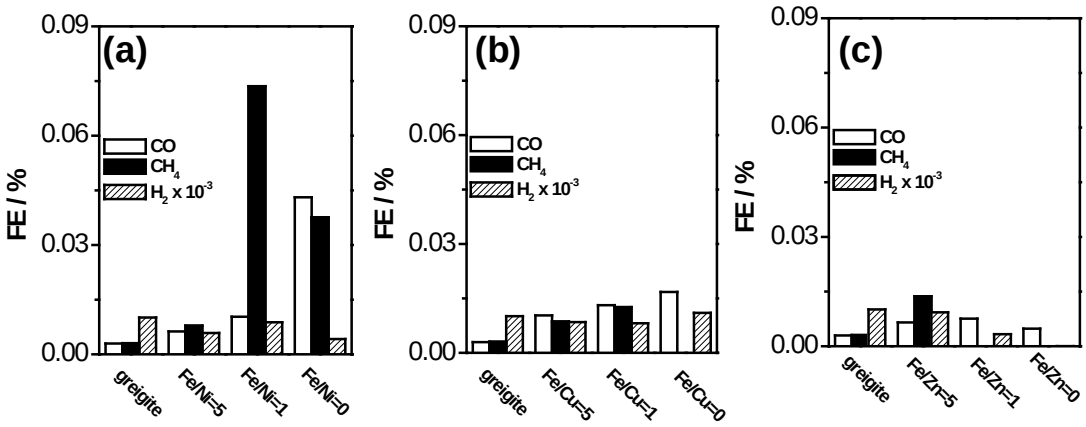

Fig. 6. Product distributions for (a) Ni-, (b) Cu- and (c) Zn-containing greigite with various Fe to metal ratios under a potentiostatic condition of –1.3 V vs SHE for 30 min. Copyright 2014, Elsevier Ltd.

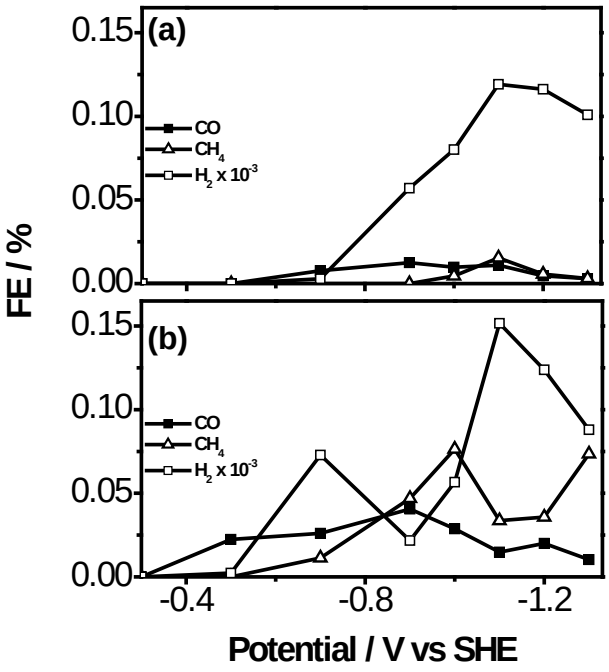

Fig. 7. Potential dependence of FE (Faradaic efficiency) for reaction products from (a) greigite and (b) Ni-containing greigite (Fe/Ni = 1) in the presence of 760 Torr CO_2. Filled squares, CO; open triangles, CH_4; open squares, $H_2 \times 10^{-3}$. Copyright 2014, Elsevier Ltd.

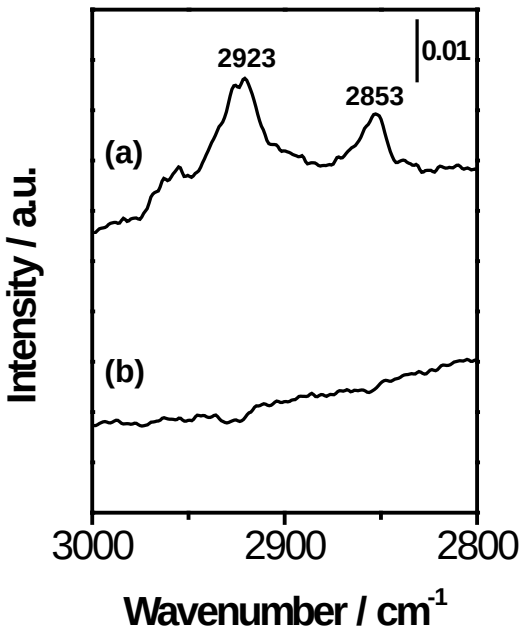

Fig. 8. FT-IR spectra of Ni-FeS (Fe/Ni = 1) after (a) and before (b) the reaction with TEA. The observed peaks at 2853 and 2923 cm^{-1} are assigned to the symmetric vibration mode of N(C-H). Copyright 2014, Elsevier Ltd.

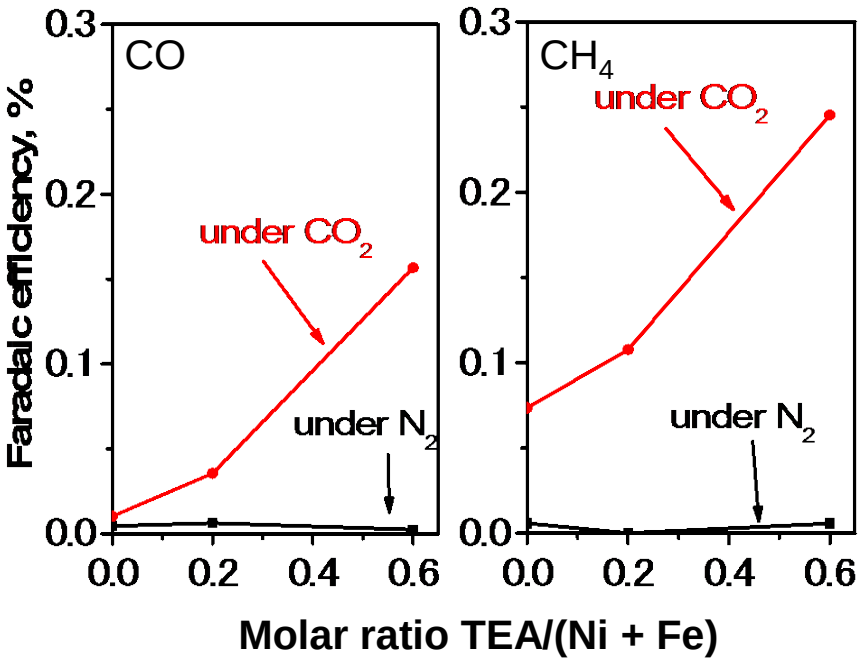

Fig. 9. FEs (Faradaic efficiencies) for CO (left) and CH_4 (right) production by Ni-containing greigite modified with various molar ration of TEA/(Ni + Fe) under a potentiostatic condition at – 1.3 V vs SHE for 30 min in the presence of 760 Torr of CO_2 (red curve) or N_2 (black curve).

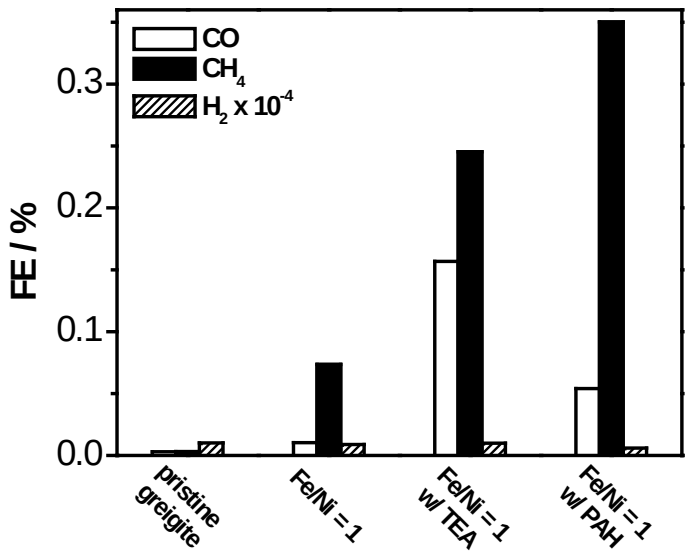

Fig. 10. FEs (Faradaic efficiencies) for CO, CH_4 and H_2 production by greigite, Ni-containing greigite (Fe/Ni = 1) and Ni-containing greigite (Fe/Ni = 1) modified with TEA or PAH under a potentiostatic condition at – 1.3 V vs SHE for 30 min. Copyright 2014, Elsevier Ltd.

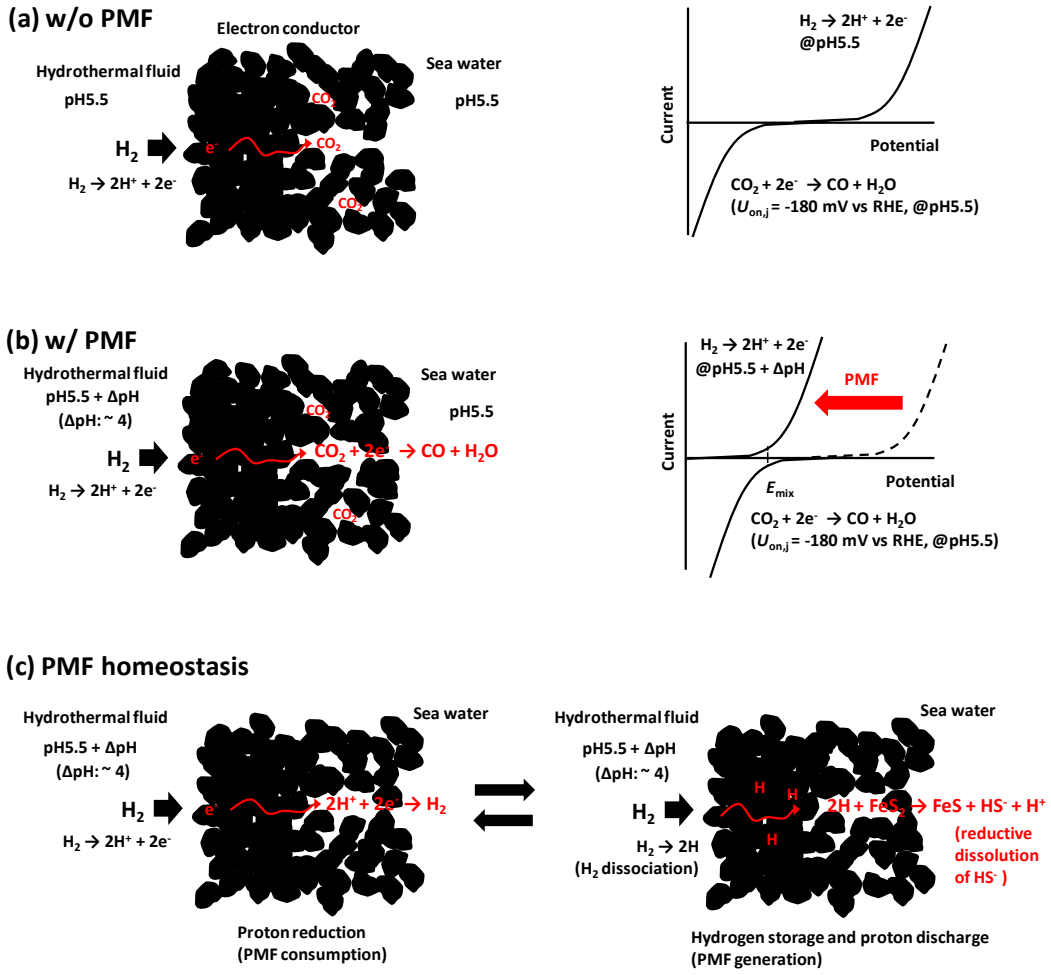

Fig. 11. Schematic illustration for the electrochemical synthesis of organic compounds in bisulfide-bearing deep-sea hydrothermal mineral deposits. (a) In the absence of the proton-motive force (PMF) across the mineral structure, electroreduction of CO_2 at the outer mineral interface by H_2 in hydrothermal fluid is the dominant endergonic reaction. (b) In the presence of the PMF, which can be as high as 200 mV, CO_2 reduction proceeds in the cavity of the bisulfide-bearing mineral deposits. (c-left) Due to the low FE for CO_2, the electrical current is predominantly used for H_2 generation, which lowers the proton concentration in the cavity, dissipating the electrochemical gradient. (c-right) Dissipation of the PMF by H_2 evolution leads to the release of elemental hydrogens stored in the hydrothermal mineral deposits into the cavity in the form of protons by the reductive dissolution of HS^- from FeS_2 ($2H + FeS_2 \rightarrow FeS + HS^- + H^+$), thereby

increasing the proton concentration and regenerating the PMF to initiate the electroreduction of CO_2. Copyright 2014, Elsevier Ltd.

Chapter 3.

Regulating Proton-Coupled Electron Transfer for Efficient Water Splitting by Mn Oxides at Neutral pH

3.1. Introduction

The development of efficient catalysts for the oxidation of water to molecular oxygen has long been the focus of intense research [1-12]. Such studies are motivated by the desire to understand the water splitting process in natural systems, such as photosystem II (PSII) of oxygenic photosynthesis, and artificial photosynthetic systems designed to produce hydrogen through proton reduction or convert carbon dioxide to fuels. In nature, water oxidation proceeds with extraordinarily high catalytic activity in PSII, in which a Ca-containing tetrameric manganese cluster ($CaMn_4O_5$) supported by bridged oxides or hydroxides and carboxylate and histidine side chains from the protein serves as the multi-electron oxidation catalyst [13-18]. Notably, all species capable of O_2 evolution possess a qualitatively identical reaction centers, and no metal element other than Mn has been identified in the catalytic cluster of PSII. Therefore, extensive research efforts have been aimed at developing water oxidation catalysts composed of the abundant element Mn [19-29].

However, a remarkable contradiction still exists on the catalytic performance between naturally occurring and synthetic Mn catalysts, particularly under neutral pH conditions. Although bioinspired water oxidation catalysts, particularly Mn oxides, function as effective electrocatalysts under alkaline conditions [30-32]; the activity of most Mn oxides is markedly reduced at neutral pH, resulting in a large electrochemical overpotential (η) ranging from 500 to 700 mV [32-35]. This high η contrasts that of the PSII tetrameric Mn cluster, which catalyzes

water oxidation with an η of only 160 mV [15-17]. Recently, Takashima et al. have shown the primary origin for these sharp declines of catalytic potential of MnO_2 under neutral conditions [35,36].

Measurements of *in-situ* water oxidation current and optical absorption have shown that electron injection from H_2O to anodically poised MnO_2 forms Mn^{3+}, which acts as a precursor for the O_2-evolution reaction [35,36]. Takashima et al. have also demonstrated that Mn^{3+} disproportionates to form Mn^{2+} and Mn^{4+} at pH <9, and subsequent regeneration via the electrooxidation of Mn^{2+} acts as the rate-determining step in the overall four-electron/four-proton reaction [35,36]. It is notable that the redox change of Mn from 2+ to 3+ on the surface of MnO_2 is approx. 1.4 V at pH <9, which forces the onset potential for water oxidation current ($U_{on,\,j}$) to remain constant at approx. 1.5 V irrespective of the pH. The involvement of the pH-independent step in the redox change of Mn increases η at intermediate pH, as shown in Fig. 1a, and is the primary origin for the sharp decline of catalytic potential of MnO_2 under neutral conditions. This property prohibits the successful application of Mn oxides as components of artificial photosynthetic systems.

The new mechanism has important implications for exploring efficient Mn-oxide catalysts for the oxidation of H_2O to O_2. It will also lead to new understanding for the marked difference in catalytic performance between naturally occurring and synthetic Mn catalysts at physiological pH. Namely, Mn^{3+} is free from CD during the Kok cycle of PSII, in contrast to synthetic Mn oxides. Thus, further clarification of the mechanism is very important. In this chapter, the author have investigated the effect of solution pH on the d-d transition of surface-associated Mn^{3+}, because the ligand field splitting of a Mn center is expected to depend strongly on solution pH owing to the occurrence of protonation or deprotonation in the water ligand bound to Mn^{3+}. As expected, the author observed a clear effect of solution pH on spectral features of Mn^{3+}.

The model explained above and the result of the pH-dependent spectral features of Mn^{3+} have suggested that the efficiency of Mn oxides as O_2-evolution catalysts may be enhanced by regulating proton-coupled electron transfer (PCET) in the electrooxidation step of Mn^{2+} to Mn^{3+}. PCET is a key part of the efficient energy conversion by PSII [37-40]. In particular, the concerted proton-electron transfer (CPET) pathway, which involves the transfer of protons and electrons in a single concerted step, avoids charge build-up and thereby enables the redox change of the tetrameric Mn cluster in PSII over a narrow potential range (approx. 250 mV) [13-15]. Therefore, it can be deduced that synthetic Mn oxides inefficiently catalyze water oxidation at neutral pH because they lack the inherent ability to manage both protons and electrons.

Herein, the author attempted to induce CPET on the surface of a Mn-oxide electrocatalyst and demonstrate that this rationale-based strategy substantially improved the O_2-evolution activity of synthetic Mn oxide in neutral medium.

3.2. Methods

3.2.1. *In situ* measurement of the pH-dependent spectral features of Mn^{3+}

3.2.1.1. Preparation of MnO_2 electrode

Manganese oxide (MnO_2) electrodes were prepared using a spray deposition method. A 0.5 mM MnO_2 colloidal solution, which was synthesized by the reduction of $KMnO_4$ with a stoichiometric amount of $Na_2S_2O_3$, was repeatedly sprayed onto a clean conducting glass substrate (FTO-coated glass, resistance: 20 Ω/sq) held on a hotplate at 200 °C. The resultant transparent darkbrown film on the electrode was thoroughly rinsed with pure water and then calcined at 500 °C in air for 2 h.

3.2.1.2. Electrospectroscopic measurement

Current density (j) vs. potential (U) curves were obtained with a commercial potentiostat and potential programmer (HZ-5000, Hokuto Denko) using a Pt wire as the counter electrode and a Ag/AgCl/KCl(sat.) electrode as the reference electrode, respectively. The electrolyte solution of a 0.5 M Na_2SO_4 aqueous solution was prepared using highly pure Milli-Q water and reagent-class chemicals, and the pH was adjusted using 0.1 M H_2SO_4, 1.0 M NaOH, and their mixture. A phosphate buffer solution was prepared from a mixture of 50 mM NaH_2PO_4 and 50 mM Na_2HPO_4.

Optical absorption spectra were measured in diffuse transmission (DT) mode using a UV-vis spectrometer (UV-2550, Shimadzu) equipped with a multipurpose large-sample compartment with a built-in integrating sphere (MPC-2200, Shimadzu). For *in situ* acquisition of spectra, a MnO_2 film electrode mounted in the electrochemical cell was placed in front of the integrating sphere to collect diffused transmission light.

3.2.2. Regulating Proton-Coupled Electron Transfer for Efficient Water Splitting

3.2.2.1. Synthesis procedure of α-MnO_2.

α-MnO_2 powder was prepared as previously described [41]. 1.10 g potassium permanganate ($KMnO_4$) was dissolved in 20 ml double-distilled water and the resulting mixture was stirred for 30 min at 60 °C. Separately, 1.55 g manganese (II) chloride tetrahydrate ($MnCl_2 \cdot 4H_2O$) was added to 25 ml of a 2 M acetic acid aqueous solution, which was then stirred for 20 min at room temperature. The $MnCl_2$ solution was added to the $KMnO_4$ solution, and the resulting mixture was stirred for 2 h at 80 °C. The formed particles were collected and washed several times with doubled-distilled water. The samples were dried overnight at 60 °C in air and then used for preparing electrodes. All chemical reagents were obtained from Wako and utilized without further purification.

3.2.2.2. Electrode preparation.

Particulate α-MnO_2 film electrodes were prepared using a spray deposition method, as previously described [35]. 75 mg of the prepared α-MnO_2 powder sample was suspended in 20 ml water by sonication at an amplitude of 15 W for 30 min with a homogenizer (S4000, Qsonica). The suspension was diluted to 100 ml with water and was then sprayed onto a clean conducting glass substrate (FTO-coated glass, resistance: 20 Ω/square, size: 30 mm × 30 mm; SPD Laboratory, Inc.) at 200 °C using an automatic spray gun (Lumina, ST-6). After coating, the electrodes were washed thoroughly with distilled water. The amount of deposited MnO_2 was approx. 0.14 mg/cm^2.

3.2.2.3. Electrochemical water oxidation.

Current density (j) vs potential (U) curves were obtained with a commercial potentiostat and potential programmer (HZ-5000, Hokuto Denko), using a Pt wire as the counter electrode and an

Ag/AgCl/KCl (sat.) electrode as the reference electrode. The electrolyte solution (0.5 M Na_2SO_4) was prepared using highly pure Milli-Q water (18 $M\Omega^{-1}cm^{-1}$) and reagent-grade chemicals, and the pH was adjusted using 0.1 M H_2SO_4 and 1.0 M NaOH [35]. No agent for pH buffering was added to the electrolyte solution to avoid influences from the specific adsorption of multivalent anions. The prepared electrolyte solution was bubbled with Ar gas prior to measurements and temperature of the reactor was kept at 30 °C unless otherwise noted. For minimizing pH changes near the electrode surface, the *j* vs *U* curve was measured using a potential sweep from negative to positive without stirring. The amount of dissolved oxygen in the electrolyte solution was monitored simultaneously during the *j* vs *U* measurements using a needle-type oxygen microsensor (Microx TX3-trace, PreSens). A gas chromatograph equipped with a TCD detector (GC-8A, Shimadzu) was used to monitor the amount of oxygen in the head-space of electrochemical reactors. The electrodeposition of MnO_2 catalysts on glassy carbon electrode for rotating disk electrode (RDE) measurement was conducted using electrolysis in 0.3 M $MnSO_4$ aq (pH = 1.8 adjusted by conc. H_2SO_4) at +1.35 V vs SHE for 300 s at room temperature [42]. RDE measurement was carried out using Rotating Disk Electrode Apparatus (RRDE-3A, Ver 1.2, ALS Co., Ltd) connected to with a commercial potentiostat and potential programmer (HZ-7000, Hokuto Denko) at room temperature. Pyridine and its derivatives were obtained from Wako and isotopic reagents (D_2O and D_2SO_4 for pD adjustment) were purchased from Sigma-Aldrich.

3.3. Results and discussions

3.3.1 *In situ* measurement of the pH-dependent spectral features of Mn^{3+}

In the previous studies [35,36], UV-vis spectroelectrochemical detection of the intermediate species for water oxidation with a Mn-oxide electrode was conducted in the absence of a pH buffering reagent. To examine if the specific adsorption of a pH buffering reagent affects the spectral feature of Mn^{3+}, UV-vis absorption spectra of a MnO_2 electrode were measured at 1.7 V with and without phosphate (50 mM), using spectral data obtained at 1.1 V as a reference (Fig. 2). In both cases, an absorption band appeared in the spectral region of the Mn^{3+} d-d transition, while a red-shift from 510 to 540 nm was observed in the presence of phosphate. Phosphate has a specific affinity to Mn oxides [43] and its coordination to Mn^{3+} is expected to cause a red-shift of the d-d transition absorption band due to its electron-withdrawing property [44]. Meanwhile, a blue-shift of the Mn^{3+} d-d transition from 510 to 470 nm was observed for Mn oxides following the coordination of electron-donating amine groups to Mn^{3+} (trace 3, Fig. 2). Therefore, the observed red-shift caused by the addition of phosphate indicates that phosphate not only functions as a pH buffer, but also alters the ligand field splitting of surface-associated Mn^{3+} species via specific coordination. To examine the effects of protonation or deprotonation in the water ligand bound to Mn^{3+}, UV-vis absorption spectra shown hereafter were taken in the absence of the pH buffering reagent.

Fig. 3 shows the UV-vis absorption spectra of surface associated Mn^{3+} species generated during water oxidation at pH 6, 10, and 13 under unbuffered conditions [45]. With increasing pH, the absorption peak shifted from 510 to 470 nm, which was accompanied by a decrease in the peak intensity. These observations demonstrate that the coordination environment of Mn^{3+} at neutral pH differs from that under alkaline conditions and suggest that the ligand field splitting of surface-associated Mn^{3+} species becomes larger at pH 13 than that at pH 6.

Regarding the origin of the observed pH-dependent coordination of Mn^{3+}, it is worth noting the new mechanism of water oxidation by MnO_2. As described in the introduction, Mn^{3+} is stable relative to CD at pH 13. Therefore, Mn^{3+} generated by electron injection from water to anodically poised MnO_2 may generate the absorption band at 470 nm. As the pK_{a2} [46] of a water ligand of Mn^{4+} is around 2.4 [47], the Mn^{3+} species exhibiting a 470-nm band at pH 13 is most likely to be Mn^{3+}-O^- (Fig. 4B). On the other hand, Mn^{3+} is unstable relative to CD under neutral conditions and its accumulation on MnO_2 surfaces requires the electrooxidation of Mn^{2+}. As the pK_a of a water ligand of Mn^{2+} is ~10.6 [48-50], the Mn^{3+} species detected at 510 nm at pH 6 is expected to be coordinated with either a H_2O or OH^- ligand generated via following reactions: Mn^{2+}- H_2O $\rightarrow$ Mn^{3+}-H_2O + e^-, or Mn^{2+}-H_2O $\rightarrow$ Mn^{3+}-OH + H^+ + e^-. According to the spectrochemical series, a magnitude of the ligand field strength increases in order of H_2O > O^{2-} > OH^- [51]. Thus, the blue-shift of the d-d transition at pH 13 relative to that at pH 6 indicates that Mn^{3+}-OH, not Mn^{3+}-H_2O, is the candidate for the species that provides the 510-nm absorption at pH 6 (Fig. 4A). The sharp decrease in the peak intensity at pH 13 relative to that at pH 6 might also be interpreted by the higher symmetry of the ligand field for Mn^{3+}-O^- than for Mn^{3+}-OH, as the five-coordination sites of a surface Mn^{3+} octahedra are occupied with framework O^{2-} ions. In the spectrum measured at pH 10, absorption bands appeared at 510 and 470 nm. The spectrum at pH 10 is a superimposition of the spectra observed at pH 6 and 13. As the transition point for the occurrence of CD and CC of Mn^{3+} is at around pH 9–10 [35,52], the spectrum at pH 10 indicates the coexistence of Mn^{3+}-O^- and Mn^{3+}-OH.

Water oxidation experiments in Fig. 3 were conducted under unbuffered conditions. Therefore, the mechanism for water oxidation is expected to vary from that for an alkaline solution to that for a neutral solution with the progress of water oxidation due to proton accumulation. Takashima et al. demonstrated that a water oxidation current sharply decreased upon scanning the electrode

potential in the positive direction at pH 12 in the absence of a pH buffer (Fig. 5A, solid line), while a continuous increase in current was attained with stirring (Fig. 5A, dotted line) [35,53]. This effect of stirring on the *j-U* curves is a clear indication that accumulation of protons altered the mechanism of water oxidation. In consistent with the *j-U* curve at pH 12, the author found that the UV-vis absorption spectra of the Mn^{3+} d-d transition at pH 12 also varied with the progress of water oxidation. As shown in Figs. 5B and 5C, upon sweeping the potential from 0.7 to 1.8 V without stirring, the ratio of the absorbance at 470 nm to that at 510 nm ($\Delta Abs_{470}/ \Delta Abs_{510}$) decreased from 1.3 to 0.8. Notably, the decrease in $\Delta Abs_{470}/\Delta Abs_{510}$ became prominent at U higher than 0.9 V, at which the water oxidation current began to be suppressed. On the other hand, in the case of stirring, $\Delta Abs_{470}/\Delta Abs_{510}$ remained constant at 1.3 (Fig. 5B, open squares). The agreement between the potential dependence of the water oxidation current and $\Delta Abs_{470}/ \Delta Abs_{510}$ in Fig. 5 demonstrates that the change in the reaction mechanism induced by proton accumulation is associated with the protonation states of a water ligand of the intermediate Mn^{3+} species (Fig. 4).

3.3.2. CPET induction by the addition of pyridine.

One possible way to induce CPET is the introduction of a protonation site, which has a pK_a value that is intermediate between the pK_a of Mn^{3+}-OH_2 (0.7) and Mn^{2+}-OH_2 (10.6) [48-50], as predicted by the libido rule of general acid-base catalysis [54-56], in close proximity to the water oxidation active site. In the course of oxidation from Mn^{2+} to Mn^{3+}, the pK_a of the Mn center undergoes a large change that would convert an unfavorable proton-transfer reaction to a favorable one with respect to the base [40, 48-50, 54-59]. Therefore, the regeneration of Mn^{3+} at neutral pH would be converted from a stepwise to a concerted pathway if the base accepts the proton at the PCET transition state rather than directly from Mn^{2+}-OH_2, as illustrated in Fig. 1b. In support of this

speculation, recent density functional theory (DFT) calculations have shown that the pK_a values of terminal water ligands in biomimetic oxomanganese complexes are drastically changed upon the oxidation of Mn^{2+} to Mn^{3+} [48,60]. In addition, the agreement of the pK_a value of Mn^{2+}-OH_2 with the transition point between pH 9-10 for the pH-independent and -dependent activity of the electrooxidation reaction [35] (Fig. 1a) also provides the support for this hypothesis. Namely, at a pH greater than the pK_a of Mn^{2+}-OH_2, the electrooxidation of Mn^{2+} proceeds after the water ligand bound to Mn^{2+} deprotonates to form Mn^{2+}- OH^- (path c in Fig. 1b), whereas Mn^{2+} oxidation prior to deprotonation produces the unstable intermediate Mn^{3+}-OH_2 (path a in Fig. 1b), leading to the electrooxidation of Mn^{2+}-OH_2, which is more thermodynamically unfavorable.

To examine the validity of the hypothesis, the effects of pyridine on the electrocatalytic performance of Mn oxides for water oxidation and its influence on the pH dependence of $U_{on,\,j}$ were first investigated. Pyridine has a pK_a (5.25) that is intermediate between that of Mn^{3+}-OH_2 (0.7) and Mn^{2+}-OH_2 (10.6), and exists as a deprotonated form at neutral pH. Thus, pyridine satisfies the conditions of the libido rule [54]. The current density (j) vs potential (U) curves for a synthesized MnO_2 electrocatalyst, consisting of α-MnO_2 nanoparticles deposited onto a fluorine-doped tin oxide (FTO) electrode, measured electrochemical cells operated at neutral pH with and without pyridine are shown in Fig. 1. The amount of dissolved O_2 in the electrolyte was also monitored using a needle-type oxygen microsensor. The author observed a large increase in both anodic current (Fig. 6a) and O_2 production (Fig. 6b) for the MnO_2 electrode in the presence of pyridine. The effects of pyridine were more prominent at higher concentrations, with an approx. 200-mV negative shift in $U_{on,\,j}$ being observed at 0.5 M pyridine. Analysis of the head-space gas in the electrochemical cell containing 50 mM pyridine by gas chromatography (GC) revealed that a turnover number (evolved O_2 molecules per total Mn atoms deposited on the FTO electrode) of 17 and coulombic efficiency (CE) of 78% was reached after 90 min of electrolysis at 1.7 V,

confirming that the evolved O_2 was generated from water oxidation. When electrolysis was conducted for 90 min at 1.39 V in the presence of pyridine (2.5 mM), 86 nmol of CO_2 was detected. This amount corresponds to the 4% of a coulombic efficiency if we assume the complete oxidation of pyridine to CO_2 (Fig. 7 and 8).

The author next examined the pH dependence of $U_{on,j}$ for water oxidation current to confirm whether CPET was induced on the surface of a Mn-oxide electrocatalyst as predicted. The electrode potential at which the current density reached 130 μA cm^{-2} was adopted as $U_{on,j}$. In the absence of pyridine, no pH dependence of $U_{on,j}$ was observed at pH <10 (Fig. 9a), whereas $U_{on,j}$ showed a clear pH dependence following the addition of pyridine into the electrochemical cell (Fig. 9b). Plots of $U_{on,j}$ against electrolyte pH showed a pH dependence in the presence of pyridine (Fig. 9c and d), demonstrating that proton transfer was involved in the rate-determining transition state for water oxidation. Notably, pyridine did not enhance water oxidation activity at pHs higher than the pK_a of Mn^{2+}-OH_2 (Fig. 9d), a result that is consistent with the deprotonation of the water ligand bound to Mn^{2+} forming Mn^{2+}-OH^- at pH >10 (path c in Fig. 1b). Similarly, when pyridine was added to the electrolyte at pH 4, almost no activity enhancement was observed, as 95% of pyridine exists as the protonated form at this pH and therefore cannot function as a proton acceptor.

The results presented in Fig. 6 and Fig. 9 are consistent with the hypothesis that pyridine accepts a proton from the water ligand bound to Mn during the PCET transition state. However, when the *j*–*U* measurements were conducted in D_2O instead of H_2O in the presence of 50 mM pyridine at neutral pD (pD = pH + 0.4) [61], the kinetic isotope effect (KIE) measured at 1.37 V for $j(H_2O)$ and $j(D_2O)$ was 1.62, which is only slightly higher than the KIE obtained in the absence of pyridine (KIE = 1.48). These results suggest that pyridine acts as proton acceptor in this system; however, the basicity of pyridine was not strong enough to induce the fully concerted reaction path. In other words, the author consider that the electron-transfer reaction is more rapid than the

transfer of the proton from the Mn-bound water ligand to pyridine and speculate that there are more suitable bases for the enhancement of catalytic activity.

3.3.3. Regulation of PCET mechanisms by the addition of bases with different pK_a values.

In an attempt to accelerate the proton-transfer reaction, the author replaced pyridine with a base that has a higher pK_a value. As pK_a is the index for proton-accepting ability, the addition of a base with a higher pK_a was expected to promote the deprotonation of water ligand during the PCET transition state. Several pyridine derivatives, namely 3-methylpyridine (β-picoline, pK_a = 5.80), 4-methylpyridine (γ-picoline, 6.10), 2,6-dimethylpyridine (2,6-lutidine, 6.96), and 2,4,6-trimethylpyridine (γ-collidine, 7.48) were evaluated as candidate bases. Similar to pyridine, the pK_a values of the selected derivatives are lower than that of Mn^{2+}-OH_2, meaning that the direct deprotonation of water ligands (path c in Fig. 1) is thermodynamically unfavorable.

The j–U curves for the MnO_2 electrode in the presence of pyridine derivatives at pH 7.5 are shown in Fig. 10a. As expected, a higher catalytic activity was observed with increasing pK_a of the added base. The η decreased with the increase of pK_a; for example, an approx. 70-mV negative shift of $U_{on,j}$ was observed for γ-collidine relative to that for pyridine. To compensate for the concentration difference between the protonated and deprotonated forms of bases due to pK_a differences, the electrolyte was prepared using a 25 mM concentration of the deprotonated base form. Therefore, the shift of $U_{on,j}$ that can be seen in Fig. 10a is attributable to the different proton-accepting abilities of the pyridine derivatives. GC analysis of the head-space gas revealed that the CE for O_2 evolution was 77% (γ-collidine), 62% (2,6-lutidine), 66% (γ-picoline), and 57% (β-picoline), and that the amount of evolved O_2 exceeded unity for all examined bases. Notably, the rate of O_2 production increased monotonically with increasing of pK_a, as shown in Fig. 10b, a

result that is consistent with the observed trends in the *j*–*U* curve measurements. In the case of γ-collidine, the O_2-evolution activity of the MnO_2 electrode at pH 7.5 showed an approx. 15-fold enhancement compared to that observed in the absence of bases, reaching nearly half of the O_2-evolution activity that was measured in alkaline medium (Fig. 11).

The KIE values obtained from *j*–*U* curve measurements for the MnO_2 electrode at neutral pH (and adjusted pD = pH + 0.4) [61] were plotted as a function of base pK_a (Fig. 12a). The concentration of the deprotonated form of bases was adjusted to 25 mM. It can be seen that the KIEs increased monotonically from 1.6 to 2.7 as the base pK_a increased from 5.25 to 7.48. The KIE is a rough measure of the position of the transition state along the reaction coordinate for proton transfer [62]. Large KIEs are expected for a reaction with nearly symmetrical transition states, as the activated complex has the proton almost equally shared between the reactant and product. Meanwhile, smaller effects are observed as the transition state moves toward reactant, as very little deprotonation has occurred at transition state. Therefore, the increase of KIEs with the base pK_a demonstrates that bases with a stronger proton extracting property increase the extent of deprotonation of the water ligand bound to a Mn center at the rate-determining transition state. Moreover, the pH dependence of $U_{on,j}$ at pH <9 became more prominent with increasing pK_a of the base (Fig. 12b and Fig. 13). For example, the shift per pH unit increased from approx. 25 mV for pyridine to 60 mV for γ-collidine (Fig. 14). The latter value indicates that the η for water oxidation reaction is almost constant irrespective of a solution pH higher than pK_a of γ-collidine (Fig. 13). The buffering effect of base reagents on the catalytic activity of MnO_2 catalysts was examined with electrochemical techniques under forced convection condition as it is possible that the inhibition of pH change at the surface of the catalytic site contributes to the activity enhancement. Fig. 15 shows *j*–*U* curve for the electrodeposited MnO_2 catalyst on glassy carbon electrode under forced convection using rotating disk electrode (RDE). In the absence of base

reagent, the onset potential for the water oxidation current shifted by 20 mV to negative direction with the increase of rotating speed from 0 to 4000 rpm. The addition of 25 mM deprotonated pyridine resulted in the further shift of the onset potential by 100 mV even with the rotating speed of 4000 rpm, indicating that buffering effect is not the sole reason for the enhancement of the water oxidation activity of MnO_2 catalysts by base addition. Thus, the observed increase in KIE and the slope of pH dependence with base pK_a (Fig. 12), together with the concomitant enhancement of the water oxidation activity of the MnO_2 electrode (Fig. 10), and the activity enhancement under forced convection (Fig. 15) demonstrate the successful induction of CPET in the electrocatalytic water oxidation by MnO_2.

The author have demonstrated for the first time the regulation of PCET mechanisms involved in water oxidation by Mn oxides. Because the oxidation of Mn from 2+ to 3+ is associated with a large change in pK_a, the potential of pyridine and its derivatives as a CPET-induction reagents could be evaluated based on the libido rule of general acid-base catalysis. The induction of the CPET reaction by the addition of γ-collidine was confirmed by the clear pH-dependence of $U_{on,j}$, which was shifted by ~60 mV, and the pronounced KIE. While the detection of KIE and compliance of the reactions with the libido rule indicated the successful regulation of PCET mechanisms, the shift of $U_{on,j}$ with pH in the presence of base is not explained directly by a simple model where the base is the proton accepter. As the reaction rate of CPET is a function of the concentration of proton acceptor, the rate is expected to be pH-independent when the concentration of deprotonated forms of base is constant. In this point of view, it is reasonably considered that the pH-dependent rate in the presence of base at the pH higher than base pK_a observed in Fig. 12b could arise from the change of the rate constant for CPET. Yet it should be also noted that the base has the possibility to affect several elementary steps other than the oxidation of Mn from 2+ to 3+ in a curse of electrocatalytic water oxidation.

3.4. Conclusions

In this chapter, the author has demonstrated that the surfaceassociated Mn^{3+} species formed by water oxidation with a MnO_2 electrocatalyst has a different coordination environment depending on solution pH. At alkaline pH, where Mn^{3+} is stabilized by CC, *in situ* UV-vis absorption spectrum showed a blue-shift of the absorption band due to deprotonation of intermediate Mn^{3+} species. The variation of surface groups is likely attributed to a difference in the Mn^{3+} formation process, as the CD efficiency of Mn^{3+} is pH-dependent.

Based on the obtained spectroscopic results, the author attempted the regulation of proton-coupled electron transfer involved in water oxidation by manganese oxides. Pyridine and its derivatives, which have pK_a values intermediate to the water ligand bound to Mn^{2+} and Mn^{3+}, are used as proton-coupled electron transfer induction reagents. The induction of concerted proton-coupled electron transfer is demonstrated by the detection of deuterium kinetic isotope effects and compliance of the reactions with the libido rule.

The regulation of PCET mechanisms is essential for the redox state change of the tetrameric Mn cluster in the Kok cycle of PSII and is likely promoted by amino acids whose pK_a varies according to the redox state of the Mn cluster [37-39]. However, most bioinspired water oxidation catalysts, particularly Mn oxides, lack such a specific regulatory mechanism, as demonstrated by the sharp decline of O_2-evolution activity under neutral conditions for most Mn oxides reported to date [30-35]. Therefore, the author consider that the regulation of PCET, as described in the present study, is an effective approach to lower the η for water oxidation by Mn oxides in neutral media designed for artificial photosynthesis, and will lead to new understanding for the marked difference in catalytic performance between naturally occurring and synthetic Mn catalysts at physiological pH.

References

[1] A. Fujishima, K. Honda, Electrochemical Photolysis of Water at a Semiconductor Electrode. *Nature,* **1972,** *238,* 37-38

[2] A. J. Nozik, Photoelectrochemistry: Applications to Solar Energy Conversion. *Annu. Rev. Phys. Chem.,* **1978,** *29,* 189-222

[3] A. J. Bard, M. A. Fox, Artificial Photosynthesis: Solar Splitting of Water to Hydrogen and Oxygen. *Acc. Chem. Res.,* **1995,** *28,* 141-145

[4] N. S. Lewis, D. G. Nocera, Powering the planet: Chemical challenges in solar energy utilization. *Proc. Natl. Acad. Sci. USA,* **2006,** *103,* 15729-15735

[5] J. P. McEvoy, G. W. Brudvig, Water-Splitting Chemistry of Photosystem II. *Chem. Rev.,* **2006,** *106,* 4455-4483

[6] Y. Zhao, R. Nakamura, K. Kamiya, S. Nakanishi, K. Hashimoto, Nitrogen-doped carbon nanomaterials as non-metal electrocatalysts for water oxidation. *Nat. Commun.,* **2013,** *4,* 2390

[7] H. Dau, I. Zaharieva, M. Haumann, Recent developments in research on water oxidation by photosystem II. *Current Opinion in Chemical Biology,* **2012,** *16,* 3-10

[8] K. Maeda, K. Teramura, D. Lu, T. Takata, N. Saito, Y. Inoue, K. Domen, Photocatalyst releasing hydrogen from water. *Nature,* **2006,** *440,* 295

[9] R. Abe, K. Higashi, K. Domen, Facile Fabrication of an Efficient Oxynitride TaON Photoanode for Overall Water Splitting into H_2 and O_2 under Visible Light Irradiation. *J. Am. Chem. Soc.,* **2010,** *132,* 11828-11829

[10] L. Duan, F. Bozoglian, S. Mandal, B. Stewart, T. Privalov, A. Llobet, L. Sun, A molecular ruthenium catalyst with water-oxidation activity comparable to that of photosystem II. *Nat. Chem.,* **2012,** *4,* 418-423

[11]L. J. Fillol, Z. Codolà, I. Garcia-Bosch, L. Gómez, J. J. Pla, M. Costas, Efficient water oxidation catalysts based on readily available iron coordination complexes. *Nat. Chem.*, **2011,** *3*, 807-813

[12]D. E. Polyansky, J. T. Muckerman, J. Rochford, R. Zong, R. P. Thummel, E. Fujita, Water Oxidation by a Mononuclear Ruthenium Catalyst: Characterization of the Intermediates. *J. Am. Chem. Soc.*, **2011,** *133*, 14649-14665

[13]I. Vass, S. Styring, pH-Dependent Charge Equilibria between Tyrosine-D and the S States in Photosystem II. Estimation of Relative Midpoint Redox Potentials. *Biochemistry*, **1991,** *30*, 830-839

[14] P. Geijer, F. Morvaridi, S. Styring, The S_3 State of the Oxygen-Evolving Complex in Photosystem II Is Converted to the $S_2Y_Z^{\bullet}$ State at Alkaline pH. *Biochemistry*, **2001,** *40*, 10881-10891

[15] J. G. Metz, P. J. Nixon, M. Rogner, G. W. Brudvig, B. A. Diner, Directed Alteration of the D1 Polypeptide of Photosystem II: Evidence That Tyrosine- 161 Is the Redox Component, Z, Connecting the Oxygen-Evolving Complex to the Primary Electron Donor, P680. *Biochemistry*, **1989,** *28*, 6960-6969

[16] Y. Umena, K. Kawakami, J. Shen, N. Kamiya, Crystal structure of oxygen-evolving photosystem II at a resolution of 1.9Å. *Nature*, **2011,** *472*, 55-61

[17] J. Yano, J. Kern, K. Sauer, M. J. Latimer, Y. Puskar, J. Biesiadka, B. Loll, W. Saenger, J. Messinger, A. Zouni, V. K. Yachandra, Where Water Is Oxidized to Dioxygen: Structure of the Photosynthetic Mn_4Ca Cluster. *Science*, **2006,** *314*, 821-825

[18] R. Pace, R. Stranger, S. Petrie, Why nature chose Mn for the water oxidase in Photosystem II. *Dalton Transactions*, **2012,** *41*, 7179-7189

[19] D. M. Robinson, Y. B. Go, M. Greenblatt, G. C. Dismukes, Water Oxidation by λ-

MnO_2: Catalysis by the Cubical Mn_4O_4 Subcluster Obtained by Delithiation of Spinel $LiMn_2O_4$. *J. Am. Chem. Soc.,* **2010,** *132,* 11467-11469

[20] M. M. Najafpour, T. Ehrenberg, M. Wiechen, P. Kurz, Calcium Manganese (III) Oxides ($CaMn_2O_4 \cdot xH_2O$) as Biomimetic Oxygen-Evolving Catalysts. *Angew. Chem. Int. Ed.,* **2010,** *49,* 2233-2237

[21] F. Jiao, H. Frei, Nanostructured manganese oxide clusters supported on mesoporous silica as efficient oxygen-evolving catalysts. *Chem. Commun.,* **2010,** *46,* 2920-2922

[22] M. Yagi, K. Narita, Catalytic O_2 Evolution from Water Induced by Adsorption of $[(OH_2)(Terpy)Mn(\mu\text{-}O)_2Mn(Terpy)(OH_2)]^{3+}$ Complex onto Clay Compounds. *J. Am. Chem. Soc.,* **2004,** *126,* 8084-8085

[23] K. Narita, T. Kuwabara, K. Sone, K. Shimizu, M. Yagi, Characterization and Activity Analysis of Catalytic Water Oxidation Induced by Hybridization of $[(OH_2)(terpy)Mn(\mu\text{-}O)_2Mn(terpy)(OH_2)]^{3+}$ and Clay Compounds. *J. Phys. Chem. B,* **2006,** *110,* 23107-23114

[24] R. Brimblecombe, G. F. Swiegers, G. C. Dismukes, L. Spiccia, Sustained Water Oxidation Photocatalysis by a Bioinspired Manganese Cluster. *Angew. Chem., Int. Ed.,* **2008,** *47,* 7335-7338

[25] J. Limburg, J. S. Vrettos, L. M. Liable-Sands, A. L. Rheingold, R. H. Crabtree, G. W. Brudvig, A Functional Model for O-O Bond Formation by the O_2-Evolving Complex in Photosystem II. *Science,* **1999,** *283,* 1524-1527

[26] Y. Naruta, M. Sasayama, T. Sasaki, Oxygen Evolution by Oxidation of Water with Manganese Porphyrin Dimers. *Angew. Chem., Int. Ed. Engl.,* **1994,** *33,* 1839-1841

[27] Y. Gao, T. Akermark, J. Liu, L. Sun, B. Akermark, Nucleophilic Attack of Hydroxide on a Mn^V Oxo Complex: A Model of the O-O Bond Formation in the Oxygen Evolving Complex of Photosystem II. *J. Am. Chem. Soc.,* **2009,** *131,* 8726-8727

[28] M. M. Najafpour, B. Haghighi, M. Z. Ghobadi, D. J. Sedigh, Nanolayered manganese oxide/poly(4-vinylpyridine) as a biomimetic and very efficient water oxidizing catalyst: toward an artificial enzyme in artificial photosynthesis.*Chem. Comm.,* **2013,** *49,* 8824-8826

[29] F. Cheng, J. Shen, B. Peng, Y. Pan, Z. Tao, J. Chen, Rapid room-temperature synthesis of nanocrystalline spinels as oxygen reduction and evolution electrocatalysts. *Nat. Chem.,* **2011,** *3,* 79-84

[30] R. N. Singh, J. P. Singh, H. N. Cong, P. Chartier, Effect of partial substitution of Cr on electrocatalytic properties of $MnFe_2O_4$ towards O_2- evolution in alkaline medium. *Int. J. Hydrogen Energy,* **2006,** *31,* 1372-1378

[31] M. S. El-Deab, M. I. Awad, A. M. Mohammad, T. Osaka, Enhanced water electrolysis: Electrocatalytic generation of oxygen gas at manganese oxide nanorods modified electrodes. *Electrochem. Commun.,* **2007,** *9,* 2082-2087

[32] M. Morita, C. Iwakura, H. Tamura, The anodic characteristics of massive manganese oxide electrode. *Electrochim. Acta,* **1979,** *24,* 357-362

[33] M. Morita, C. Iwakura, H. Tamura, The anodic characteristics of manganese dioxide electrodes prepared by thermal decomposition of manganese nitrate. *Electrochim. Acta,* **1977,** *22,* 325-328

[34] A. M. Mohammad, M. I. Awad, M. S. El-Deab, T. Okajima, T. Ohsaka, Electrocatalysis by nanoparticles: Optimization of the loading level and operating pH for the oxygen evolution at crystallographically oriented manganese oxide nanorods modified electrodes. *Electrochim. Acta,* **2008,** *53,* 4351-4358

[35] T. Takashima, K. Hashimoto, R. Nakamura, Mechanisms of pH-Dependent Activity for Water Oxidation to Molecular Oxygen by MnO_2 Electrocatalysts. *J. Am. Chem. Soc.,* **2012,** *134,* 1519-1527

[36] T. Takashima, K. Hashimoto, R. Nakamura, Inhibition of Charge Disproportionation of MnO_2 electrocatalysts for Efficient Water Oxidation under Neutral Conditions. *J. Am. Chem. Soc.,* **2012,** *134,* 18153-18156

[37] M. H. V. Huynh, T. J. Meyer, Proton-Coupled Electron Transfer. *Chem. Rev.,* **2007,** *107,* 5004-5064

[38] D. R. Weinberg, C. J. Gagliardi, J. F. Hull, C. F. Murphy, C. A. Kent, B. C. Westlake, A. Paul, D. H. Ess., D. G. McCafferty, T. J. Meyer, Proton-Coupled Electron Transfer. *Chem. Rev.,* **2012,** *112,* 4016-4093

[39] T. J. Meyer, M. H. V. Huynh, H. H. Thorp, The Possible Role of Proton-Coupled Electron Transfer (PCET) in Water Oxidation by Photosystem II. *Angew. Chem., Int. Ed. Engl.,* **1994,** *46,* 5284-5304

[40] M. Sjodin, S. Styring, B. Akermark, L. Sun, L. Hammarström, Proton-Coupled Electron Transfer from Tyrosine in a Tyrosine−Ruthenium−tris-Bipyridine Complex: Comparison with $Tyrosine_Z$ Oxidation in Photosystem II. *J. Am. Chem. Soc.,* **2000,** *122,* 3932-3936

[41] M. Singh, D. N. Thanh, P. Ulbrich, N. Strnadová, F. Štěpánek, Synthesis, characterization and study of arsenate adsorption from aqueous solution by α- and δ-phase manganese dioxide nanoadsorbents. *J. Solid State Chem.,* **2010,** *183,* 2979-2986

[42] N. Cherchour, C. Deslouis, B. Messaoudi, A. Pailleret, pH sensing in aqueous solutions using a MnO_2 thin film electrodeposited on a glassy carbon electrode. *Electrochim. Acta,* **2011,** *56,* 9746-9755

[43] W. Yao, F. J. Millero, Adsorption of Phosphate on Manganese Dioxide in Seawater. *Environ. Sci. Technol.,* **1996,** *30,* 536-541

[44] N. Khare, J. D. Martin, D. Hesterberg, Phosphate bonding configuration on ferrihydrite based on molecular orbital calculations and XANES fingerprinting. **2007,** *71,* 4405-4415

[45] Only at pH 13, we measured the spectrum at 0.9 V, as the probe light was scattered by intensively generated oxygen bubbles at 1.7 V.

[46] pK_{a2} is the second acid dissociation constants of a water ligand.

[47] J. W. Tonkin, L. S. Balistrieri, J. W. Murray, Modeling sorption of divalent metal cations on hydrous manganese oxide using the diffuse double layer model. *Appl. Geochem.*, **2004,** *19,* 29-53

[48] M. Amin, L. Vogt, S. Vassiliev, I. Rivalta, M. M. Sultan, D. H. Bruce, G. W. Brudvig, V. S. Batista, M. R. Gunner., Electrostatic effects on Proton-coupled Electron Transfer in Oxomanganese Complexes Inspired by the Oxygen-Evolving Complex of Photosystem II. *J. Phys. Chem. B,* **2013,** *117,* 6217-6226

[49] F. A. Armstrong, Why did Nature choose manganese to make oxygen? *Phil. Trans. R. Soc. B,* **2008,** *363,* 1263-1270

[50] D. H. Macartney, N. Sutin, Kinetics of the Oxidation of Metal Complexes by Manganese (III) Aquo Ions in Acidic Perchlorate Media: The $Mn(H_2O)_6^{2+}$-$Mn(H_2O)_6^{3+}$ Electron-Exchange Rate Constant. *Inorg. Chem.,* **1985,** *24,* 3403-3409

[51] R. G. Burns, *Mineralogical Applications of Crystal Field Theory*, 2nd edition, Cambridge University Press, UK, **1993,** p.28

[52] E. Silvester, A. Manceau, V. A. Drits, Structure of synthetic monoclinic Na-rich birnessite and hexagonal birnessite: II. Results from chemical studies and EXAFS spectroscopy. *Am. Mineral.,* **1997,** *82,* 962-978

[53] A similar continuous increase in current density was observed by maintaining pH with phosphate buffer. This result also indicates that the mechanism of water oxidation changes by proton accumulation.

[54] J. Medina-Ramos, O. Oyesanya, C. Alvarez, Buffer Effects in the Kinetics of Concerted

Proton-Coupled Electron Transfer: The Electrochemical Oxidation of Glutathione Mediated by $[IrCl_6]^{2-}$ at Variable Buffer pK_a and Concentration. *J. Phys. Chem. C,* **2013,** *117,* 902-912

[55] W. P. Jencks, Requirements for General Acid-Base Catalysis of Complex Reactions. *J. Am. Chem. Soc.,* **1972,** *94,* 4731-4732

[56] W. P. Jencks, General Acid-Base Catalysis of Complex Reactions in Water. *Chem. Rev.,* **1972,** *72,* 705-718

[57] C. Costentin, M. Robert, J. –M. Savéant, A. –L. Teillout, Concerted proton-coupled electron transfers in aquo/hydroxo/oxo metal complexes: Electrochemistry of $[Os^{II}(bpy)_2py(OH_2)]^{2+}$ in water. *Proc. Natl. Acad. Sci. USA,* **2009,** *106,* 11829-11836

[58] C. Constentin, C. Louault, M. Robert, J. –M. Savéant, The electrochemical approach to concerted proton-electron transfers in the oxidation of phenols in water. *Proc. Natl. Acad. Sci. USA,* **2009,** *106,* 18143-18148

[59] C. J. Gagliardi, R. A. Binstead, H. H. Thorp, T. J. Meyer, Concerted Electron-Proton Transfer (EPT) in the Oxidation of Tryptophan with Hydroxide as a Base. *J. Am. Chem. Soc.,* **2011,** *133,* 19594-19597

[60] T. Wang, G. W. Brudvig, V. S. Batista, Study of Proton Coupled Electron Transfer in a Biomimetic Dimanganese water Oxidation Catalyst with Terminal Water Ligands. *J. Chem. Theory Comput.,* **2010,** *6,* 2395-2401

[61] A. K. Covington, M. Paabo, R. A. Robinson, R. G. Bates, Use of the glass electrode in deuterium oxide and the relation between the standardized pD (paD) scale and the operational pH in heavy water. *Anal. Chem.,* **1968,** *40,* 700-706

[62] J. E. Dixon., T. C. Bruice, Dependence of the primary isotope effect (k^H/k^D) on base strength for the primary amine catalyzed ionization of nitroethane. *J. Am. Chem. Soc.,* **1970,** *92,* 905-909

[63] S. Hammes-Schiffer, Theory of Proton-Coupled Electron Transfer in Energy Conversion Processes. *Acc. Chem. Res.* **2009,** *42,* 1881-1889

[64] S. J. Edwards, A. V. Soudackov, S. Hammes-Schiffer, Analysis of Kinetic Isotope Effects for Proton-Coupled Electron Transfer Reactions. *J. Phys. Chem. A*, **2009,** *113,* 2117-2126

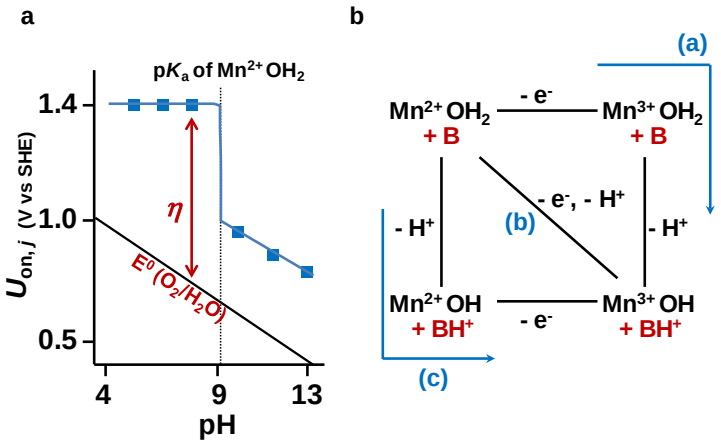

Fig 1 | pH-dependent water oxidation mechanisms by MnO_2 electrodes. a, Schematic illustration of the pH dependence of the onset potential ($U_{on,\,j}$) for water oxidation [35]. Under neutral conditions, $U_{on,\,j}$ does not show pH dependence, whereas it exhibits a linear pH dependence at pHs above 9. The transition point from pH-independent to pH-dependent at pH~9 corresponds to the pK_a of $Mn^{2+}OH_2$. **b,** Thermodynamic cycle for the electrooxidation of Mn^{2+} to Mn^{3+} on the surface of MnO_2 electrodes. The pK_a values of the water ligand bound to Mn^{2+} and Mn^{3+} are 10.6 and 0.7, respectively. Thus, Mn^{2+} and Mn^{3+} exist as protonated and deprotonated forms, respectively, at intermediate pH. B and BH^+ represent the deprotonated and protonated forms, respectively, of a proton acceptor. Copyright 2014, Rights Managed by Nature Publishing Group.

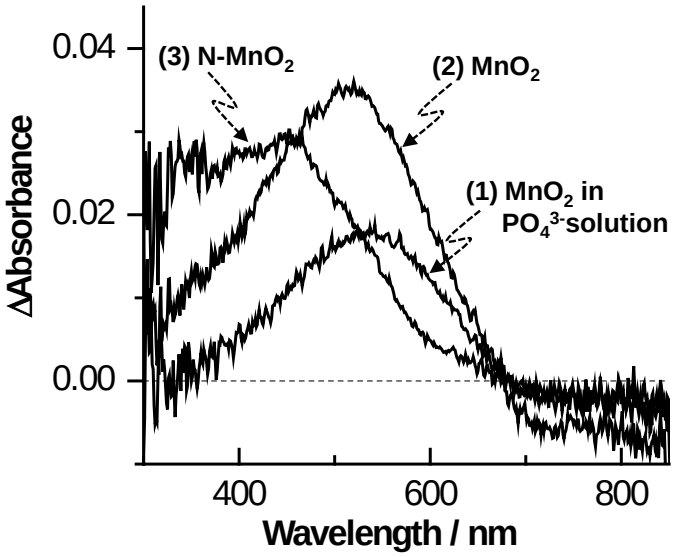

Fig 2 | Difference spectra of a MnO_2 electrode at 1.7 V in (1) 50 mM phosphate buffer and (2) 0.5 M Na_2SO_4 (pH 6). The spectrum measured at 1.1 V was used as a reference spectrum. (3) Mn^{3+} d-d transition spectrum of a MnO_2 electrode coordinated with ammonium groups of poly(allylamine hydrochloride) (N-MnO_2). Details of the preparation of the N-MnO_2 electrode are described in ref. 36. Copyright 2014, Rights Managed by Nature Publishing Group. Copyright 2014, The Electrochemical Society of Japan.

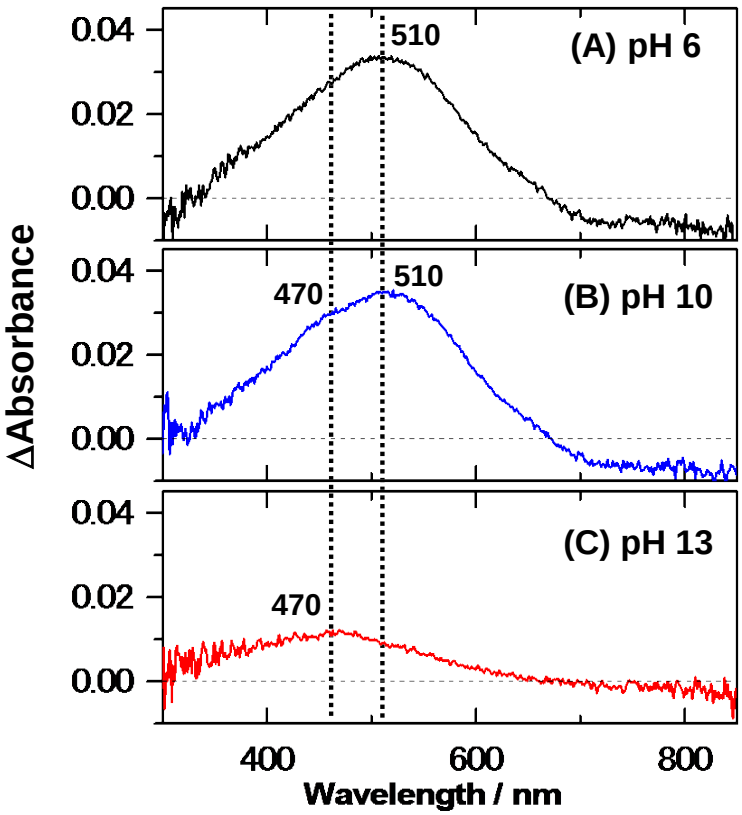

Fig 3 | Comparison of Mn^{3+} d-d transition spectra measured at (A) pH 6 (1.7 V), (B) pH 10 (1.7 V), and (C) pH 13 (0.9 V).

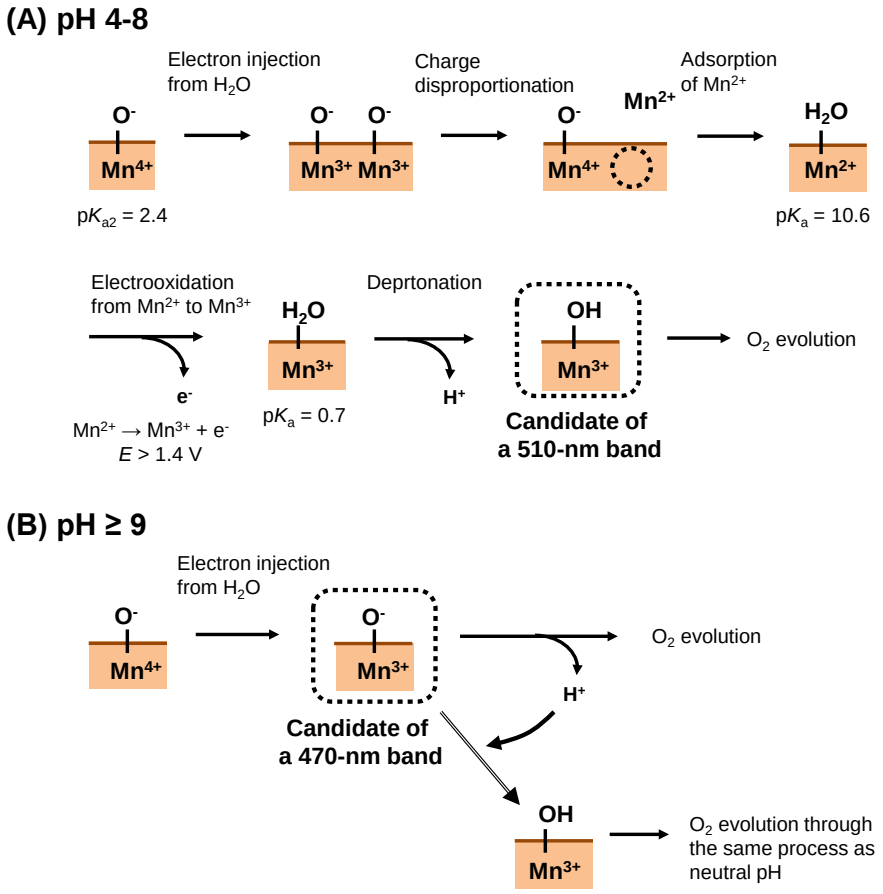

Fig 4 | Proposed model of water oxidation by a MnO_2 electrode at (A) pH 4-8 and (B) pH ≥ 9.

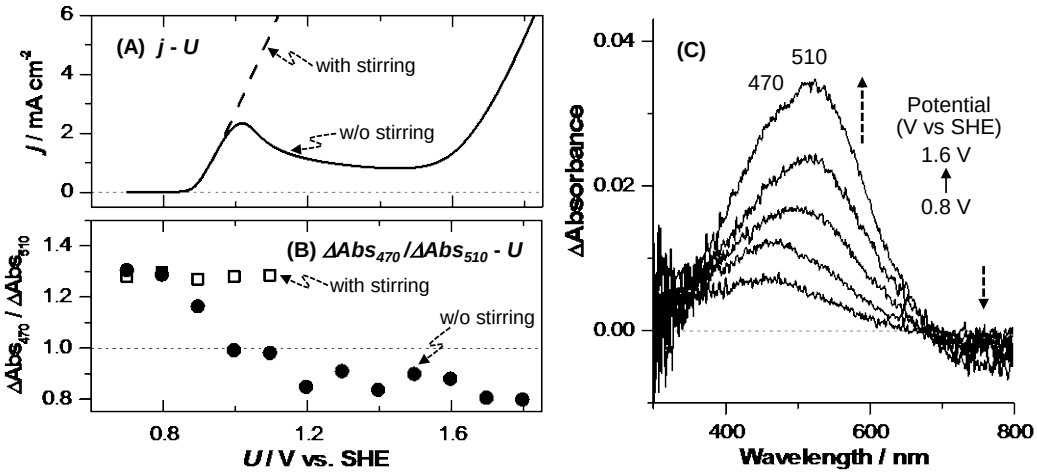

Fig 5 | (A) Current density (*j*) vs potential (*U*) curves for a MnO_2 electrode at pH 12. Solid line; without stirring, Dotted line; with stirring. (B) Potential dependence of the ratio between difference absorbance at 470 nm to that at 510 nm. Closed circles; without stirring, Open squares; with stirring. (C) Changes in the diffuse transmission UV-vis spectra of a MnO_2 electrode measured at increasing potential (0.8, 0.9, 1.1, 1.3, 1.6 V) at pH 12. Copyright 2014, The Electrochemical Society of Japan.

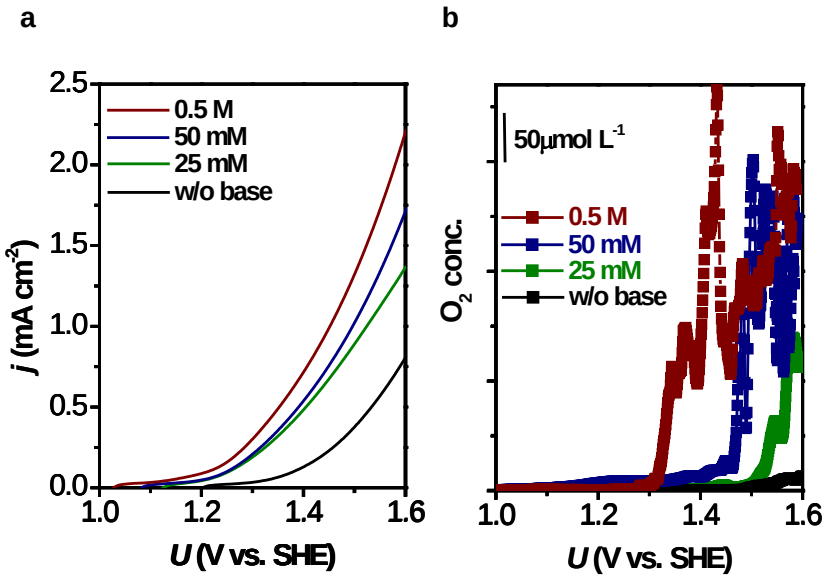

Fig 6 | Enhanced water oxidation activity of MnO_2 electrodes at pH 7.5 by the addition of pyridine. a, Potential dependence of current density for MnO_2 electrodes in presence and absence of pyridine. **b,** Potential dependence of dissolved O_2 concentration for MnO_2 electrodes in presence and absence of pyridine. For both **a** and **b**, the scan rate was 10 mV/s. Copyright 2014, Rights Managed by Nature Publishing Group.

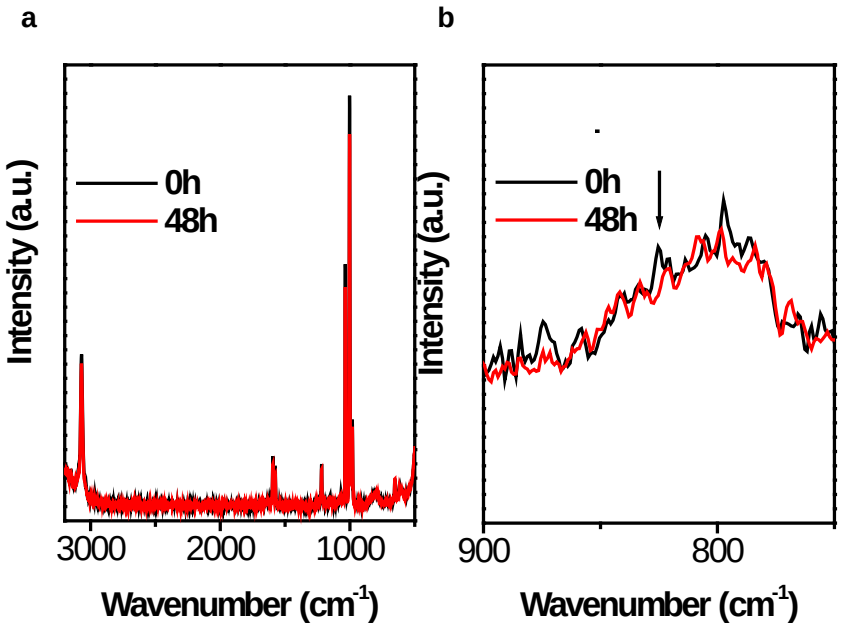

Fig 7 | FT-Raman spectra of electrolytes measured before and after electrolysis for 48h at 1.39 V vs SHE. a. Overall spectra for the electrolyte in the presence of pyridine. Black line indicates spectrum for the condition before the electrolysis and the red line for the condition after electrolysis. **b.** The magnified image of the spectrum region for pyridine-N-oxide. Copyright 2014, Rights Managed by Nature Publishing Group.

Note: Comparison of the spectra before and after electrolysis showed no notable changes in the spectrum corresponding to the pyridine-N-oxide (825 cm^{-1}). Based on the S/N ratio of the spectrum, the amount of pyridine-N-oxides, if it formed, is less than 0.7 % of total pyridine added in the electrolyte.

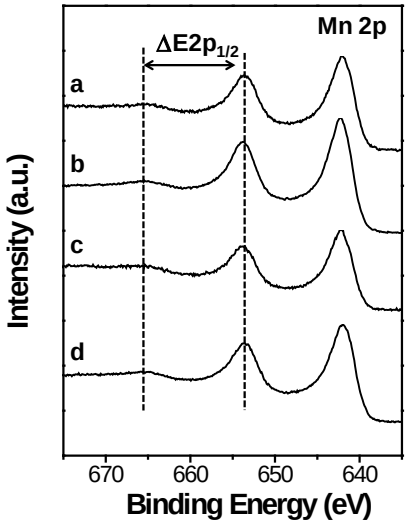

Fig 8 | XPS spectra of MnO_2 electrodes before and after electrolysis at + 1.39 V vs SHE. a. before the electrolysis in the absence of pyridine. **b.** after the electrolysis in the absence of pyridine. **c.** before the electrolysis in the presence of pyridine. **d.** after the electrolysis in the presence of pyridine. Copyright 2014, Rights Managed by Nature Publishing Group.

Note: The oxidation state of Mn in MnO_2 was determined by the relative position of the Mn $2p_{1/2}$ satellite structure ($\Delta E2p_{1/2}$). In the absence of pyridine, the $\Delta E2p_{1/2}$ values for the samples before and after electrolysis were 11.5 eV and 11.7 eV, respectively. These values remained constant at 11.5 eV and 11.7 eV even the electrolysis was conducted in the presence of pyridine. These results indicate that the pyridine addition did not induce the notable change in the electronic structure of Mn species during water oxidation. Also, these results are consistent with the fact that pyridine functions as a CPET inducer via the interaction with water ligands bound to a Mn center, but not direct ligation with a Mn center.

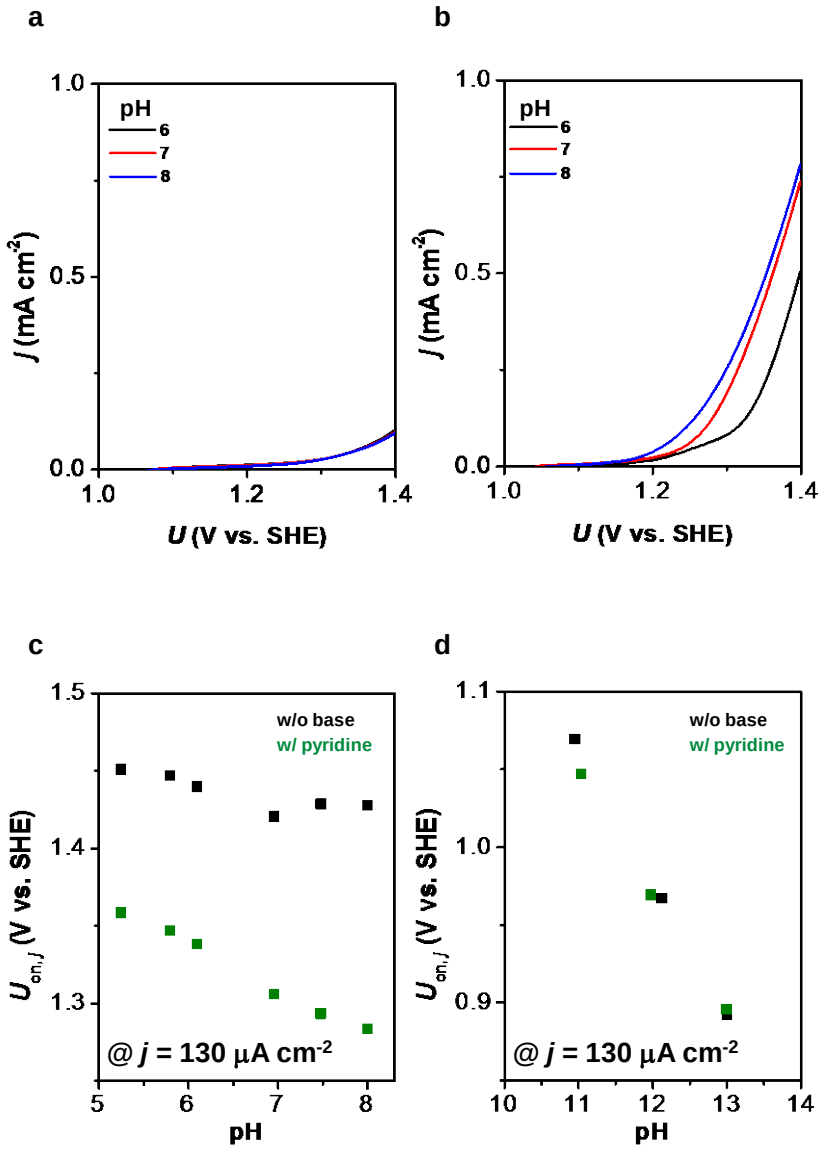

Fig 9 | pH dependence of $U_{on,\,j}$ for MnO_2 electrodes in the presence and absence of 25 mM pyridine. a. Potential dependence of current density for MnO_2 electrodes in the absence of pyridine under neutral conditions. **b.** Potential dependence of current density for MnO_2 electrodes in the presence of 25 mM pyridine under neutral conditions. **c** and **d.** Plot of pH versus potential showing the pH dependence of the onset potential ($U_{on,j}$) defined at 130 μA cm^{-2} for water oxidation in the presence (green squares) and absence (black squares) of pyridine under neutral and alkaline pHs, respectively. Copyright 2014, Rights Managed by Nature Publishing Group.

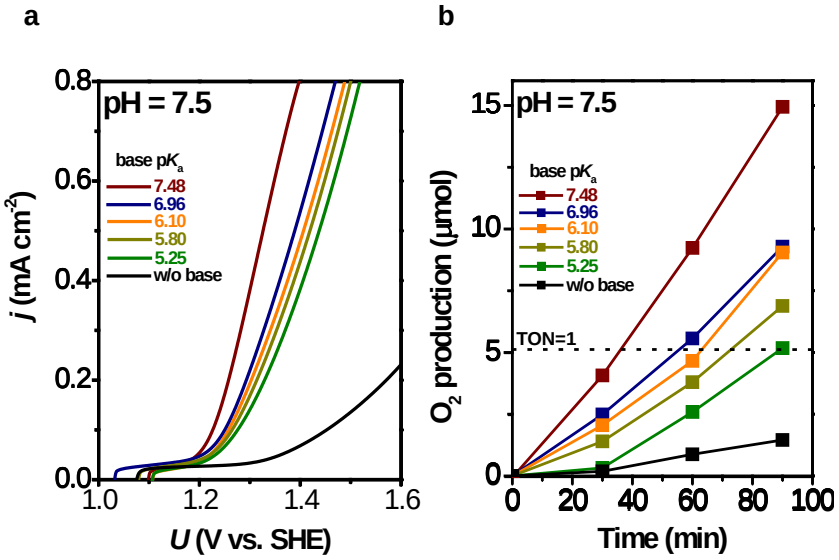

Fig 10 | Effects of base pK_a on electrochemical water-oxidation activity of MnO_2 electrodes at pH 7.5. a, Potential dependence of current density for MnO_2 electrodes in the presence of pyridine (pK_a = 5.25; light green), β-picoline (pK_a = 5.80; olive green), γ-picoline (pK_a = 6.10; orange), 2,6-lutidine (pK_a =6.96; blue), and γ-collidine (pK_a = 7.48; brown). A MnO_2 electrode without the addition of bases to the electrolyte is also depicted as a reference (black). **b,** Time course of O_2 production observed for MnO_2 electrodes at an applied potential of +1.39 V vs SHE in the presence of the bases listed in **a**. The dashed line indicates the value corresponding to TON=1. The concentration of each base was adjusted to 25 mM of the deprotonated form. A MnO_2 electrode without the addition of bases to the electrolyte is also depicted as a reference.

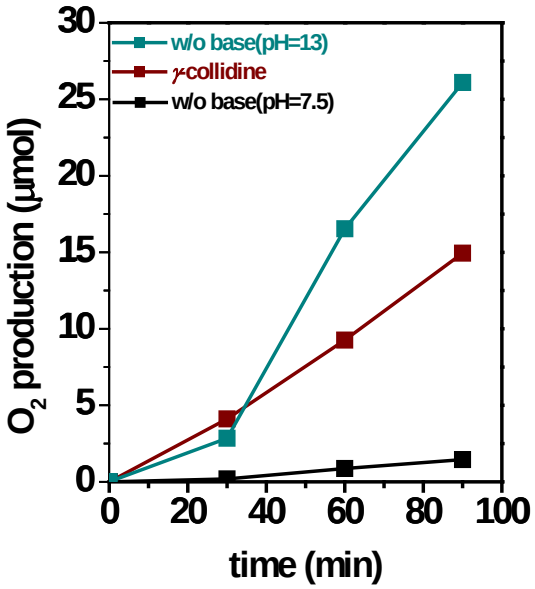

Fig 11 | Time course of O_2 production for MnO_2 electrodes at pH 13. O_2 production by MnO_2 electrodes at pH 7.5 in the presence and absence of γ-collidine are depicted as a comparison. Copyright 2014, Rights Managed by Nature Publishing Group.

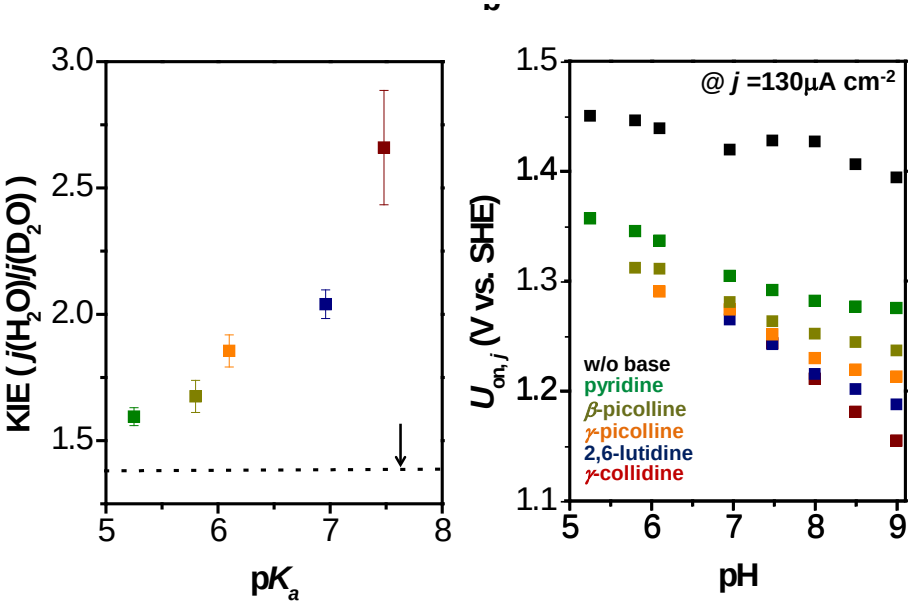

Fig 12 | Regulation of PCET mechanisms by the addition of bases with different pK_a values. **a,** Plot of KIE as a function of the pK_a of the indicated bases at pH (pD) 7.5 at 1.29 V vs SHE. The measured pH value in D_2O was converted to pD value using the equation of pD = measured pH + 0.4. Base concentration: 25 mM of deprotonated form. **b,** Plot of pH versus potential showing the pH dependence of the onset potential ($U_{on,j}$) defined at 130 μA cm^{-2} for water oxidation in the presence of the indicated bases at pHs ranging from 5 to 9. Copyright 2014, Rights Managed by Nature Publishing Group.

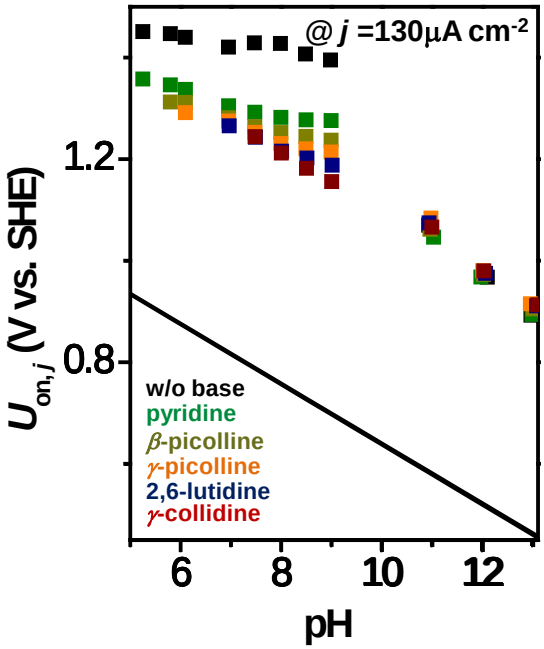

Fig 13 | Plot of pH versus potential showing the pH dependence of the onset potential ($U_{on,j}$) defined at 130 μA cm^{-2} for water oxidation in the presence of the indicated bases at pHs ranging from 5 to 13. The solid line represents the standard potential for the oxygen evolution reaction. Copyright 2014, Rights Managed by Nature Publishing Group.

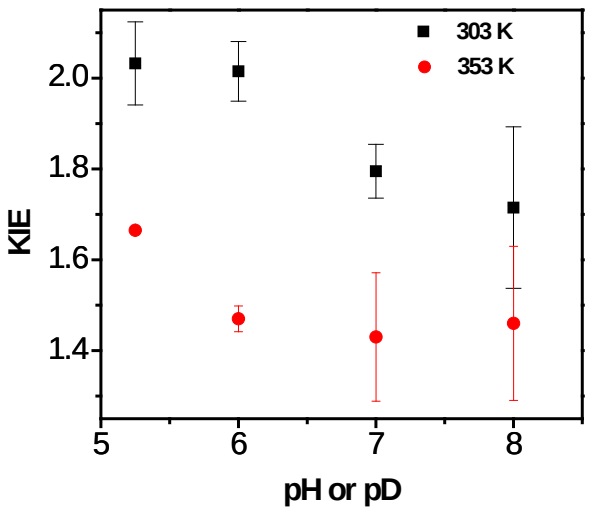

Fig 14 | Plot of KIE as a function of the pH (pD) at 1.83 V vs RHE in the presence of 25 mM of deprotonated form of pyridine. Black squires are measured at 303 K, and red circles at 353 K. The measured pH value in D_2O was converted to pD value using the equation of pD = measured pH + 0.4. Copyright 2014, Rights Managed by Nature Publishing Group.

Note: It was confirmed that KIE decreased with temperature from 303 K to 353 K. Note that the KIE is predicted to decrease with temperature as $KIE = |S_H|^2/|S_D|^2 \exp[-2k_BT(\alpha_D^2 - \alpha_H^2)/M\Omega^2]$, where $\alpha_D > \alpha_H$ because the overlap (S) decreases faster with the equilibrium proton donor-acceptor distance (R) for deuterium than for hydrogen [63,64]. (Ω: the proton donor-acceptor mode frequency, k_B: Boltzmann constant, T: the absolute temperature, α_H or α_D: the exponential dependence of H or D wave function overlap on R, M: the reduced mass for the quantum mechanical harmonic oscillator). Therefore, the decrease in KIE with temperature demonstrates that the rate constant k of PCET for water oxidation is dominantly affected by R and Ω. It was also confirmed that the KIE decreased with pH ranging from 5 to 8 at the constant temperature T. This KIE decrease with pH illustrates that R and Ω varies with pH, as both T and the concentration

of pyridine are kept constant. Proton vibrational wave function overlap decreases with decreasing equilibrium proton donor-acceptor distance. Therefore, we can consider that the chemical origin of the pH dependence of the PCET rate observed in Fig. 8 is due to the decrease of the equilibrium distance and mode frequency of a proton-donor acceptor interface; that is, R and Ω for a water ligand bound to a Mn center and a deprotonated form of pyridine, with pH increase.

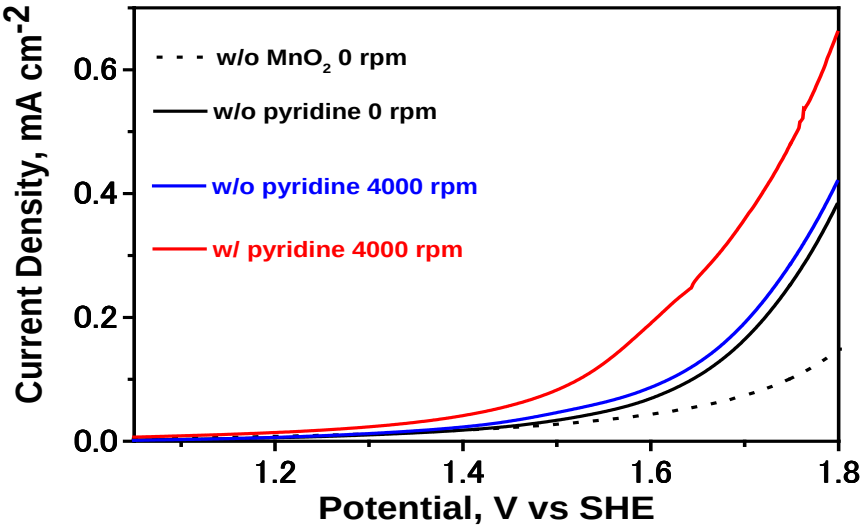

Fig 15 | Enhanced water oxidation activity of MnO_2 electrodes at pH 7.5 by the addition of pyridine under forced convection with rotating disk electrode. Pyridine concentration: 25 mM of deprotonated form. The scan rate was 10 mV/s.

Chapter 4.

Development of electron and proton conductive membrane based on polyoxometalates toward the reaction field for mineral catalysts

4.1. Introduction

General design strategy toward multi-electron transfer catalysts are mainly just focused on reaction site where reactions proceed. In this chapter, the author extend the concept of the function of enzymes from reaction sites to the functions of the surrounding proteins and attempted to develop electron and proton conductive membrane which works as the reaction field for mineral catalysts.

One of the most striking aspects of natural enzymes, for instance photosynthetic systems, is the sophisticated organization of light harvesting site, redox catalytic site, and charge transport chain within the thylakoid membrane. The membrane also achieves the separation of reductive and oxidative process, and the precise management of electron and proton transfer. In addition, reaction fields in enzymatic systems regulate the efficient charge injection to their catalytic center. In photosystem II (PSII), four oxidative equivalents are efficiently transferred into the Mn_4-cluster to promote O_2 evolution reaction in one catalytic cycle. As O_2 evolution from water requires high positive potential (E^0 = 1.23 V vs SHE), the production of the oxidative equivalents is achieved with photo-chemical reaction in PSII and the oxidative equivalents are transferred to the catalytic site without any side reactions. Those properties are essential to maintain the stable catalytic cycle in enzymatic systems, and thus, these could be also important parameters in artificial reaction

fields. However, developments of the reaction fields required for artificial multi-electron transfer catalyst systems remain largely unexplored.

To develop a reaction field satisfying the proton and electron transfer property and the organization of functional component, the author focused on polyoxometalates (POMs). POMs are inorganic transition-metal-oxide clusters with well-defined molecular structures composed of tungsten (WO_6) and/or molybdenum (MoO_6) octahedral and central hetero- atom tetrahedral (XO_4, X = P, Si, etc.) [1]. Due to the flexibility of their molecular properties, including size, shape, charge, and redox potential [2-5], POMs exhibit various catalytic properties. In addition, the framework of POMs possesses the ability to store multiple numbers of electrons [6] and the catalytic sites can be designed by hetero-metal substitution. Considering these properties, POMs are potentially attractive multi-electron transfer catalysts for large numbers of redox reactions, including CO_2 reduction [7], hydrogen evolution [8], and water oxidation reactions [9].

Recently, Takashima et al. demonstrated that an inorganic metal cluster assembly composed of a POM and a Ce^{3+} ion immobilized on the surface of the meso-porous silica (MCM-41) represents a new class of photocatalysts [10-12]. Notably, oxo-bridging $PW_{12}O_{40}$/Ce complexes exhibit metal-to-metal charge transfer (MMCT) from Ce^{3+} to W^{6+} under visible light irradiation. In addition, photo-excitation of the $Ce^{3+} \rightarrow W^{6+}$ MMCT in the clusters initiates the photooxidation of gaseous isopropanol to CO_2 and the reduction of O_2 [10]. The use of an oxo-bridged MMCT unit as a visible light chromophore is one of the promising approaches for the photo-functionalization of POMs. Hill et al. demonstrated MMCT ($Re^{1+} \rightarrow W^{6+}$) using Wells-Dawson type POM-supported $[Re(CO)_3]^+$ complex ($[P_4W_{35}O_{124}\{Re(CO)_3\}_2]^{16-}$) [13]. Recently, Mizuno et al. [14] applied the POM-based MMCT system to artificial photosynthesis and demonstrated H_2 evolution from Pt cocatalyst by the induction of intramolecular MMCT ($Ce^{3+} \rightarrow W^{6+}$) with $TBA_6[\{Ce(H_2O)\}_2\{Ce(CH_3CN)\}_2(\mu_4\text{-}O)(\gamma\text{-}SiW_{10}O_{36})_2]$ (TBA = tetra-*n*-

butylammonium).The photo-functionalized system is one of the suitable candidates to monitor the organization of the functional components since the system can operate well only when the components are ordered properly. Molecular assembly which is capable of CO_2 reduction to CO coupled with water oxidation was achieved by Frei et al. [15], the group has extensively developed bimolecular MMCT units on the surface of mesoporus silica [16-18]. They constructed a Zr-O-Co^{II} MMCT unit coupled to IrO_x water oxidation cluster on the surface of SBA-15 and the visible light irradiation triggered the photosynthesis-like reaction.

In this chapter, the author extended the concept of the inorganic photo-functionalized assembly to a membrane system. POM/polymer membrane composites are widely investigated [19-31] toward various applications such as fuel cells, heterogeneous catalysts and sensors because of unique characteristics of POMs including high electron and proton conductivity. Here the author conducted a photo-functionalization of the POM/polymer membrane by the induction of MMCT reacting with Ce^{3+} and Co^{2+} to activate MnO_x mineral water oxidation catalyst (Fig.1a-1).

The outline of this chapter is shown in Scheme 1. First, as shown in Scheme 1-1, the author fabricated a POM-containing membrane sample with the blending of POM, polyvinyl alcohol (PVA) and polyacrylamide (PAM), followed by a cross-linking process with glutaraldehyde (Glu). MMCT unit was constructed by the reaction of the sample with $Ce(NO_3)_3$ and $CoCl_2$ (Scheme 1-2). The molecular structure of the MMCT unit in polymer matrix was examined by micro-Raman and FT-IR spectroscopic measurement. Electrochemical techniques enable us to determine the redox potential of the MMCT unit in polymer matrix fabricated on electrode. Following the deposition of MnO_x water oxidation catalysts (Scheme 1-3), photoelectrochemical measurement was conducted to confirm the organization of the functional components and electron transfer properties, in other words, the usability of the membrane system as the reaction fields (Scheme 1-4).

4.2. Experiments

4.2.1. Fabrication of POM/polyvinyl alcohol/polyacrylamide (POM/PVA/PAM) membrane sample

The fabrication of self-standing POM/polymer membrane was conducted by blending POM and organic polymers as linkers following the literature reported by Helen et al. [23] except that the total amount of POM in the membrane was different from reported amount to achieve electron conducting ability. The same volume of 10 wt% of PVA (polyvinyl alcohol 1000, completely hydrolyzed, Wako) aq and 2.5 wt% PAM (polyacrylamide, Polysciences. Inc) aq were mixed together at 70 °C and 12 tungsto (VI) phosphoric acid n-hydrate ($H_3PW_{12}O_{40}$, Wako) was added into the mixed solution as the weight ratio of POM / (POM + polymers) was approx. 0.8. After stirring the solution at 70 °C for 6 h, 750 μl of the solution was dropped onto the 5 x 5 cm^2 clean glass substrate held on a hotplate at 130 °C and dried at room temperature in air. Then, the membrane was subjected to PAM anchoring process. The sample on the glass substrate was dipped in the anchoring reagent containing 72 v% distilled water, 24 v% acetone (Wako), 2 v% 25 %-glutaraldehyde solution (Wako), and 2 v% conc. HCl (Wako) for 30 min, and washed with distilled water. After peeling off from the glass substrate, the membrane sample was stored in distilled water. The fabricated samples hereafter will be referred as to POM/PVA/PAM. Samples containing different POMs were fabricated by identical procedure except that Si-centered POM (tungstosilicic acid hydrate, $H_4SiW_{12}O_{40}$, SIGMA-Aldrich) and Boron-centered POM ($K_5BW_{12}O_{40}$) were utilized as POM reagents. Boron-centered POM was synthesized following literature [32]. 6 ml of 6 M HCl was added to 10 ml solution containing 10 g of sodium tungstate (VI) dehydrate (Wako) and 0.5 g of boric acid (Wako) and boiled for 24 h. Following an immediate filtration, the pH of the filtrate was adjusted to 2 with 6 M HCl after cooling. Following an additional boiling for 30 min, 2 g of KCl (Wako) was added to the solution. White

precipitates were collected by filtration, and the obtained sample was washed with diethylether (Wako).

4.2.2. Construction of MMCT unit on POM/PVA/PAM samples

The reaction of POM/PVA/PAM samples with $Ce(NO_3)_3$ or $CoCl_2$ was conducted as follows. The POM/PVA/PAM sample was dipped in a 160 mM $Ce(NO_3)_3 \cdot 6H_2O$ (Wako) or $CoCl_2 \cdot 6H_2O$ (Wako) aq and kept at 80 °C for 5h without stirring, and washed with distilled water. The POM/PVA/PAM sample reacted with $Ce(NO_3)_3$ and $CoCl_2$ will be referred to hereafter as POM/PVA/PAM/Ce and POM/PVA/PAM/Co, respectively. Deposition of MnO_x water oxidation catalysts was conducted with spraying method. 500 ml of MnO_x colloidal solution was prepared by the drop-wise addition of 20 ml of 10 mM $Na_2S_2O_3 \cdot 5H_2O$ (Wako) aq into 10 ml of 25 mM $KMnO_4$ (Wako) aq at room temperature with vigorous stirring followed by dilution to 500 ml [33], and sprayed onto the membrane samples held on a hotplate at 60 °C using an automatic spray gun (Lumina, ST-6). The POM/PVA/PAM, POM/PVA/PAM/Ce and POM/PVA/PAM/Co samples with MnO_x deposits will be referred to hereafter as POM/PVA/PAM/MnO_x, POM/PVA/PAM/Ce/MnO_x and POM/PVA/PAM/Co/MnO_x, respectively. All chemical reagents were used as received without further purification. Characterization of samples was conducted by DEKTAK6M (ULVAC) for the thickness measurement and micro-Raman and IR spectroscopy. Micro-Raman spectra were recorded with a Raman microscope (Senterra, Bruker) with the laser operation of 532 nm and 20 mW. FT-IR spectra of the membrane samples were recorded with a FT-IR spectrometer (Vertex 70, Bruker) in transmission mode with a deuterated triglycine sulfate (DTGS) detector at room temperature. The sample was mounted into an in-house constructed transmission infrared vacuum cell equipped with KBr windows. The UV-Vis spectra of the samples were measured with UV-Vis

spectrometer (MPC-2200, SHIMADZU).

4.2.3. Electrochemical measurement

To conduct electrochemical measurement, the membrane samples were fabricated onto a clean conducting glass substrate (ITO-coated glass, resistance: 20 Ω/square, size: 30 mm × 30 mm; SPD Laboratory, Inc.). Voltammograms were obtained with a commercial potentiostat and potential programmer (HZ-5000, Hokuto Denko), using a Pt wire as the counter electrode and an Ag/AgCl/KCl (sat.) electrode as the reference electrode. The electrolyte solution (0.1 M Na_2SO_4) was prepared using highly pure Milli-Q water (18 $M\Omega^{-1}cm^{-1}$) and reagent-grade chemicals. All measurements were conducted at 30 °C.

Current vs time curves (I – *t* curves) for the membrane samples fabricated onto ITO electrode were obtained in 0.1 M Na_2SO_4 electrolyte (pH = 10 adjusted by 1 M NaOH) under visible light irradiation with applying potential of +1100 mV vs SHE after 20 min of Ar bubbling. The light source was generated with a 300 W Xe lamp (Asahi Spectra, MAX-302) equipped with a UV cut-off filter (Y-47, transparent at wavelength larger than 450 nm; Asahi Glass). Action spectrum was obtained in the same electrolyte utilizing band-pass filter with a half-width of 10-15 nm to obtain monochromatic light.

4.3. Results and discussion

4.3.1. Synthetic strategy

As shown in Scheme 1-1, this work applied cross-linking method to prepare POM/polymer composites membrane. In the case of nafion® or polyvinyl acetate as basal polymers, $H_3PW_{12}O_{40}$-based self-standing membrane was not obtained because of high crystallinity and/or high acidity of $H_3PW_{12}O_{40}$. Thus, utilizing the polyacrylamide as physically strong anchoring reagent, the fabrication of self-standing membrane based on $H_3PW_{12}O_{40}$ was achieved. As to the construction of MMCT unit, POM with H^+ as its counter ion is suitable for the reaction with Ce^{3+} or Co^{2+} as labile cation like proton is necessary for promoting the cation-exchanging reactions with Ce^{3+} and Co^{2+}. Indeed, in the case of homogeneous reaction with Ce^{3+} utilizing POMs which have other cations such as K^+, Na^+, Cs^+, TBA^+ (TBA= tetrabutyl ammonium), the apparent color change was not observed, indicating no MMCT unit was constructed. The thickness of POM/PVA/PAM membrane sample was 100 μm obtained by DEKTAK surface profile measurement for the samples fabricated on glass substrate.

4.3.2. Raman/IR spectroscopic characterization

To confirm that the POM remains intact and that the MMCT unit was successfully constructed, micro-Raman and FT-IR spectroscopic measurement were conducted. Raman spectroscopy is a powerful method for investigating the molecular structure of the polyoxometalate because it is sensitive to the Keggin unit. Micro-Raman spectra of POM/PVA/PAM, POM/PVA/PAM/Ce, POM/PVA/PAM/Co samples and the crystalline $H_3PW_{12}O_{40}$ are shown in Fig. 1a. The crystalline $H_3PW_{12}O_{40}$ exhibits three band peaks at 1013, 236, 221 cm^{-1} (Fig. 1a trace 4). The peak at 1013 cm^{-1} is characteristic for the stretching vibration of terminal W=O, while the peak at 236 cm^{-1} is characteristic for a combination of a symmetric stretching mode of W, four-coordinated oxygen,

and bending motion of a W-O_{2c2}-W bond [34]. The coupling between two bending modes, [δ(O_{2c1}-W=O) and δ(W-O_{2c1}-W)], leads to a peak at 221 cm^{-1} [34]. In the spectrum for POM/PVA/PAM (Fig. 1a trace 1), peaks at 1007 cm^{-1}, 236, 216 cm^{-1} were observed. The peak positions at 236 cm^{-1} are identical to those for bare crystalline $H_3PW_{12}O_{40}$ sample (Fig. 1a trace 4), while the peaks corresponding to the stretching vibration of terminal W=O and the coupling between two bending modes, [δ(O_{2c1}-W=O) and δ(W-O_{2c1}-W)], shifted to lower energy region (1007 cm^{-1} and 216 cm^{-1}). These peak shifts are due to the increase of the distance between POMs and the coulombic interaction between the terminal W=O of POMs and hydroxyl groups of PVA by introduction to the PVA matrix [31]. The stretching vibration of terminal W=O exhibits distinctive spectral feature from that of $PW_{11}O_{40}^{7-}$, which is the hydrolysis product of $PW_{12}O_{40}^{3-}$ [10]. The peak position of W=O band at 1013 cm^{-1} indicates POMs maintain their original Keggin structure in the process of membrane fabrication.

Upon the reaction with Ce^{3+} (trace 2) or Co^{2+} (trace 3), the W=O band slightly shifted from 1007 cm^{-1} to 1006 cm^{-1} for Ce^{3+} and 1005 cm^{-1} for Co^{2+}. These peak shifts indicate the ligand exchange reaction between hydrogen bonded proton to OH group of PVA and Ce^{3+} or Co^{2+} as shown in Scheme 1-2. Therefore, the W-O-Ce/Co MMCT unit was successfully constructed by the reaction with Ce^{3+} and Co^{2+} without any degradation of original Keggin structure. The absence of the peaks corresponding to CeO_2 and Co oxides in the regions of 300-900 cm^{-1} [35, 36] indicates neither CeO_2 nor Co oxides were formed, supporting the successful construction of MMCT unit.

FT-IR spectroscopic measurement was applied to investigate the coordination environment of polymer matrix. FT-IR spectra of PVA/PAM and POM/PVA/PAM membrane samples are shown in Fig. 1b. The broad band assigned to the stretching vibration of O-H group for hydrogen-bonded PVA was observed at 3600 cm^{-1} observed for both samples (not shown). The bands at 2940 cm^{-1} and 1661 cm^{-1} in PVA/PAM sample (trace 1) were assigned to a C-H alkyl stretching band and a

C=O stretching of the acrylamide unit, respectively [23]. The spectra also exhibited a C-H alkyl stretching band and C=O stretching band of glutaraldehyde (Glu) cross-linked to PVA at 2873 cm^{-1} and 1716 cm^{-1}, respectively. Upon the reaction with POM, bands originated from Glu (2873 cm^{-1} and 1716 cm^{-1}) and PAM (1661 cm^{-1}) were shifted to 2865 cm^{-1}, 1664 cm^{-1}, and 1612 cm^{-1}, respectively, while the bands for C-H stretching remains the original position (trace 2), indicating POMs were distributed near the cross-linking reagent and side-chains of polymers, not near the backbone structure of them. All spectroscopic results indicate the intact POM-based MMCT unit was constructed within PVA/PAM polymer metrics.

4.3.3. Optical properties of MMCT unit

To confirm the MMCT unit within POM/PVA/PAM sample, optical measurement was conducted. Following the reaction with Ce^{3+} and Co^{2+}, the apparent sample colors changed from colorless to pale yellow and pink color for samples reacted with Ce^{3+} and Co^{2+}, respectively. UV-Vis diffuse reflectance spectra of the samples before and after the treatment with Ce^{3+} and Co^{2+} are shown in Fig. 2. In the case of bare membrane sample (Fig. 2 trace2), absorption in UV region ($\lambda < 400$ nm) is observed which corresponds to the ligand-to-metal charge transfer (LMCT: O2p $\rightarrow$ W5d). Although small absorption in visible region is observed because of the aggregation of POMs, this membrane sample is almost transparent in the visible light region. Following the reaction with Ce^{3+}, new visible light absorption in the region of 400~600 nm is observed (Fig. 2a trace 1 and inset). As neither bare sample nor membrane samples prepared without POMs reacting with Ce^{3+} possesses the absorption in visible region (Fig. 2a trace 3), the new visible light absorption is assigned to the MMCT from Ce^{3+} to W^{6+}. The absence of Raman peaks corresponding to the formation of CeO_2 supports the assignment (Fig. 1a trace 2). All results obtained from UV-Vis diffuse reflectance and Raman spectroscopy are consistent with the results reported by Takashima

et al [10].

Sample reacted with Co^{2+} also showed new absorption in visible region extending to 650 nm (Fig. 2b trace 2 and inset). A peak at 530 nm is assigned to the d-d transition of Co^{2+}, and as $[Co(H_2O)_6]^{2+}$ possesses its d-d transition absorption maximum at 500 nm (Fig. 2b trace 3), the Co^{2+} in the membrane is in an octahedral coordination environment. [37,38] In addition to this d-d transition absorption, an absorption peak corresponding to MMCT from Co^{2+} to W^{6+} is observed at 400 nm extending to 650 nm. The absence of Raman peaks corresponding to the formation of Co oxides also supports the construction of W-O-Co MMCT unit (Fig. 1a trace 2). The optical properties observed in this work agree with the results reported by Frei et al., who constructed a Ti-O-Co unit on the surface of mesoporous silica (MCM-41) [37,38].

4.3.4. Electrochemical properties of membrane samples

To determine the redox potential of each component, electrochemical methods are the efficient tools. First, we investigated the electrochemical properties of POMs in POM/PVA/PAM membrane sample as the tuning of the redox property of POMs is useful way to control the absorption wavelength of MMCT unit. Redox potential of POMs is tunable by just changing the central atom. Altenau et. al [8,39] examined the redox potential of various POMs ($XW_{12}O_{40}^{n-}$:X = P, Si, Ge, Fe, B, Co, H_2, Cu and $XMo_{12}O_{40}^{n-}$:X = P, Si) and reported that the first redox potential for examined POMs showed anion charge dependence over the range of 600 mV from 0.2 V vs SHE for $PW_{12}O_{40}^{3-}$ to –0.4 V for $CuPW_{12}O^{7-}$. Cyclic voltammograms (CV) for homogeneous aqueous solution of $PW_{12}O_{40}^{3-}$, $SiW_{12}O_{40}^{4-}$, and $BW_{12}O_{40}^{5-}$ are shown in Fig. 3a. The first cathodic peak is shifted to negative potential region with the increase of negative charge of POM anion as reported [8,39]. CVs and differential pulse voltammograms (DPVs) for each membrane samples prepared with $PW_{12}O_{40}^{3-}$, $SiW_{12}O_{40}^{4-}$, and $BW_{12}O_{40}^{5-}$ as POM reagents are shown in Fig. 3b and

c. Several redox peaks were observed in the potential region more negative than 0.1 V in each voltammograms, which reflects the multi-electron oxidation/reduction property of POMs. When the potential was swept to the redox region of POMs, apparent color change to blue color corresponding to inter-valence charge transfer (IVCT) between W^{5+} and W^{6+} was observed, which is the characteristics of "heteropoly blue" [40]. Thus, POMs are electrochemically-active even in the polymer matrix. By altering the central atom from P to Si or B, the first reduction potential of the membranes was shifted from 0.07 V for $PW_{12}O_{40}^{3-}$—based membrane to -0.26 V for $BW_{12}O_{40}^{5-}$. The degree of potential shifts is identical to the reported values [8, 39], and observed peak shifts in CVs for corresponding homogeneous POMs solution (Fig. 3a). Thus, it is confirmed that the redox property of POMs are maintained in the polymer matrix, namely, the MMCT unit with the suitable redox potential can be constructed with in the polymer matrix fabricated in this work.

To examine the electron transfer property of the membrane system through POM molecules, plots of cathodic peak current in CVs for the membrane samples with different POM loading amount against the POM amount is shown in Fig. 4. The peak currents increase with the POM amount with zero intercept. The maximum POM amount for monolayer is calculated to 0.2 nmol cm^{-2} considering that the diameter of one POM molecule is 1 nm. Therefore the linear increase of peak current indicates the electron tunneling from POM molecule to POM molecule [19,21,26,28,30]. The sample used for further analysis corresponds to 2.6 μmol cm^{-2} with the thickness of 100 μm. Thus, it is confirmed that the membrane sample fabricated in this work satisfies the electron conduction properties required to operate as appropriate reaction field.

Next, we examined the redox potential of MMCT unit in polymer matrix. In addition to the redox potential of POMs, the redox potential of electron donor metal site is fundamental information to apply POM/PVA/PAM to photo-induced electron transfer system. Cyclic voltammograms of

POM/PVA/PAM/Ce and POM/PVA/PAM/Co membrane samples fabricated on ITO electrode are shown in Fig. 5. Following the reaction with Ce^{3+}, new redox couple with the midpoint potential at 1.5 V was observed in pH = 1 (Fig. 5a solid line), which corresponds to Ce^{4+}/Ce^{3+} couple. Compared with the standard redox potential of Ce^{4+}/Ce^{3+} (+1.71 V), the observed redox potential negatively shifted. This potential shift reflects the coordination environment change from free aqueous ions to oxo-bridged W-O-Ce unit observed in micro-Raman spectra (Fig. 1a trace 2) and/or to the insertion into negatively-charged environment of hydroxyl group of PVA matrix. It is reported [41] that lanthanide metal cation (Ln) reacted with monovacant POMs ($XW_{11}O_{40}^{n-}$) constructs a dimer of the POM, $Ln(XW_{11}O_{40}^{n-})_2$, and that the redox potential largely shifted to negative direction (+0.6 V vs SHE at pH = 4.5). In this work, the extent of the negative shift is 200 mV, supporting the fact that POM retains its original structure. This result is consistent with the obtained Raman spectrum after treatment with Ce^{3+} (Fig. 1a trace 2).

To confirm the effect of the redox potential of the donor metal site, this work subjected to the reaction of the membrane sample with Co^{2+} in addition to Ce^{3+} because standard redox potential of Co^{3+}/Co^{2+} couple is more positive than that of Ce^{4+}/Ce^{3+}, which is advantageous to activate MnO_x water oxidation catalyst. Fig. 1b shows the cyclic voltammogram of samples after treated with Co^{2+}. Compare with the bare sample shown in Fig. 1b (dashed line), an oxidation current increase in the potential region more positive than +1.8 V was observed. Considering the standard redox potential of Co^{3+}/Co^{2+} couple (+1.92V) and the absence of the cathodic process, the current increase can be assigned to the water oxidation on Co site under electrochemical condition. Thus, the redox potential of Co^{3+}/Co^{2+} in POM/PVA/PAM/Co is +1.8 V or in more positive region. As the redox potential of Co^{3+}/Co^{2+} couple in our membrane system positioned at more positive than the value for Ce^{4+}/Ce^{3+} couple, generated holes at Co sites are more advantageous toward oxygen evolution from water than that generated at Ce sites.

4.3.5. Photo-induced charge transfer property

To confirm generated Ce^{4+} and Co^{2+} by MMCT can activate MnO_x catalyst, photoelectrochemical measurement was conducted under visible light illumination following the deposition of MnO_x catalyst onto POM/PVA/PAM/Ce and POM/PVA/PAM/Co samples with spraying method [42]. The current vs time curves of (trace 1) POM/PVA/PAM/Co/MnO_x, (trace 2) POM/PVA/PAM/Ce/MnO_x, (trace 3) POM/PVA/PAM/Co and (trace 4) POM/PVA/PAM/MnO_x membrane samples posed at +1100 mV are shown in Fig. 6. For trimetalic sample composed of W, Co and Mn (trace 1), the photocurrent was observed under visible light irradiation ($\lambda > 450$ nm). This result indicates that the excited electrons are conducted through the membrane sample and collected by ITO electrode. As a control experiment, photoelectrochemical measurement was onducted for other dimetalic samples fabricated without Co or MnO_x, resulting in small photo-current production compared with trimetalic samples. These observations clearly indicate that each metal centers plays crucial roles in visible light-induced charge transfer. Note that the sample reacted with Ce^{3+} demonstrated smaller photocurrent compared with the sample treated with Co^{2+} (trace 2), reflecting the stronger oxidizing power of Co^{3+} than Ce^{4+} and the flexible tuning of the redox potential of the membrane system by altering the metal ion. The photoelectrochemical results are consistent with those of UV-Vis measurement that the absorption maximums of MMCT are 420 nm for POM/PVA/PAM/Ce and 395 nm for POM/PVA/PAM/Co, respectively, reflecting the more positive redox potential of Co^{2+} site.

To confirm that the observed photo current is originated from MMCT excitation, the action spectrum for POM/PVA/PAM/Co/MnO_x sample was examined as shown in Fig. 7. The observed photocurrent corresponds to the absorption in visible region which appeared after the reaction with Co^{2+} except for the d-d transition of Co^{2+} at 530 nm, indicating the origin of collected electrons at the electrode is MMCT excitation.

Visible light irradiation can induce MMCT (Co 3d → W 5d) and the electrons at POM sites are transferred to the ITO electrode through the membrane. On the other hand, the generated hole at Co site is transferred to MnO_x deposit. In previous report [42], O_2 evolution current on MnO_x electrode was observed in the potential region more positive than +1.5 V. The redox potential of Co site in the membrane sample is in the potential region more positive than +1.8 V (Fig. 5b), thus, the generated holes at Co site possess sufficient oxidizing power to promote the oxidation of water on MnO_x catalysts (Fig. 8). The more negative redox potential for Ce^{4+}/Ce^{3+} couple than Co^{3+}/Co^{2+} couple agrees with the observation that the generated photocurrent is smaller for the sample treated with Ce^{3+} than that with Co^{2+}.

4.4. Conclusions

In this chapter, the author developed the photo-functionalized membrane samples by MMCT to develop reaction fields where the mineral catalysts promote multi-electron transfer reactions. POM/polymer-based self-standing membrane was fabricated with cross linking method utilizing PVA as basal polymer and PAM as cross linking reagent. The molecular structure and the redox properties of POMs are maintained in the polymer matrix as confirmed by Raman spectroscopy and electrochemical measurements. To photo-functionalize the membrane sample, they were subjected to construct MMCT chromophore assembly with a reaction of Ce^{3+} and Co^{2+}. The appearance of new absorption band in visible region indicated that the MMCT from Ce^{3+} or Co^{2+} to W^{6+} was successfully induced. The photoelectrochemical measurement under visible light illumination demonstrated that the generated holes can be transferred to MnO_x deposit while the excited electrons can be conducted through the membrane sample. It is notable that only trimetric (W, Co, Mn) system promoted the photoelectrochemical electron transfer indicating the appropriate organization of functional components (catalyst, light harvesting site and electron transfer site) is achieved in the membrane system. The result is a suitable demonstration to confirm the usability of the system as the reaction field which manages electron and proton transfer, and the ordering the functional components to maintain the catalytic cycles.

References

[1] M. T. Pope, *Heteropoly and Isopoly Oxomatalates,* Springer, New York, **1983**

[2] M. Sadakane, E. Steckhan, Electrochemical Properties of Polyoxometalates as Electrocatalysts. *Chem. Rev.,* **1998,** *98,* 219-237

[3] I. A. Weinstock, Homogeneous-Phase Electron-Transfer Reactions of Polyoxometalates. *Chem. Rev.,* **1998,** *98,* 113-170

[4] T. Yamase, Photo- and Electrochromism of polyoxometalates and Related Materials. *Chem. Rev.,* **1998,** *98,* 307-325

[5] T. Okuhara, N. Mizuno, M. Misono, Catalytic Chemistry of Heteropoly Compounds. *Adv. Catal.,* **1996,** *41,* 113-252

[6] M. T. Pope, G. M. Varga Jr, Heteropoly Blues. I. Reduction Stoichiometries and Reduction Potentials of Some 12-Tungstates. *Inorg. Chem.,* **1966,** *5,* 1249-1254

[7] A. M. Khenkin, I. Efremenko, L. Weiner, J. M. L. Martin, R. Neumann, Photochemical Reduction of Carbon Dioxide Catalyzed by a Ruthenium-Substituted Polyoxometalate. *Chem. Eur. J.,* **2010,** *16,* 1356-1364

[8] B. Keita, S. Floquet, J. –F. Lemonnier, E. Cadot, A. Kachmar, M. Bénard, M. –M. Rohmer, L. Nadjo, A New Class of Efficient Electrocatalysts for the Reduction of Protons into Hydrogen Based on the $[Mo_2O_2S_2]^{2+}$ Building Block. *J. Phys. Chem. C,* **2008,** *112,* 1109-1114

[9] Q. Yin, J. M. Tan, C. Besson, Y. V. Geletti, D. G. Musaev, A. E. Kuznetsov, Z. Luo, K. I. Hardcastle, C. L. Hill, A Fast Soluble Carbon-Free Molecular Water Oxidation Catalyst Based on Abundant Metals. *Science,* **2010,** *328,* 342-345

[10] T. Takashima, R. Nakamura, K. Hashimoto, Visible Light Sensitive Metal Oxide Nanocluster Photocatalysts: Photo-Induced Charge Transfer from Ce(III) to Keggin-Type

Polyoxotungstates. *J. Phys. Chem. C,* **2009,** *113,* 17247-17253

[11] T. Takashima, A. Yamaguchi, K. Hashimoto, R. Nakamura, Multielectron-transfer reactions at single Cu(II) centers embedded in polyoxotungstates driven by photo-induced metal-to-metal charge transfer from anchored Ce(III) to framework W(VI). *Chem. Commun.,* **2012,** *48,* 2964-2966

[12] T. Takashima, R. Nakamura, K. Hashimoto, Visible-Light-Absorbing Lindqvist-Type Polyoxometalates as Building Blocks for All-Inorganic Photosynthetic Assemblies. *Electrochemistry,* **2011,** *79,* 783-786

[13] C. Zhao, Z. Huang, W. Rodríguez-Córdoba, C. S. Kambara, K. P. O'Halloran, K. I. Hardcastle, D. G. Musaev, T. Lian, C. L. Hill, Synthesis and Characterization of a Metal-to-Polyoxometalate Charge Transfer Molecular Chromophore. *J. Am. Chem. Soc.,* **2011,** *133,* 20134-20137

[14] K. Suzuki, F. Tang, Y. Kikukawa, K. Yamaguchi, N. Mizuno, Hydrogen Evolution Using the Visible-light-induced Metal-to-polyoxometalate Multiple Electron Transfer. *Chem. Lett.,* **2014,** *43,* 1429-1431

[15] W. Kim, G. Yuan, B. A. McClure, H. Frei, Light Induced Carbon Dioxide Reduction by Water at Binuclear $ZrOCo^{II}$ Unit Coupled to Ir Oxide Nanocluster Catalyst. *J. Am. Chem. Soc.,* **2014,** *136,* 11034-11042

[16] W. Lin, H. Frei, Anchored Metal-to-Metal Charge-Transfer Chromophores in a Mesoporous Silicate Sieve for Visible-Light Activation of Titanium Centers. *J. Phys. Chem. B,* **2005,** *109,* 4929-4935

[17] W. Lin, H. Frei, Photochemical CO_2 Splitting by Metal-to-Metal Charge Transfer Excitaion in Mesoporous ZrCu(I)-MCM-41 Silicate Sieve. *J. Am. Chem. Soc.,* **2005,** *127,* 1610-1611

[18] W. Lin, H. Frei, Bimetallic redox sites for photochemical CO_2 splitting in mesoporous silicate

sieve. *C. R. Chimie,* **2006,** *9,* 207-213

[19] S. Liu, Z. Tang, Polyoxometalate-based functional nanostructured films: Current progress and future prospects. *Nano Today,* **2010,** *5,* 267-281

[20] M. Clemente-León, C. Mingotaud, B. Agricole, C. J. Gómez-García, E. Coronado, P. Delhaès, Application of the Langmuir-Blodgett Technique to Polyoxometalates: Towards New Magnetic Films. *Angew. Chem. Int. Ed. Engl.,* **1997,** *36,* 1114-1116

[21] D. M. Fernandes, H. M. Carapuca, C. M. A. Brett, A. M. V. Cavaleiro, Electrochemical behavior of self-assembly multilayer films based on iron-substituted α-Keggin polyoxotungstates. *Thin Solid Films,* **2010,** *518,* 5881-5888

[22] M. Ammam, B. Keita, L. Nadjo, I. –M. Mbomekalle, J. Fransaer, Attempts to immobilize catalytically active substituted-heteropolytungstates in multilayer film of charged polyelectrolyte poly(allylamine hydrochloride). *J. Electroanal. Chem.,* **2010,** *645,* 65-73

[23] M. Helen, B. Viswanathan, S. S. Murthy, Poly(vinyl alcohol)-Polyacrylamide Blends with Cesium Salts of Heteropolyacid as a Polymer Electrolyte for Direct Methanol Fuel Cell Applications. *Journal of Applied Polymer Science,* **2010,** *116,* 3437-3447

[24] M. Amirinejad, S. S. Madaeni, E. Rafiee, S. Amirinejad, Cesium hydrogen salt of heteropolyacids/Nafion nanocomposite membranes for proton exchange membrane fuel cells. *Journal of Membrane Science,* **2011,** *377,* 89-98

[25] D. R. Vernon, F. Meng, S. F. Dec, D. L. Williamson, J. A. Turner, A. M. Herring, Synthesis, characterization, and conductivity measurements of hybrid membranes containing a mono-lacunary heteropolyacid for PEM fuel cell applications. *Journal of Power Sources,* **2005,** *139,* 141-151

[26] S. Liu, D. G. Kurth, B. Bredenkötter, D. Volkmer, The Structure of Self-Assembled Multilayers with Polyoxometalate Nanoclusters. *J. Am. Chem. Soc.,* **2002,** *124,* 12279-12287

[27] M. Amirinejad, S. S. Madaeni, M. A. Navarra, E. Rafiee, B. Scrosati, Preparation and characterization of phosphotungstic acid-derived salt/Nafion nanocomposite membranes for proton exchange membrane fuel cells. *Journal of Power Sources,* **2011,** *196,* 988-998

[28] A. M. Douvas, E. Makarona, N. Glezos, P. Argitis, J. A. Mielczarski, E. Mielczarski, Polyoxometalate-Based Layered Structures for Charge Transport Control in Molecular Devices. *ACS NANO,* **2008,** *2,* 733-742

[29] S. Zhao, Q. Wu, Preparation and conductivity of hybrid materials containing undecatungstocobaltoindic heteropoly acid and polymer matrix. *Materials Letters,* **2006,** *60,* 2650-2652

[30] S. Gao, R. Cao, X. Li, Self-assembly of Keggin-type tungstoborate-based multilayer films and their electrochemical behavior. *Thin Solid Films,* **2006,** *500,* 283-288

[31] A. Lewera, G. Zukowska, K. Miecznikowski, M. Chojak, W. Wieczorek, P. J. Kulesza, Solid-state electroanalytical characterization of the nonaqueous proton-conducting redox gel containing polyoxometallates. *Analytica Chimica Acta,* **2005,** *536,* 275-281

[32] C. Rocchiccioli-Deltcheff, M. Fournier, R. Franck, R. Thouvenot, Vibrational Investigations of Polyoxometalates. 2. Evidence for Anion-Anion Interactions in Molybdenum(VI) and Tungsten (VI) Compounds Related to the Keggin Structure. *Inorg. Chem.,* **1983,** *22,* 207-216

[33] J. F. Perez-Benito, E. Brillas, R. Pouplana, Identification of a Soluble Form of Colloidal Manganese(IV). *Inorg. Chem.,* **1989,** *28,* 390-392

[34] A. J. Bridgeman, Density functional study of the vibrational frequencies of α-Keggin heteropolyanions. *Chem. Phys.,* **2003,** *287,* 55-69

[35] W. H. Weber, K. C. Hass, J. R. McBride, Raman study of CeO_2: Second-order scattering, lattice dynamics, and particle-size effects. *Phys. Rev. B,* **1993,** *48,* 178-185

[36] J. Yang, H. Liu, W. N. Martens, R. L. Frost, Synthesis and Characterization of Cobalt Hydroxide, Cobalt Oxyhydroxide, and Cobalt Oxide Nanodiscs. *J. Phys. Chem. C,* **2010,** *114,* 111-119

[37] H. Han, H. Frei, Visible light absorption of binuclear $TiOCo^{II}$ charge-transfer unit assembled in mesoporous silica. *Microporous and Mesoporous Materials,* **2007,** *103,* 265-272

[38] H. Han, H. Frei, Controlled Assembly of Hetero-binuclear Sites on Mesoporous Silica: Visible Light Charge-Transfer Units with Selectable Redox Properties. *J. Phys. Chem. C,* **2008,** *112,* 8391-8399

[39] J. J. Altenau, M. T. Pope, R. A. Prados, H. So, Models for Heteropoly Blues. Degrees of Valence Trapping in Vanadium(IV)- and Molybdenum(V)-Substituted Keggin Anions. *Inorg. Chem.,* **1975,** *14,* 417-421

[40] G. M. Varga Jr, E. Papaconstantinou, M. T. Pope, Heteropoly Blues. IV. Spectroscopic and Magnetic Properties of Some Reduced Polytungstates. *Inorg. Chem.,* **1970,** *9,* 662-667

[41] N. Haraguchi, Y. Okaue, T. Isobe, Y. Matsuda, Stabilization of Tetravalent Cerium upon Coordination of Unsaturated Heteropolytungstate Anions. *Inorg. Chem.,* **1994,** *33,* 1015-1020

[42] T. Takashima, K. Hashimoto, R. Nakamura, Mechanism of pH-Dependent Activity for Water Oxidation to Molecular Oxygen by MnO_2 Electrocatalysts. *J. Am. Chem. Soc.,* **2012,** *134,* 1519-1527

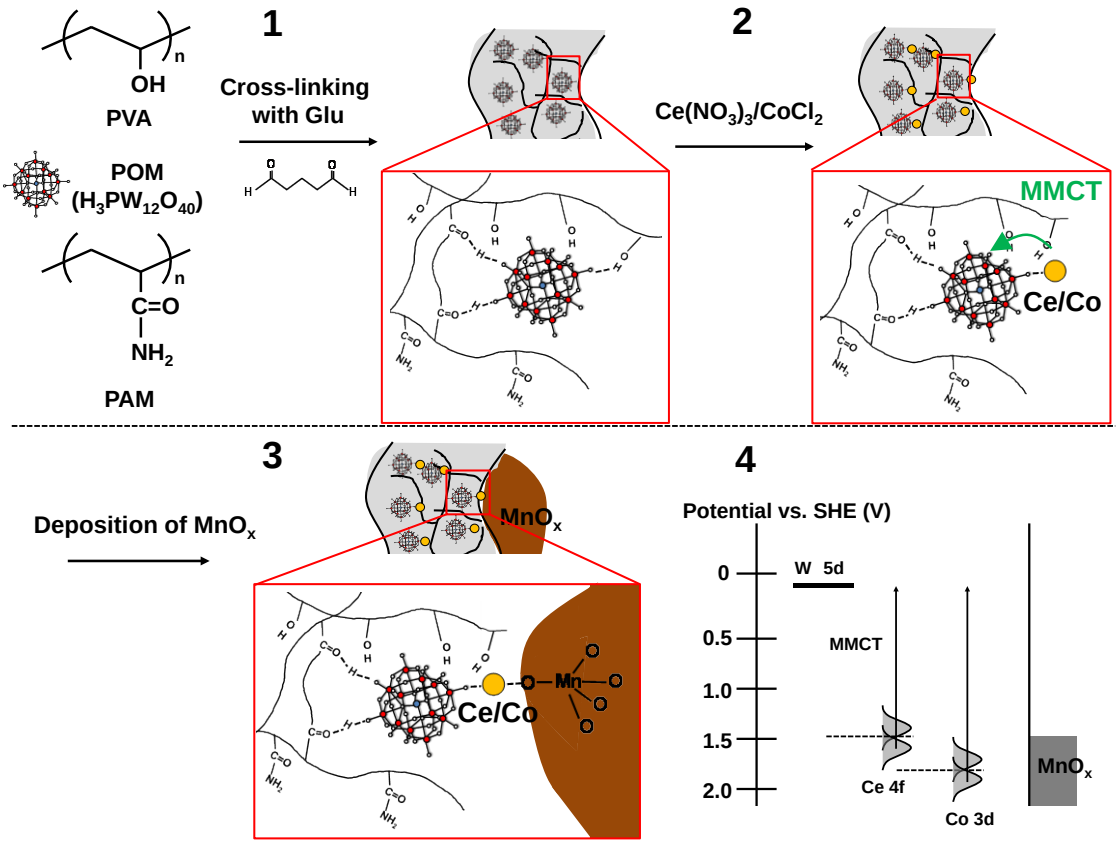

Scheme 1 The outline of this chapter. (1)Membrane sample was fabricated by the mixing POM, PVA and PAM, followed by the cross linking process with glutaraldehyde (Glu). (2)To construct MMCT unit, the samples were subjected to react with $Ce(NO_3)_3$ and $CoCl_2$ and the structure was investigated with micro-Raman and FT-IR measurements. Electrochemical techniques provided the information concerning the redox potential of the donor site (Ce^{III} and Co^{II}). (3)Following the deposition of MnO_x water oxidation catalyst, (4)photoelectrochemical measurement was conducted to demonstrate the validity of our concept that POM-based MMCT unit can activate MnO_x water oxidation catalysts. Here, visible light irradiation induces MMCT (Ce 4f or Co 3d → W 5d) and the generated hole and the excited electron are collected by MnO_x catalyst and electrode, respectively.

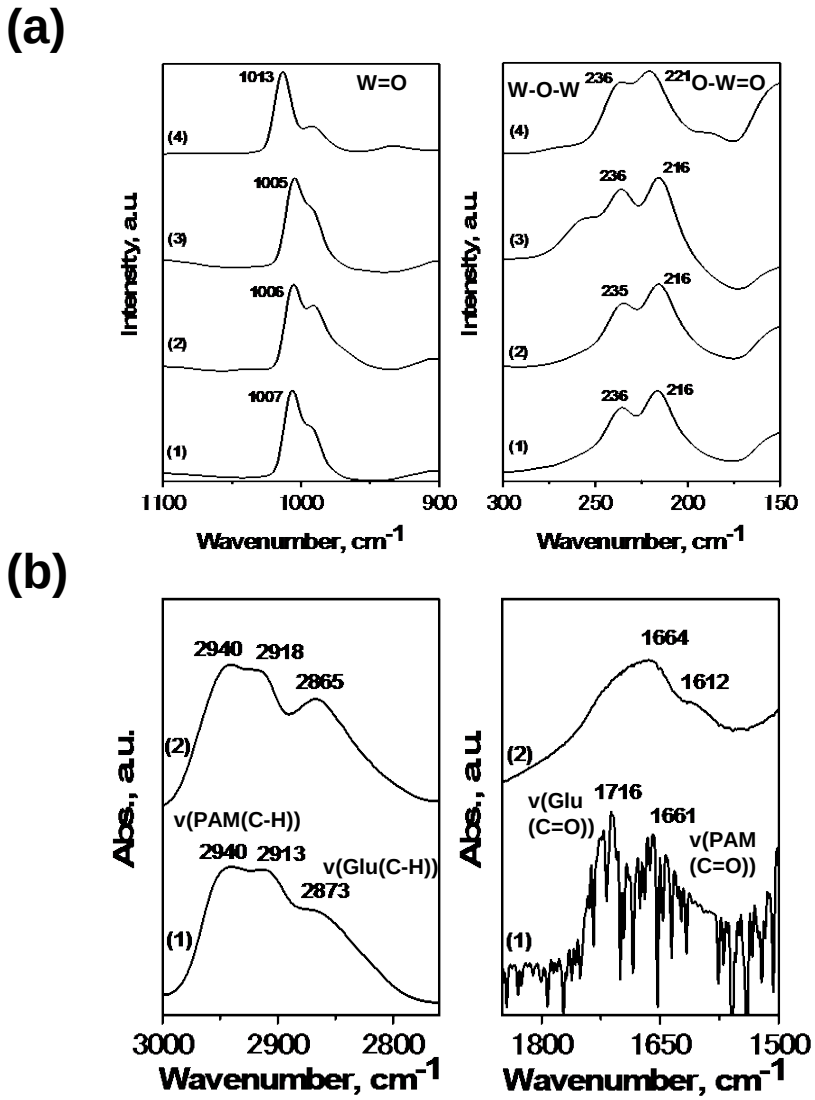

Fig. 1 (a) Micro-Raman spectra of the membrane samples before (POM/PVA/PAM: trace 1) and after the reaction with $Ce(NO_3)_3$ (POM/PVA/PAM/Ce: trace 2) or $CoCl_2$ (POM/PVA/PAM/Co: trace 3). The spectrum for crystalline $H_3PW_{12}O_{40}$ is shown for the reference (trace 4). Laser intensity was 20 mW. (b) FT-IR spectra of (trace 1) PVA/PAM and (trace 2) POM/PVA/PAM membrane samples.

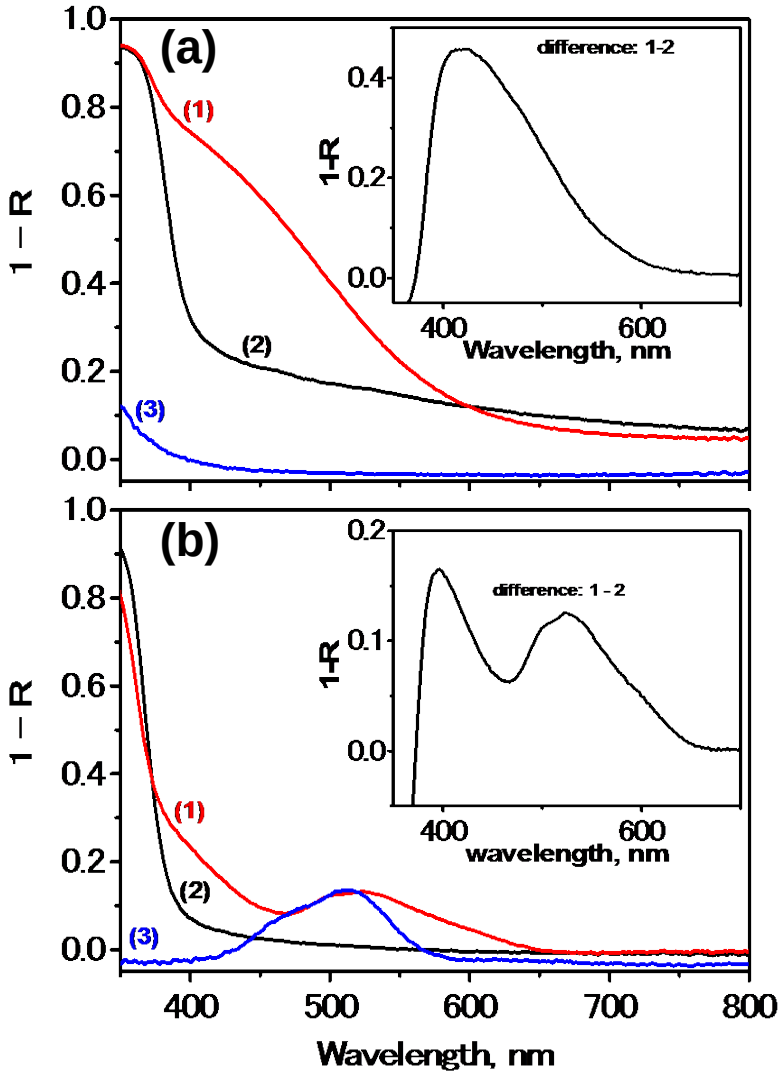

Fig. 2 UV-Vis diffuse reflectance spectra of the membrane samples reacted with (a) Ce^{3+} and (b) Co^{2+}. Trace 1: samples after reacted with Ce^{3+} or Co^{2+}, trace 2: bare samples, trace 3: (a) PVA/PAM/Ce, (b) UV-Vis absorption spectra of aqueous solution $CoCl_2$ in absorbance unit. The insets are the subtraction spectra of before and after reaction with Ce^{3+} and Co^{2+}.

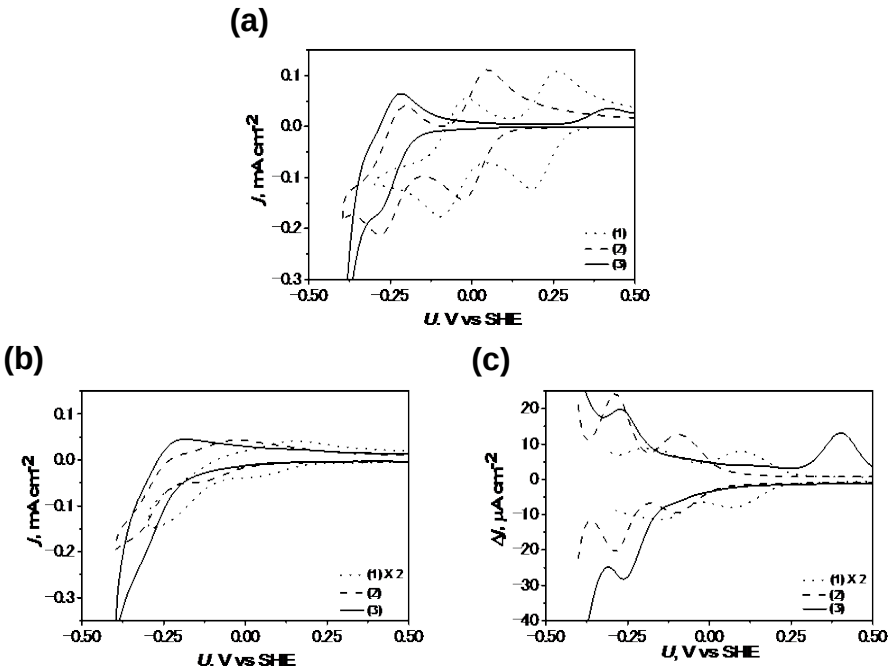

Fig. 3 (a) Cyclic voltammograms (CVs) of 1 mM POM solutions, (b) POM/PVA/PAM membrane samples fabricated on ITO electrode, and (c) differential pulse voltammograms (DPVs) of membrane samples. Traces 1, 2 and 3 corresponds to POM = $H_3PW_{12}O_{40}$, $H_4SiW_{12}O_{40}$ and $K_5BW_{12}O_{40}$, respectively. The electrolyte was 0.1 M Na_2SO_4 aq (pH = 1). For CV measurement, scan rate was 100 mV/s. For DPV measurement, ΔE was 10 mV.

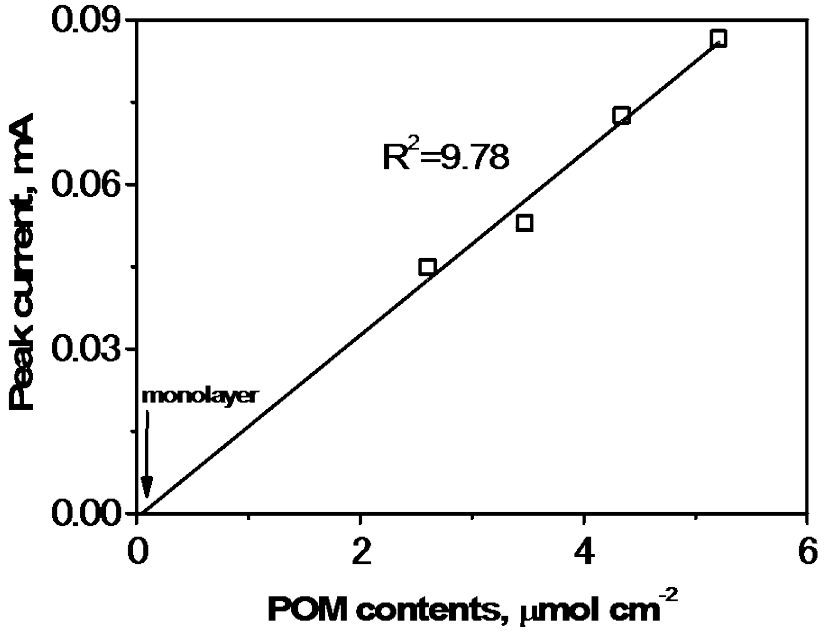

Fig. 4 The peak current (at 0.07 V) vs. POM contents plot. The electrolyte was 0.1 M Na_2SO_4 aq and the scan rate was 50 mV/s under Ar atmosphere. The arrow shows a corresponding value to the amount of POM of monolayer.

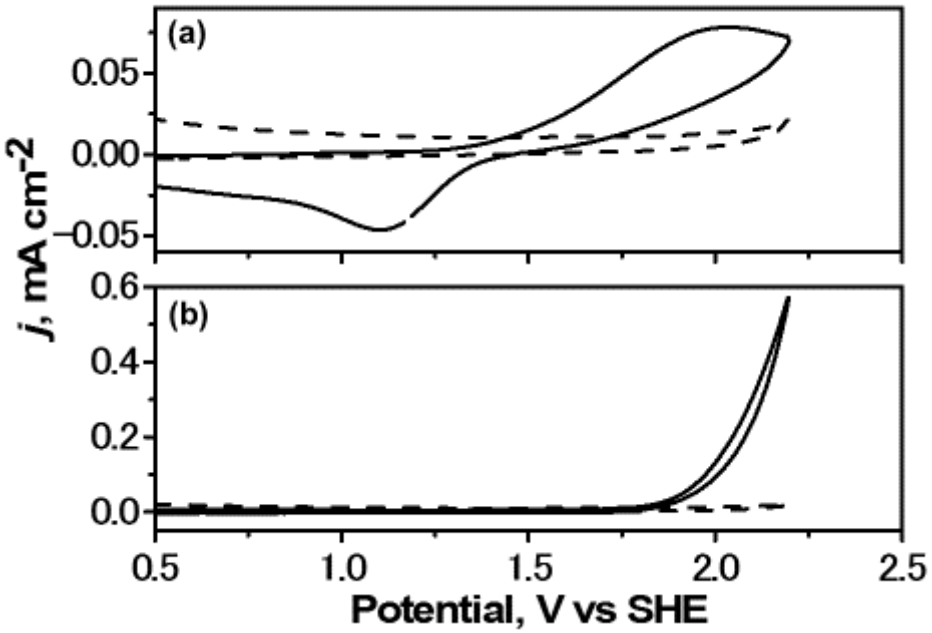

Fig. 5 Cyclic voltammograms of membrane samples after reaction with (a, solid line) $Ce(NO_3)_3$ (POM/PVA/PAM/Ce) or (b) $CoCl_2$ (POM/PVA/PAM/Co) under Ar condition. The voltammogram for POM/PVA/PAM sample is shown as a control (dashed line). The electrolyte was 0.1 M Na_2SO_4 aq (pH = 1), and the scan rate was 100 mV/s.

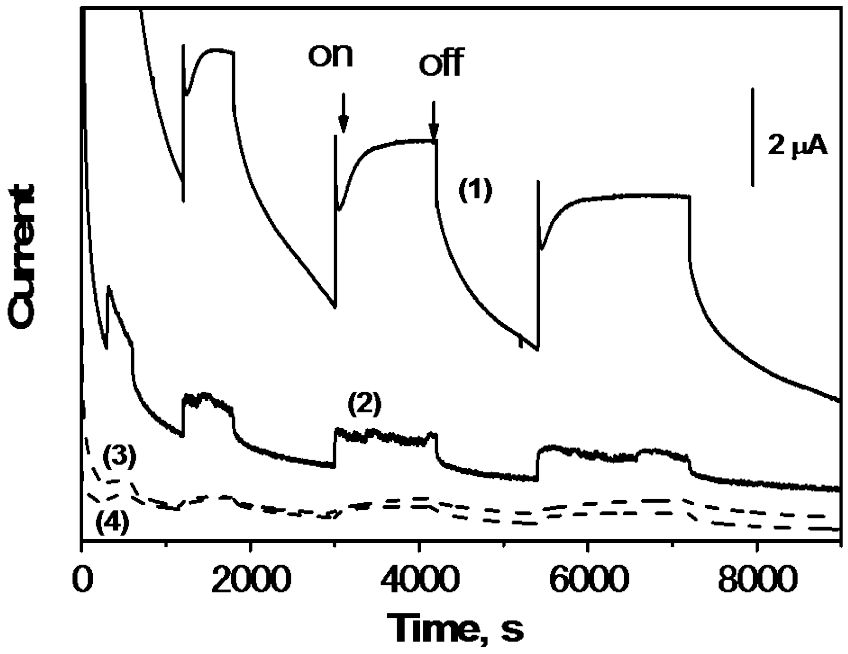

Fig. 6 Current vs time curves **(**I - t curves) for (1) POM/PVA/PAM/Co/MnO_x, (2) POM/PVA/PAM/Ce/MnO_x, (3) POM/PVA/PAM/Co and (4) POM/PVA/PAM/MnO_x samples fabricated on ITO electrode under visible-light irradiation. The light source was 300 W Xe lamp and a cutoff filter at 450 nm was utilized to avoid the absorption of UV light.

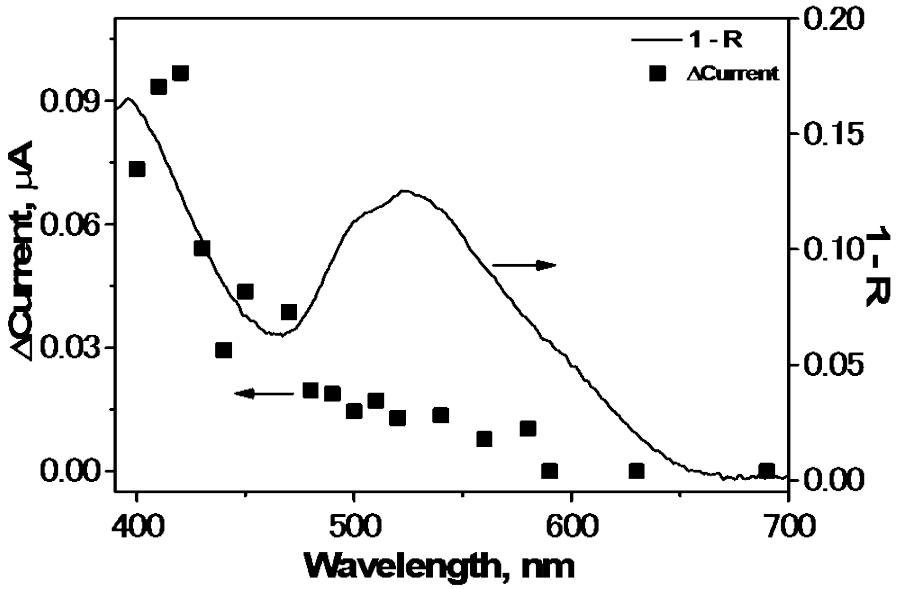

Fig. 7 The action spectrum for POM/PVA/PAM/Co/MnO_x sample (closed square). The solid line indicates the UV-Vis diffuse reflectance subtraction spectrum obtained from trace 1 – trace 2 in Fig.2b.

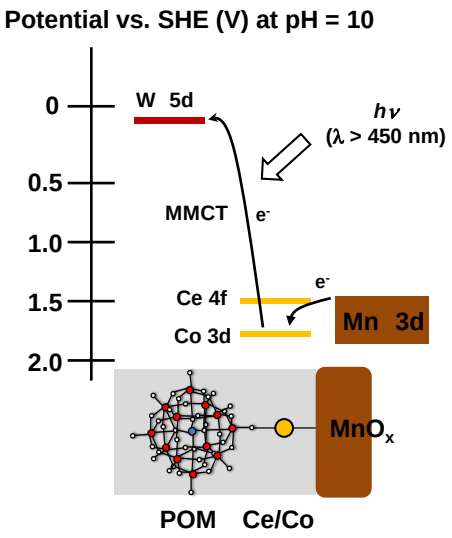

Fig. 8 Energy diagram of the relevant redox species in the fabricated membrane samples.

Chapter 5.

Conclusion and Perspective

Conclusion

Functionalization of iron sulfides and manganese oxides as CO_2 reduction and O_2 evolution multi-electron transfer catalysts, respectively, was achieved by the controlling the intermediate by the regulation of electron and proton transfer. Furthermore, the reaction field in which catalysts promote chemical reactions was developed by focusing the characteristics of polyoxometalates. The reaction field can manage the electron and proton transfer and the organization of the required components for the reactions confirmed by photoelectrochemical techniques. Although the learning from natural system is one of the promising approaches for the catalyst design, most of the “bio-mimetic” works focus only on the structural motif of the enzymes. In this study, the author focused on the function of the natural system, and attempted to apply the function to artificial systems.

In chapter 2, the author succeeded to enhance the CO_2 reduction activity of iron sulfide minerals by the modification with Ni^{2+} ion and N-containing polymers. Although the iron sulfides like greigite (Fe_3S_4) are hypothesized to contribute to the emergence of life at deep sea hydrothermal vent by the reduction of CO_2 to organic compounds due to its structural similarity to the present CO_2 reduction enzymes, its catalytic activity was hardly examined. In this work, the catalytic properties of greigite were examined and the CO_2 reduction activity of greigite under aqueous solution is verified to be very low due to the competition with H_2 evolution. To regulate the intermediate species in the CO_2 reduction process, Ni^{2+}, which had existed in deep sea, and N-containing polymer were introduced to the system. As a result, the faradaic efficiency for CO_2

reduction was improved approx. 85 fold compared with bare greigite. The improvement of the catalytic activity for CO_2 reduction on the iron sulfide by modification with Ni^{2+} and N-containing electron-donating polymer indicates that the catalyst design based not only on the structure, but on the properties of the minerals including the surrounding environment is one of the promising approaches to functionalize the minerals as multi-electron transfer catalysts.

The investigation on the catalytic activity of iron sulfides for CO_2 reduction brought the deep insight concerning the prebiotic organic synthesis to author. He proposed models that the pH difference (Proton Motive Force: PMF) of 3-4 unit between hydrothermal fluid and sea water is required to promote CO_2 reduction on iron sulfides and that the storage of hydrogen into iron sulfides plays a crucial role to maintain the PMF. The models include the kinetic consideration and explain the reaction sustainability issues, which are not taken into consideration in existing models.

Not only for iron sulfide minerals, which play the key role in chemoautotrophic process near deep sea hydrothermal vent, but also for manganese oxide minerals, the functionalization as water oxidation catalysts were achieved as described in chapter 3. In natural photosynthesis, manganese oxide cluster is essential to extract electrons from water to fix carbons, and the origin of the manganese oxide cluster is suggested to manganese oxide minerals. Manganese oxide minerals demonstrated high catalytic O_2 evolution activity at alkaline pH while the activity drastically decreased at neutral pH due to the inherent instability of intermediate Mn^{3+} toward disproportionation reaction ($2Mn^{3+} \rightarrow Mn^{2+} + Mn^{4+}$) under neutral conditions. *In situ* electrospectroscopic measurements enabled the author to obtain the further insight concerning the protonation state of intermediate Mn^{3+} and to make sure the reaction process between under neutral and alkaline pH is totally different. At neutral pH, proton transfer is not involved in the rate-determining process of water oxidation reaction on manganese oxide electrode and this is

quite different from the natural system in which concerted proton-electron transfer (CPET) proceeds. In this work, CPET induction during the rate-determining step of the water oxidation process on manganese oxide minerals was attempted and the author succeeded to enhance the catalytic activity by the introduction of pyridine and pyridine derivatives which satisfy the libido rule. The success tells us that the understanding and the application of the function of natural enzymes to artificial materials is one of the important strategies to functionalize minerals as multi-electron transfer catalysts.

Through chapter 2 and chapter 3, functionalization of minerals as reaction site was attempted. In following chapter 4, the proton and electron conductive membrane was fabricated to construct reaction field for the mineral catalysts. In addition to the reaction center, the development of reaction filed which can transport electron, proton, and reaction substrate efficiently and organize the redox components is another important factor to construct efficient and stable reaction systems. To realize the reaction field with artificial systems, the author focused on the characteristics of polyoxometalate (POM) like electron and proton conductivity and adopted a POM/polymer hybrid system. The usability of the fabricated membrane was conducted by photoelectrochemical techniques after the photo-functionalization with hetero transition metal element and the deposition of manganese oxide catalysts as reaction site. Larger photo-current was observed for the trimetalic W, Co, and Mn systems, demonstrating the achievement of the rectification of electron transfer and the ordered setting of the redox centers.

At last, the works described above offer the opportunity to utilize metal sulfide and oxide minerals as multi-electron transfer catalysts by regulating electron and proton transfer. Moreover, the reaction field for catalytic active center is constructed by extending the concept of the function of enzyme from reaction center to the surrounding protein networks. In summary, the understanding of the function and essential physic-chemical parameters of enzymes and the

application of the knowledge to artificial systems is one of the promising approaches to construct efficient catalysts based on naturally-abundant 3d block metal elements for CO_2 reduction, O_2 evolution, and other various multi-electron transfer reactions.

Perspective

Author attempted to functionalize iron sulfide and manganese oxide minerals as CO_2 reduction and O_2 evolution catalysts respectively, and succeeded to enhance the catalytic activity by modification of the surrounding environment the catalysts. Moreover, he developed the proton-electron conducting membrane which can work as the reaction fields for the catalysts like enzymatic proton- and substrate-conducting networks. However, the issues we should tackle to are still remained. One of the big issues to develop more sophisticated catalysts is the reaction selectivity. As described in this work, CO_2 reduction reaction competes with hydrogen evolution, and O_2 evolution also compete with the oxidative decomposition of co-existing base reagents. On the other hand, when we compare the natural H_2 evolution and CO_2 reduction enzymes, both of the active centers are composed of Fe-Ni-S cluster [1,2]. Each enzyme promotes each reaction with high selectivity in spite of the structural similarity of active centers: namely, to achieve the high selectivity, structural imitation is not enough, and extraction of the essential physicochemical parameters is required. One possible candidate of such a parameter is the spin state of Ni(II) site as described in section 1.4.1 [3,4].

When we focus on the natural O_2 evolution process, the large turnover number is achieved [5] without the decomposition of surrounding amino acid residues in spite of the fact that the O_2 evolution reaction requires strongest oxidative power in biological systems [6]. Therefore, the exploring of the physicochemical properties which manage the kinetic selectivity of amino acid residues can bring us insights concerning not only the catalysts with high selectivity, but the biological challenging issues.

The approach taken in this work can be applied to the other multi-electron transfer catalysts, namely, the understanding of the function of the enzymes and its application to artificial materials is one of the promising approach to design the efficient catalysts.

For instance, several kinds of natural O_2 reducing enzymes possess Fe or Cu centers in their active centers [7-9]. However, most efficient catalysts for O_2 reduction so far is Pt-based catalysts, and first-row transition metal based catalysts generally exhibit low activity. Recently, Fe-N coordinating graphene-based catalysts was reported and the onset potential for O_2 reduction under acidic condition was 850 mV vs RHE [10]. In this material, the isolated Fe ion and electron-donating N ligand works as active site, which is structural and functional similarity to the enzymatic systems [9]. Thus, this is one of the representative works of biomimetic approach to functionalize first-row transition metal element-based materials as efficient catalysts like taken by this work.

One of the "holly grail" reactions for chemists is the partial oxidation of methane to methanol ($CH_4 + H_2O \rightarrow CH_3OH + 2H^+ + 2e^-$), which is the extremely difficult reaction because the oxidation of methanol is thermodynamically favorable than that of methane. In nature, this reaction is catalyzed by methane monoxigenase (MMO) whose active center utilizes Fe as reaction center [11]. In spite of the high catalytic activity of the enzyme, artificial catalysts achieving the reaction are very limited even for noble metal-based catalysts [12]. In the reaction cycle of MMO, Fe^{IV} is proposed to acts as the precursor for the reaction [13]. Notably, Fe^{4+} is vulnerable to charge disproportionation reaction resulting in the formation of Fe^{3+} and Fe^{4+}. Thus, the understanding of the mechanism in natural enzyme to suppress the charge disproportionation reaction can open the opportunity to accomplish methane partial oxidation reaction based on first-row transition metal elements. Not only examples mentioned above, but for other reactions such as ammonia oxidation and nitrogen fixation can be enhanced by the exploring the functional difference between artificial materials and corresponding enzymes.

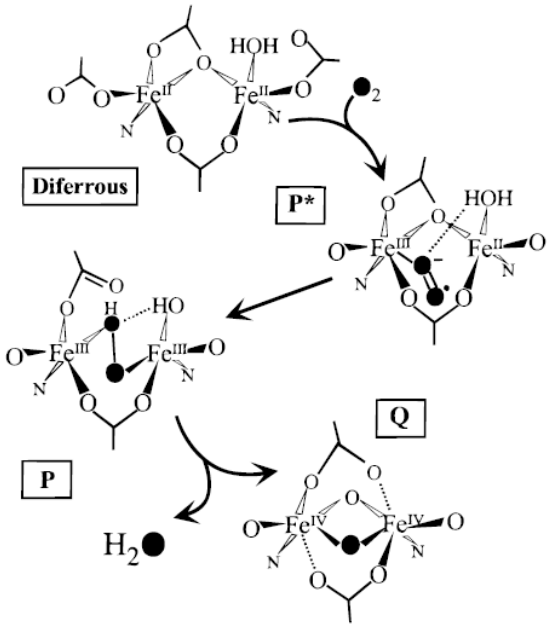

Fig.1 MMO catalytic Cycle for the O_2 activation. (Reprinted with permission from ref. 13. Copyright 1999, American Chemical Society)

In addition to catalytic design, results in this work can provide us new insights concerning geographic and oceanographic issues. One of the striking examples is the existence of Mn^{3+} in nature. The reason for low O_2 evolution activity of MnO_2 electrode under neutral condition is the inherent instability of Mn^{3+} [14]. Despite the instability of Mn^{3+} on artificial MnO_2 materials, Mn^{3+} is found in various natural systems including the photosynthetic water oxidation center [15]. For instance, soluble Mn^{3+} is found in the suboxic zone of the Black Sea, where the concentration of molecular oxygen is very low [16-18]. Manganese is one of the important chemical species to manage redox cycles ocean to form the chemical gradient in the oxygen-deficient zones shown in fig.2 due to its multiple valence. Trouwborst et al. examined the Mn^{3+} concentration in regions of Black Sea and Chesapeake Bay by utilizing electrochemical techniques after chelating Mn^{3+} with desferroxamine-B [16] and soluble Mn^{3+} with concentrations of up to 4 μM was detected. This finding has required a major revision of the understanding concerning the geochemical cycle

related to manganese [17].

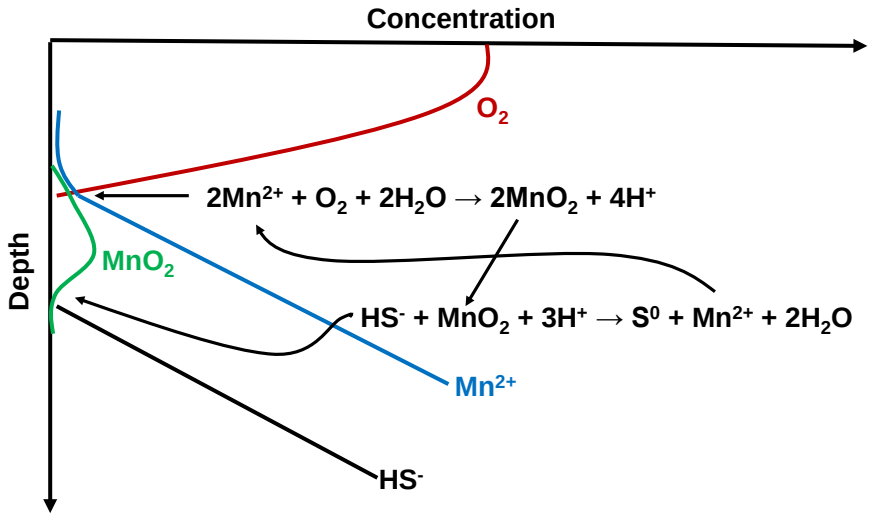

Fig.2 Redox cycle in the Black sea managed by manganese. Mn^{2+} is oxidized by down-welling O_2 forming MnO_2, while the produced MnO_2 reacts with HS^- to resupply Mn^{2+}[17].

Furthermore, some kinds of microbes produce Mn^{3+} through the oxidation of Mn^{2+} [19] and reduction of MnO_2 [20] during their respiration process. Webb et al. reported that *Bacillus* sp. Strain SG-1 produced Mn(III) bind to the enzymes which is the family of multi-copper oxidase during the respiratory Mn^{2+} oxidation detected by pyrophosphate titration technique [19]. Not only oxidative process, Lin et al. clarified that *S.* oneidensis reduces MnO_2 with a single two-electron transfer process via Mn(III) [20]. These reports clearly indicate that Mn^{3+} exists stably throughout natural environment in spite of its thermodynamic instability. Therefore, if the physicochemical origin of the stable Mn^{3+} in enzymatic catalytic cycle is clarified, we can tackle to these challenging issues.

One possible parameter to stabilize Mn^{3+} in natural system is the coordinating environment. The

origin of the instability of Mn^{3+} is the specific electrochemical property, called potential inversion. In normal condition, the removal of the second electron is thermodynamically more difficulty than the first one due to the coulombic repulsion. However, the situation for Mn^{4+}/Mn^{3+} and Mn^{3+}/Mn^{2+} is opposite; the removal of second electron is more feasible (Mn^{4+}/Mn^{3+} = 0.95 V and Mn^{3+}/Mn^{2+} = 1.5 V under neutral condition). This situation is the potential inversion. In this condition, the second oxidation proceeds immediately after the first oxidation resulting in the unstable one electron oxidation product (Mn^{3+}). The origin of potential inversion is discussed based on solvation energy [21]. Solvation energy is proportional to the square of charges of metal ions described in Born equation. Thus, the stabilization by solvation is asymmetric between Mn^{4+}/Mn^{3+} and Mn^{3+}/Mn^{2+} couples, resulting in the potential inversion. Since the solvation energy is also the function of dielectric constant of solvent, the energy should be largely different in protein environment from aqueous one. Indeed, DFT calculation demonstrated that the oxidation potential of Chl*a* of P680 in PSII is positively shifted with the decrease of dielectric constant, especially smaller than $\varepsilon = 5$ [22]. Therefore, it is expected that the redox tuning is achieved in the enzymatic reaction center.

However, the above discussion is based on the effect of the solvation and thus cannot explain the redox behavior difference of Mn ion between neutral and alkaline condition. The other candidate of the origin of the potential inversion is the protonated state of the aqueous ion as we focused on chapter 3. Evans reported that the switching of the reaction pathway between sequential and concerted proton-electron transfer (CPET) can alter the the redox property from the normal ordering and inverted order for benzophenone system [23]. We assume that the same concept can be adopted to aqueous metal ion system. Considering the fact that the pK_a of Mn^{2+}-OH_2 is 10.6, the protonation state of the Mn^{2+} is different between neutral and alkaline conditions. The difference of the protonation state indicates the net charges of the ion systems also differ

under these conditions. As the solvation energy largely depends on the net charge of the system, the effect of solvation is expected to be quite different between under neutral and alkaline condition. Especially, in the process of CPET, the net charge can be unchanged because both electron and proton are transferred simultaneously, resulting in the decrease of the asymmetry of the solvation effect. Therefore, the induction of CPET also can be one of the strategies to inhibit charge disproportionation in natural systems.

References

[1] H. Dobbek, V. Svetlitchnyi, L. Gremer, R. Huber, O. Meyer, Crystal Structure of a Carbon Monoxide Dehydrogenase Reveals a [Ni-4Fe-5S] Cluster. *Science,* **2001,** *293,* 1281-1285

[2] S. P. J. Albracht, Nickel hydrogenases: in search of the active site. *Biochim. Biophys. Acta,* **1994,** *1188,* 167-204

[3] C. Y. Ralston, H. Wang, S. W. Ragsdale, M. Kumar, N. J. Spangler, P. W. Ludden, W. Gu, R. M. Jones, D. S. Patil, S. P. Cramer, Characterization of Heterogeneous Nickel sites in CO Dehydrogenases from *Clostridium thermoaceticum* and *Rhodospirillum rubrum* by Nickel L-Edge X-ray Spectroscopy. *J. Am. Chem. Soc.,* **2000,** *122,* 10553-10560

[4] H. Wang, C. Y. Ralston, D. S. Patil, R. M. Jones, W. Gu, M. Verhagen, M. Adams, P. Ge, C. Riordan, C. A. Marganian, P. Mascharak, J. Kovacs, C. G. Miller, T. J. Collins, S. Brooker, P. D. Croucher, K. Wang, E. I. Stiefel, S. P. Cramer, Nickel L-Edge Soft X-ray Spectroscopy of Nickel-Iron Hydrogenases and Model Compounds-Evidence for High-Spin Nickel(II) in the Active Enzyme. *J. Am. Chem. Soc.,* **2000,** *122,* 10544-10552

[5] H. Dau, C. Limberg, T. Reier, M. Risch, S. Roggan, P. Strasser, The Mechanism of Water Oxidation: From Electrolysis via Homogeneous to Biological Catalysis. *ChemCatChem,* **2010,** *2,* 724-761

[6] H. Dau, I. Zaharieva, Principles, Efficiency, and Blueprint Character of Solar-Energy Conversion in Photosynthetic Water Oxidation. *Acc. Chem. Res.,* **2009,** *42,* 1861-1870

[7] S. Ferguson-Miller, G. T. Babcock, Heme/Copper Terminal Oxidases. *Chem. Rev.,* **1996,** *96,* 2889-2907

[8] R. H. Holm, P. Kennepohl, E. I. Solomon, Structural and Functional Aspects of Metal Sites in Biology. *Chem. Rev.,* **1996,** *96,* 2239-2314

[9] I. G. Denisov, T. M. Makris, S. G. Sligar, I. Schlichting, Structural and Chemistry of

Cytochrome P450. *Chem. Rev.,* **2005,** *105,* 2253-2277

[10] K. Kamiya, K. Hashimoto, S. Nakanishi, Instantaneous one-pot synthesis of Fe-N-modified graphene as an efficient electrocatalyst for the oxygen reduction reaction in acidic solutions. *Chem. Commun.,* **2012,** *48,* 10213-10215

[11] E. G. Kovaleva, M. B. Neibergall, S. Chakrabarty, J. D. Lipscomb, Finding Intermediates in the O_2 Activation Pathways of Non-Heme Iron Oxygenases. *Acc. Chem. Res.,* **2007,** *40,* 475-483

[12] R. Palkovits, M. Antonietti, P. Kuhn, A. Thomas, F. Schüth, Solid Catalysts for the Selective Low-Temperature Oxidation of Methane to Methanol. *Angew. Chem. Int. Ed.,* **2009,** *48,* 6909-6912

[13] S-. K. Lee, J. D. Lipscomb, Oxygen Activation Catalyzed by Methane Monooxygenase Hydroxylase Component: Proton Delivery during the O-O Bond Cleavage Steps. *Biochemistry,* **1999,** *38,* 4423-4432

[14] T. Takashima, K. Hashimoto, R. Nakamura, Mechanism of pH-Dependent Activity for Water Oxidation to Molecular Oxygen by MnO_2 Electrocatalysts. *J. Am. Chem. Soc.,* **2012,** *134,* 1519-1527

[15] E. M. Sproviero, J. A. Gascón, J. P. McEvoy, G. W. brudvig, V. S. Batista, Quantum Mechanics/Molecular Mechanics Study of the Catalytic Cycle of Water Splitting in Photosystem II. *J. Am. Chem. Soc.,* **2008,** *130,* 3428-3442

[16] R. E. Trouwborst, B. G. Clement, B. M. Tebo, B. T. Glazer, G. W. Luther III, Soluble Mn(III) in Suboxic Zones. *Science,* **2006,** *313,* 1955-1957

[17] K. S. Johnson, Manganese Redox Chemistry Revisited. *Science,* **2006,** *313,* 1896-1897

[18] A. S. Madison, B. M. Tebo, A. Mucci, B. Sundby, G. W. Luther III, Abundant Porewater Mn(III) Is a Major Component of the Sedimentary Redox System. *Science,* **2013,** *341,* 875-

878

[19] S. M. Webb, G. J. Dick, J. R. Bargar, B. M. Tebo, Evidence for the presence of Mn(III) intermediates in the bacterial oxidation of Mn(II). *Proc. Natl. Acad. Soc. USA*, **2005,** *102*, 5558-5563

[20] H. Lin, N. H. Szeinbaum, T. J. DiChristina, M. Taillefert, Microbial Mn(IV) reduction requires an initial one-electron reductive solubilization step. *Geochim. Cosmochim. Acta*, **2012,** *99*, 179-192

[21] D. H. Evans, One-Electron and Two-Electron Transfers in Electrochemistry and Homogeneous Solution Reactions. *Chem. Rev.*, **2008,** *108*, 2113-2144

[22] K. Hasegawa, T. Noguchi, Density Functional Theory Calculations on the Dielectric Constant Dependence of the Oxidation Potential of Chlorophyll: Implication for the High Potential of P680 in Photosystem II. *Biochemistry*, **2005,** *44*, 8865-8872

[23] S. Wang, P. S. Singh, D. H. Evans, Concerted Proton-Electron Transfer: Effect of Hydroxylic Additives on the Reduction of Benzophenone, 4-Cyanobenzophenone, and 4,4'-Dicyanobenzophenone. *J.Phys. Chem. C*, **2009,** *113*, 16686-16693

List of Publications

(1)"Electrochemical CO_2 Reduction by Ni-containing Iron Sulfides: How Is CO_2 Electrochemically Reduced at Bisulfide-Bearing Deep-sea Hydrothermal Precipitates?"

A. Yamaguchi, M. Yamamoto, K. Takai, T. Ishii, K. Hashimoto, R. Nakamura

Electrochim. Acta **2014**, *141*, 311-318

(2)"*In situ* UV-vis Absorption Spectra of Intermediate Species for Oxygen-Evolution Reaction on the Surface of MnO_2 in Neutral and Alkaline Media"

T. Takashima, **A. Yamaguchi**, K. Hashimoto, H. Irie, R. Nakamura

Electrochemistry **2014**, *82*, 325-327

(3)"Regulating Proton-Coupled Electron Transfer for Efficient Water Splitting by Manganese Oxides at Neutral pH"

A. Yamaguchi, R. Inuzuka, T. Takashima, T. Hayashi, K. Hashimoto, R. Nakamura

Nat. Commun. **2014**, doi:10.1038/ncomms5256

(4)" Water Splitting using Electrochemical Approach"

A. Yamaguchi, T. Takashima, K. Hashimoto, R. Nakamura, Springer *submitted*

(5)" Design of Metal-to- Metal Charge-Transfer Chromophore in a Polymer Matrix for Visible-Light Activation of O_2-Evolving MnO_2 Catalysts"

A. Yamaguchi, T. Takashima, K. Hashimoto, R. Nakamura, *in preparation*

Acknowledgements

This work was conducted under the supervision of Prof. Kazuhito Hashimoto from April 2012 to March 2015. Firstly, I owe my deepest gratitude to Prof. Kazuhito Hashimoto for his invaluable instruction for the research and provision of the sophisticated research environment. His enthusiastic education and critical comments enabled me to complete this work.

I would like to appreciate to Dr. Ryuhei Nakamura for his daily fruitful discussions and encouragements for continuing research activity.

I would like to express my gratitude to Dr. Keisuke Tajima, Prof. Kayano Sunada, Prof. Shuji Nakanishi, Dr. Akihiro Okamoto and Dr. Kazuhide Kamiya for their critical comment and suggestions during seminars and daily discussions.

I appreciate to Mr. Seiichiro Izawa, Mr. Takumi Ishii, and Mr. Shoichi Matsuda for their friendship.

I would like to show my appreciation to the members in Dr. Nakamura's group; Prof. Peng Luo, Dr. Satoshi Kawaichi, Dr. Li Yamei, Mr. Toru Hayashi, Mr. Hideshi Ooka, Mr. Hirotaka Kakizaki, Mr. Shogo Mori, Mr. Akira Murakami, Mr. Akio Umezawa, Mrs. Tomomi Minami as well as ex-members in Dr. Nakamura's group, Ms. Riko Inuzuka, Mr. Katsuhito Kondo, Mr. Taketo Mogi, and Mr. Koichiro Saito and Mrs. Keiko Tsukamoto for their kind help.

I owe a very important debt to Dr. Ken Takai, Dr. Masashiro Yamamoto in JAMSTEC and Dr. Toshihiro Takashima and Prof. Hiroshi Irie in Yamanashi univ. for their kind research help and suggestions.

I am grateful to all the other members of Prof. Hashimoto's Laboratory members for their help and discussion.

Finally, my heartfelt appreciation goes to my family and friends, who always supported and encouraged me to complete this work.

February 19th, 2015

Akira Yamaguchi